University of California
Los Angeles

Multiscale Modelling of Self-Organized Mono-Layer Surface Atomic Clusters

A dissertation submitted in partial satisfaction of the
requirements for the degree Doctor of Philosophy
in Mechanical Engineering

by

Qiyang Hu

2006

The dissertation of Qiyang Hu is approved.

Ya-Hong Xie

William Klug

Nick Kioussis

Yongho Sungtaek Ju

Nasr M. Ghoniem, Committee Chair

University of California, Los Angeles

2006

To my wife

Table of Contents

List of Figures

List of Tables

Acknowledgments

First of all, I would like to thank Professor Nasr M. Ghoniem for his great guidance in my graduate study and research, especially for his encouragement for me to be becalmed on the ocean of scientific knowledge. I also like to thank everyone in the Computational Nano&Micro Mechanics Lab for their help and the wonderful time we spent together.

Vita

1975	Born in Xining, China.
1993-1997	B.S., Engineering Mechanics, Tsinghua University, Beijing, China.
1997-2000	M.S., Engineering Mechanics, Tsinghua University, Beijing, China.
2000-2005	PhD, Mechanical & Aerospace Engineering, University of California, Los Angeles, USA.

Publications

Qiyang Hu, Nasr M. Ghoniem, Daniel Walgraef. Influence of substrate-mediated interactions on the self-organization of ad-atom clusters. Submitted to *Physical Review B*.

Qiyang Hu, Hyung-jun Kim, Ya-hong Xie, Nasr M. Ghoniem. Nucleation of self-organization of quantum dots with interfacial dislocation arrays. Submitted to *Journal of Computational and Theoretical Nanoscience*.

Qiyang Hu, Nasr M. Ghoniem, Daniel Walgraef. Multiscale modelling of self-organized mono-layer surface atomic clusters. *Technical Proceedings of the 2005 NSTI Nanotechnology Conference and Trade Show, Anaheim, California*, 2:306-9, 2005.

Abstract of the Dissertation

Multiscale Modelling of Self-Organized Mono-Layer Surface Atomic Clusters

by

Qiyang Hu

Doctor of Philosophy in Mechanical Engineering

University of California, Los Angeles, 2006

Professor Nasr M. Ghoniem, Chair

We present here a multi-scale modelling approaches for investigation of self-organized monolayer atomic clusters on atomically flat substrates during epitaxial deposition processes. A phase field model is developed for the free energy of the system, which includes short-range as well as long-range interactions between deposited atoms clusters mediated by the substrate. The way of calculating cluster interactions is the elastic theory of surface stress. The coverage-dependent part in nonlocal interactions is found to have a q^3 destabilizing effect, where q is the magnitude of the wave vector for spatial fluctuations in surface atom concentrations. The coverage-independent part associated with the presence of an external elastic field in the substrate is shown to provide an efficient way to control the spatial and size distributions of clusters. Qualitative and quantitative agreements between model predictions and experimental observations on self-organized Ge quantum dots on Si substrate are demonstrated. To precisely determine the influence of periodic strain fields in the substrate on the nucleation of self-organized surface atomic clusters, a Kinetic Monte Carlo model was developed. Island diffusion is found to play a dominant role in the early stage of nucleation.

CHAPTER I

Introduction

1 Quantum Dots and Atomic Clusters

NOWADAYS "nanotechnology" has become one of the most important branches in modern engineering and sciences. Nanoelectromechanical systems (NEMS), carbon nanotube field effect transistors, bio nanosensors and nanocrystal assemblers illustrate the emergence of a promising future in the economic production of goods and services. Quantum Dots (QDs), which are considered as a perfect candidate for future quantum computer chips and laser generators, have drawn special attention because of their special electronic and optical properties [8].

It should be noted that a so-called "nanoscale device" should be denoted by an object of which at least one of its dimensions is in the nanometer scale. Thus in a two-dimensional (2-D) case, the nanostructure might be a sheet with a nano-thickness. In a one-dimensional (1-D) case, it can be a nanowire or a nanocube. If the scaling is for all three dimensions, the structure would become so small that it contains only a few atoms (atomic cluster) and sometimes it is described as a "zero-dimensional"(0-D) or "dot" object. Unlike macroscopic bulk materials, strong size-dependent properties are magnified in nanostructures. Especially in atomic clusters, quantum states for electrons become few and sharply separated in energy. This is the reason why the term "quantum" often appears in the names of various nano-sized devices. A typical size of such an atomic cluster or

quantum dot is 10nm and it may contain 10^4 atoms or more [8]. Figure 1.1 shows two typical images of single quantum dot [47, 52].

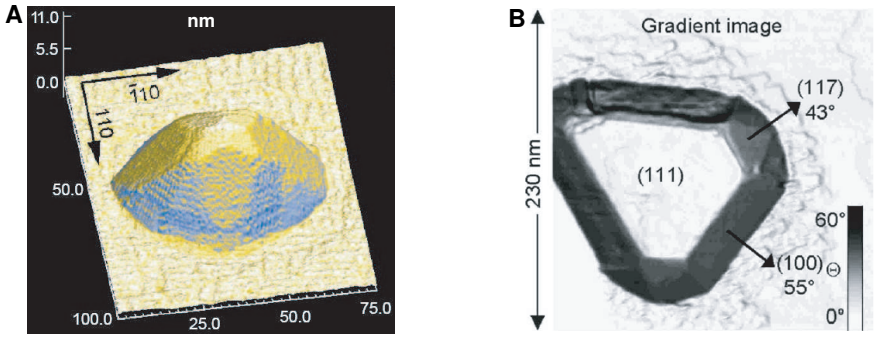

Figure 1.1: Experimental observations of single quantum dot. (A) Magnified STM topography image of Ge nanocrystal on Si(001) [47]. (B) STM topography, imaged in gradient mode, of a Ge island deposited on Si(111) [52].

One of the basic problems in the research on quantum dots is the fabrication of such nanometer structures, especially for a massive manufacturing process. The current research is initiated by this challenge, that is how to fabricate ultra small structures in a precise manner and control their spatial and size distributions. Initially researchers employed conventional fabrication techniques, such as patterning, masking, etching and lithography. All these methods in some sense belong to a "top-down" approach for fabrication which means that the ultra-small structures are obtained by manipulating or cutting from macroscopic objects. However, these methods have some intrinsic limitations, such as the production of defects during the manufacturing process. Another drawback is that the lateral resolution is always limited by the length scale of masks or the wavelength of light in lithography, which is limited on the order of 180nm [82].

In contrast to "top-down" approaches, there are two possibilities to manufacture quantum dots in a "bottom-up" way. One is to manipulate the individual

atoms and assemble them into an atomic cluster. This technique can be looked as an extension of the methods of scanning probe microscopy (STM). These scanning probe machines can be imagined as prototype molecular assemblers [82]. However this method cannot meet the need for the massive production in an industrial sense. The second choice is letting atoms assemble spontaneously by self-organization effects. The mechanism of atomic self-assembly will be discussed and reviewed in the next chapter. Generally speaking, however, self-assembly can be understood as a result of interactions between atoms during a non-equilibrium process. Since the intrinsic wavelength of self-organized patterns is often on the order of 10 nm, it is a preferred route to fabricate nano-size structures. Thus, the basic idea is to apply on the system some specific external field, which is able to interplay with the self-organized behavior of atoms and make the pattern biased in an expected way. Specifically, for fabricating self-assembled quantum dots (QDs), periodic external fields, such as the strain field on the surface generated by interfacial dislocation lines [34, 33], inclusions [73, 31] or void lattices [18] buried in the matrix may be utilized for self-assembly. Besides the elastic field mediated by the substrates, electro-magnetic laser fields which directly act on the surface adatoms have recently shown to be a good choice to generate regular distribution of atomic clusters [46, 57].

2 Scope and Contributions of Current Thesis

The present research work is aimed at the study of the influence of externally applied force fields on the mechanisms of self-assembly of surface atomic clusters on substrates during atomic deposition processes. In other words, we pursue here a comprehensive understanding of the nucleation of ad-atom clusters and the large-scale evolution of these clusters into specific regular patterns as a result

of the interplay between naturally self-organization and forced-ordering. It should be noted that in the present thesis, we use the term "*directed* self-organization" to denote the organization patterns by the coupling of spontaneous ordering effects ("*intrinsic* self-organization") and the applied external fields.

The main contributions of the current thesis can be summarized in the following:

- *Theoretical contributions:* Extension the Walgraef's theory of surface atomic self-assembly:

  1. The influence of external fields, such as those generated by periodic arrays of interfacial dislocations, bulk inclusions or laser electromagnetic fields has been specifically included.
  2. Cluster-cluster interaction energy terms in the general continuum model has been included.

- *Numerical contributions:* A series of numerical procedures based on systematic numerical Fourier-spectral methods in a Galerkin approach has been developed. This resulted in the development of new algorithms on single-processor and multi-processor (MPI) platforms in `Fortran` 90.

- *Atomistic simulations:* A relationship between the island size and binding energy by static MEAM interatomic potential calculations and the corresponding Kinetic Monte Carlo (KMC) simulations based on island diffusion kinetics have been developed.

The thesis is organized as follows. In Chapter II, experimental observations and theoretical developments for *intrinsic* and *directed* self-organizations surface atomic clusters are thoroughly reviewed. In Chapter III a phase field model

is presented in details. Especially the effect of external fields is described as a coverage-independent term and the cluster-cluster interaction is described as a global coverage-dependent term. A systematic spectral method is developed in Chapter IV for numerical solution of the governing equation of the phase field model. Then Chapter V presents the simulation results with both the natural self-organization and three possible external fields, which are periodic strain fields by interfacial dislocation networks, and by buried inclusions and periodic electromagnetic fields by lasers. A qualitative and quantitative comparison is made for the dislocation case. In Chapter VI an atomistic KMC model which is independent of the phase field model is presented and it gives the necessary information during the very early stage of surface cluster nucleation. Finally the conclusions and discussions are given in the last chapter, Chapter VII.

CHAPTER II

Literature Review

3 Experimental Observations

3.1 Intrinsic Self-Organization Phenomena

Self-ordering structures on surfaces, especially crystal surfaces, have been observed under a variety of experimental conditions. In Figure 3.1, three typical atomic images illustrate some of these observations. Figure 3.1 (A) shows a strip corrugated Au(111) surface formed by the interaction between surface steps and surface reconstruction processes. The lighter color lines in the STM image are stacking fault regions from the surface construction. It is found that a discommensuration line is systematically observed parallel to the step at the bottom of {100} steps, whereas {111} steps are always crossed by discommensuration lines. Figure 3.1 (B) shows square-shape dots of nitrogen atoms deposited on a copper surface. It is found that with increasing coverage, the original squares change to octagonal-like islands by "cutting" the corners, if other nitrogen islands are in the immediate neighborhood similar to the formation of four-leaf clover structures at low coverage. Finally the bare copper area between four adjacent octagons forms a square rotated by 45° with respect to the ⟨100⟩ direction. Fig. 3.1 (C) shows a self-assembled growth of highly symmetric germanium pyramids when Ge is deposited onto a T_4-boron surface phase on Si(111) at low temperatures (about

400°C). The Ge pyramids have heights of about 30 nm and base lengths of about 200 nm. It is also found that the pyramids have a perfect 3-fold symmetry and the dots are nearly uniform in size. They are aligned parallel to the terrace steps and all oriented in the same direction.

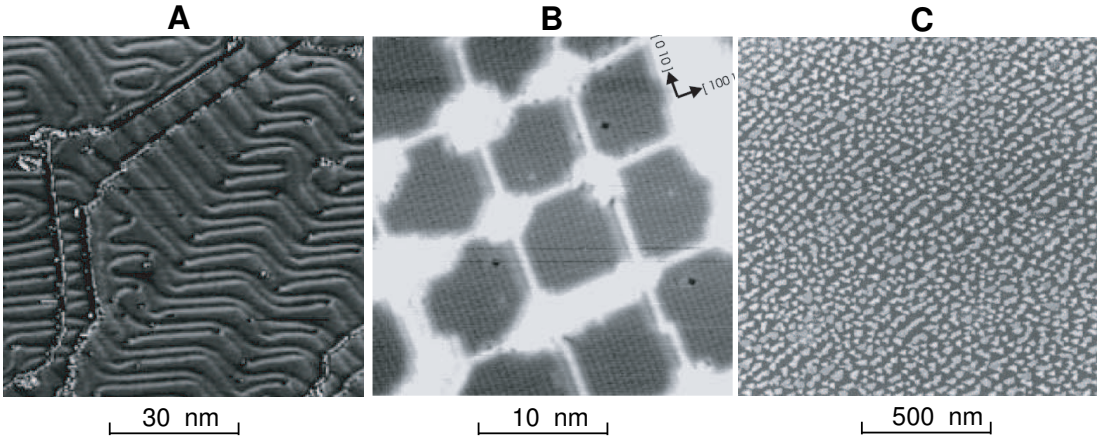

Figure 3.1: Experimental observations of self-ordering phenomena on the surfaces. (A) STM image of closed-packed steps on Au(111) surface [61]. (B) Atomically resolved image of Nitrogen domains on bare Cu substrate [16]. (C) AFM images of Self-Assembled Ge dots on top of $\sqrt{3}\times\sqrt{3}$ boron surface phase on Si(111) [15].

From the atomic images shown above, it can be seen that there are mainly two types of characteristic structures in self-organization, that are the dots and stripes[†]. For dot-type structures, it has been theoretically shown that on isotropic surface the dots will be distributed in hexagons [79]. If the surface is anisotropic which is a crystal surface, the distribution will much depend on the detailed property of the anisotropy [59]. In Figure 3.1 (B), the square shape dots are formed since the χ parameter of copper is $\chi = c_{11}-c_{12}-2c_{44} = -1.0$ [16]. Another characteristics in the above experiments is that the internal length scale of the self-ordering structures is in nano-scale, which is usually very small compared

[†]Another type of self-ordering structure is the "hole" which is the reciprocal type of dots.

with the external field applied.

3.2 Interfacial Dislocation Fields

A conventional way to form surface clusters by coupling self- and forced- organization is to create a periodic elastic field in the substrate generated by a periodic dislocation array of interfacial dislocations. The non-uniform and periodic stress field on the surface forces atoms to be "self-" assembled.

An extensive experimental study was undertaken by Kim *et al.* [32, 34]. In their experiments, samples were grown in a Riber EVA-32 molecular beam epitaxy (MBE) system equipped with two electron beam evaporation sources of Si and Ge. The entire relaxed buffer layer was grown at 550°C with the growth rate of $2\,\text{Å} \cdot \text{sec}^{-1}$. The structure is nearly elastically strained as grown. When the layer exceeds the critical thickness for pseudomorphic growth, the mismatch strain is relieved by the formation of misfit dislocations. The thin Si capping layer is thus under a tensile strain, which served to keep the surface flat. Post growth anneals at 700°C for 30 minutes were used to introduce the buried misfit dislocation network. The resulting misfit strain relaxation after the anneal was approximately 10%. The surface of the relaxed buffer layers has typical roughness 9.9 Å RMS according to atomic force microscopy (AFM). The growth rate of Ge QDs for all samples was kept constant at 0.05 Å/s for the same coverage of Ge. The thickness of the partially relaxed $Si_{1-x}Ge_x$ buffer layer (the experimental variable in this study) varied from 300 Å to 2000 Å in order to study the effect of the strain field from interfacial dislocations on the self-assembly of Ge QDs.

A Park Scientific AFM operating in the contact mode was used for the characterization of the resulting surface topography. The directions of Burgers vectors of the interfacial buried dislocations as well as the preferential nucleation sites of Ge

SAQDs were determined by using a plan-view transmission electron microscope (TEM). A 200-kV JEOL 2000FX was used for the plan-view TEM micrographs and Burgers vector analysis using four different g-vectors including $\mathbf{g} = \langle \bar{1}\,3\,\bar{1} \rangle$, $\langle 1\,3\,\bar{1} \rangle$, $\langle 1\,1\,\bar{1} \rangle$, and $\langle \bar{1}\,1\,\bar{1} \rangle$ and the $\mathbf{g} \cdot \mathbf{b} = 0$ extinction criterion.

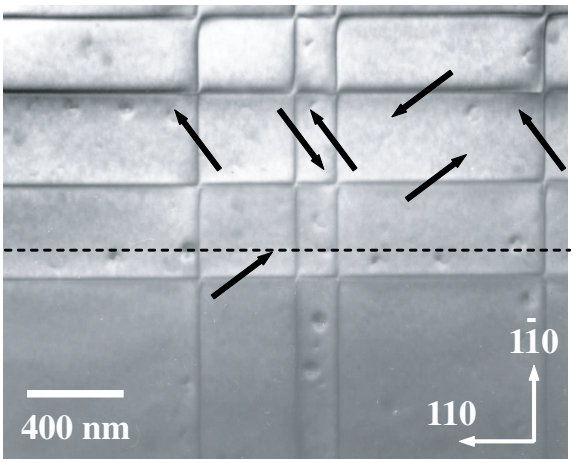

Figure 3.2: A plan-view STM micrograph of the sample with Ge SAQDs grown on the relaxed 800$\mathring{A}$ thick $Si_{0.85}Ge_{0.15}$ buffer layer is shown [32].

Figure 3.2 is the corresponding plan-view TEM image representing the ordering of Ge SAQDs along underlying buried dislocations in the relaxed 800$\mathring{A}$ thick $Si_{0.85}Ge_{0.15}$ buffer layer. The projections of Burgers vectors corresponding to individual dislocations onto the interface plane are marked by arrows, verifying the direction of the slip plane. Each array of SAQDs is not only clearly associated with a single buried dislocation but is also observed to be decisively located on one side of the buried dislocations.

The average distance (650$\pm$13$\mathring{A}$) between the dislocation line and the array of Ge SAQDs, in Figure 3.2, approximately agrees with a calculated value of 640 Åwhich is the lateral distance from the buried dislocation to the position where the $\{1\,1\,1\}$ slip plane intersects the top surface of the 900 Å (800 Å

$Si_{0.85}Ge_{0.15}$ plus 100 Å Si capping) thick underlying layers. A dashed line indicates the centers of the dots which belong to the horizontal dislocation below.

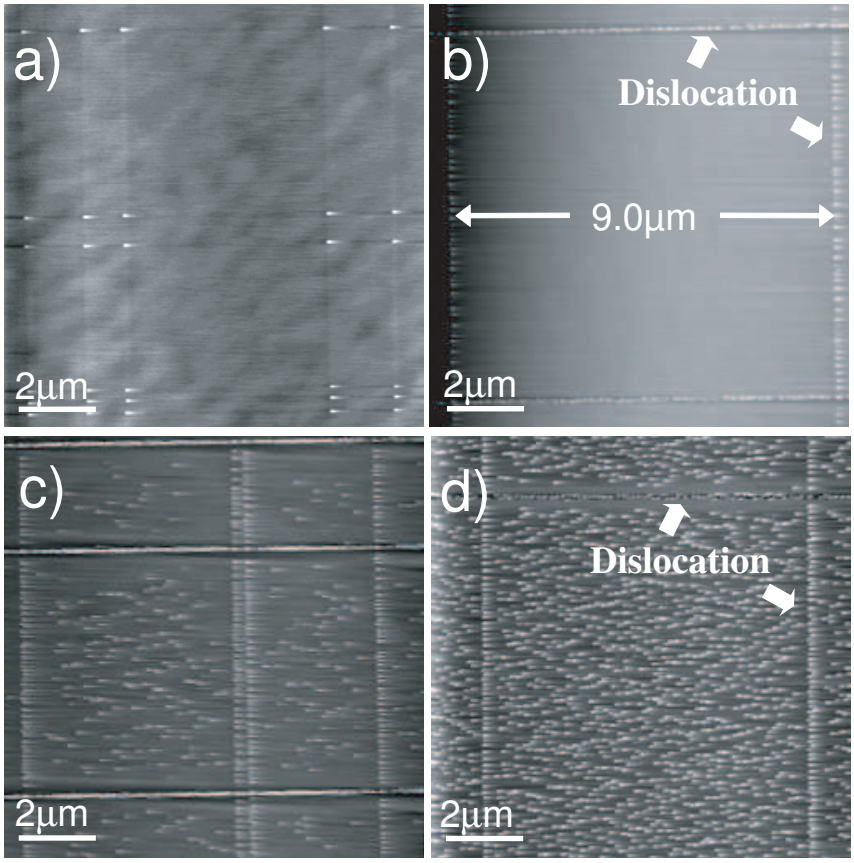

Figure 3.3: AFM topographic images of Ge SAQDs with $4 - 6$ Å coverage on a partially relaxed $Si_{0.9}Ge_{0.1}$ buffer layer. From (a) to (d) the Ge coverage is respectively 4.0 Å, 4.5 Å, 5.0 Å, 6.0 Å [34].

Figure 3.3 shows the existence of three types of surface sites and the resulting three-stage nucleation at dislocation intersections (a), single dislocation lines (b), and in regions far away from dislocations (c) respectively. These observations can also be understood as three different organization patterns resulting from the coupling between the self-ordering interactions and the external strain fields. The local coverage, c, can be viewed as the control parameter here. It should

be noted that Ge growth on a Si substrate follows the Stranski-Krastanov (SK) mode, in which the first several monolayers of the deposited material grow in a layer-by-layer mode due to surface and interface energy minimization. This thin layer is known as the wetting layer, the thickness of which is about 3 monolayer (ML) $\sim 4.2\,\text{Å}$. The Ge dot coverage in the figure should be regarded as only from $0.2\,\text{Å}$ to $1.8\,\text{Å}$, which is about 0.14ML to 1.28ML. In the experiment, it is found that during this range of coverage, the dots are formed with a pyramid shape with very low aspect ratio around $1 : 10.8(\pm 1)$ representing slightly lower angle facet. Thus, it is reasonable to approximate the dots in a monolayer form with such a low coverage or at the very early stages of cluster nucleation during atomic deposition.

3.3 Inclusion/Void Fields

Besides interfacial dislocations, a possible source of periodic surface elastic field is a regular array of buried inclusions. Compared with dislocation sources, the inclusion source provides a more flexible tool to control the lateral arrangement and position of atomic clusters. In an experimental sense, the growth of self-assembled quantum dots on the surface is aimed at a three-dimensional stacking of quantum dots in multilayers or super lattice structures. Thus we need to be concerned with not only the lateral correlations between the dots on one surface, but also the vertical correlations of the dot distribution between different layers. It is found that various mechanisms can induce different dot stacking modes [73]. Figure 3.4 shows some representative examples for different types of interlayer dot stackings in self-assembled quantum dot multilayers in which we can have an idea about the complexity of the problem. It is found that the vertical dot alignment along the growth direction is the predominant case

for most self-assembled quantum dot systems as shown in Fig. 3.4(a) for an InAs/GaAs superlattice. On the other hand staggered dot stacking were observed for a number of other systems such as InAs/AlInAs quantum wire superlattices as shown in Fig. 3.4(e) and (f), as well as an *fcc*-like $ABCABC\ldots$ stacking for IV-VI dot superlattices as shown in Figure 3.4(b).

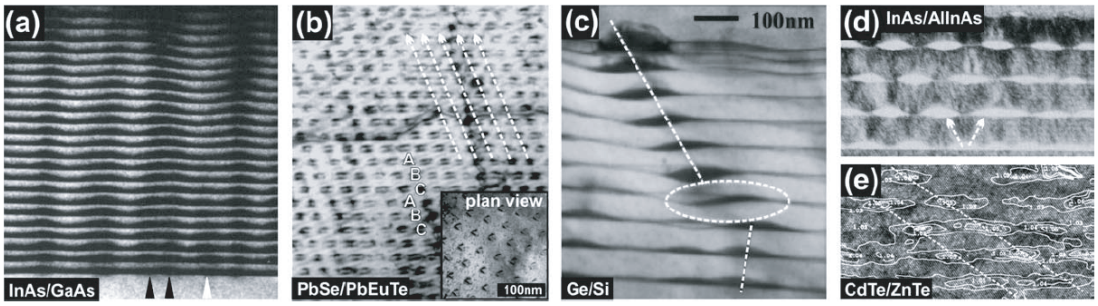

Figure 3.4: Examples of some representative types of interlayer dot stackings in self-assembled quantum dot multilayers as revealed by cross-sectional TEM [73]: (a) vertically aligned (001) InAs QD superlattice with 20nm GaAs spacer layer. (b) Staggered stacking in a PbSe/PbEuTe (111) quantum dot superlattice with 5ML PbSe alternating with 45 nm PbEuTe. (c) Inclined dot correlations in a Ge dot superlattice of 1.2 nm Ge alternating with 40 nm Si spacers. (d) Vertically anticorrelated InAs/AlInAs quantum wire superlattice (3 ML/10 nm, respectively) on InP(001). (e) Anticorrelated multilayer of 2 ML CdTe islands separated by 15 ML ZnTe spacers.

It is easy to see that the desired field in fabricating quantum dots should all have two common features. One is the high regularity of the desired distribution of the fields. The other is that the ordering field should have adequate strength of the field. With the advancement of nuclear technology, it is found that a very regular pattern of the strain field can be achieved in irradiated materials by energetic particles (e.g. electrons, ions and neutrons). In these experiments,

many self-organized defect clusters, dislocation loops, voids and bubbles can be observed. Especially implantation of metals with energetic helium can result in remarkable self-assembled bubble super-lattices with wavelengths (super-lattice parameters) in the range of $5 - 8\,\mathrm{nm}$ as shown in Figure 3.5 [18].

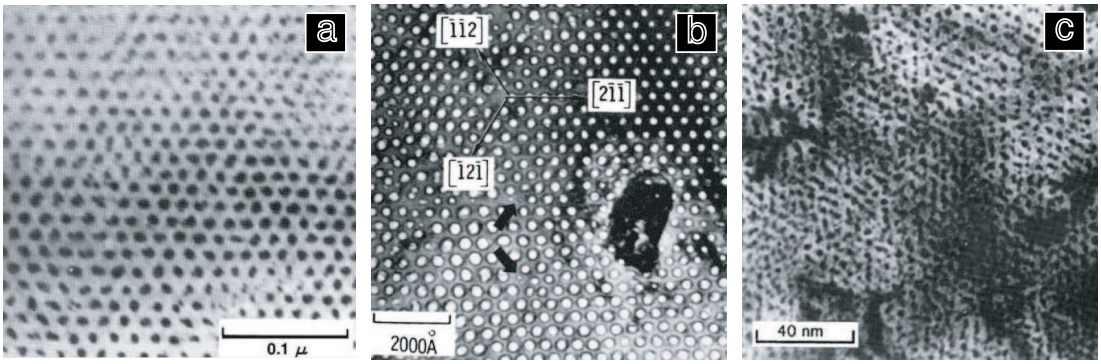

Figure 3.5: Three void lattice examples collected in [18]: (a) Mo: TEM showing a BCC void superlattice in molybdenum irradiated with 2 MeV N+ ions to a dose of 100 dpa at 870°C. (b) Nb: TEM showing a BCC void superlattice in niobium irradiated with 7.5 MeV Ta+ ions to a dose of 300 dpa at 800°C. (c) TEM observations of helium bubble lattice in Mo irradiated with 40 KeV helium at 500°C to an ion flux of $5 \times 10^{21}\,\mathrm{m}^{-2}$.

The experimental observations suggest that void superlattice can be formed over a wide temperature range. And with the summarized experimental data in [18], it is found that the void lattice parameter is typically about two orders of magnitude larger than the atomic lattice parameters and about four times larger than the void diameter in fully-developed void superlattices. Since the relaxation of voids due to the free surface is only about 3 percent, the self-ordering void lattice might be able to provide a perfect strain field so that a completely new method to fabricate the self-assembled quantum dots with highly uniform distributions. Although there is no real experiment appearing in the literature

to realize the quantum dot formation in irradiated materials, we believe it would become a promising method in QD fabrication in the near future.

3.4 Electromagnetic Fields

An alternative way of utilizing external fields is to apply electromagnetic fields during and after the atomic deposition process (see Figure 3.6 Left). Sometimes this technique is called an optical-mask. In this method, all interactions of adatoms are mediated by the field itself. A representative experiment is the deposition onto a silicon substrate of chromium (Cr) atoms, which are focused by a standing-wave laser fields performed by McClellend [46, 45]. The dye-laser frequency is set above the atomic resonance by 60 to 240 MHz. The laser cooling beams (for optical collimation) are frequency shifted with an acousto-optic modulator (AOM) to just below the atomic resonance. Figure 3.6 (Right) shows a three-dimensionally rendered view atomic force microscope images of laser-focused chromium nanostructures. The resulting nanostructures are highly-regular arrays of Cr with height up to 60 nm, and can be as narrow as 28 nm and are spaced at exactly half the laser wavelength.

Further experiments have been performed to generate the dot structure by a 2-D laser intensity. The perfect distribution of chromium dots are formed in McClelland's experiments by two-dimensional standing linear polarized waves (see Figure 3.7).

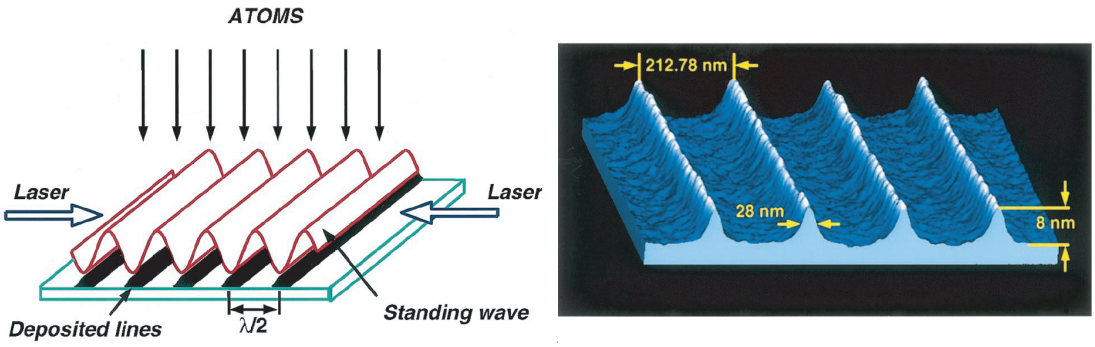

Figure 3.6: Left: A standing wave laser field forms a series of cylindrical lenses for Cr atoms, focusing them into nanometer-sized lines during the deposition onto a substrate. Right: Atomic force microscope images of laser-focused chromium nanostructures in which three-dimensionally rendered view showing some of the narrowest features created in Si [46].

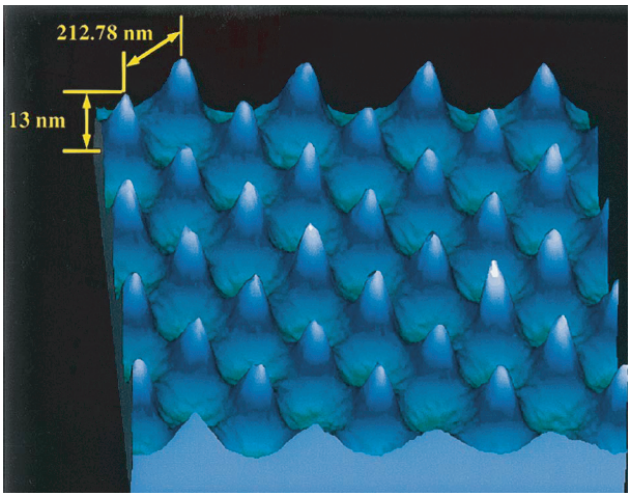

Figure 3.7: Atomic force microscope images of laser-focused chromium dot structures in which 3-D rendered view created on Si [45].

4 Review of Theoretical Modelling

4.1 Understanding Self-Organization

Self-organization is a process where the internal structures or organizations spontaneously increase without any influence or guidance by an external source. Systems having self-assembled behavior have been widely observed in many different areas, such as the Belousove-Zhabotinskii reaction in chemistry, morphogenesis and homeostasis in biology and cellular automata in mathematics. But the most profound and robust examples of "self-organized" systems are found in physics, such as Bénard cells in convection, dendrete formation during crystallization and the clustering of adatoms on a surface during thin film growth.

In the literature on quantum dot formation and thin film deposition, however, the word "self-organization" is commonly used to describe two different processes, both of which are closely related.

In some studies "self-organization" refers to an equilibrium process, which means that the system to be considered is a thermodynamically static one [8, 64]. From this viewpoint, the equilibrium shapes or positions of a group of QDs is determined by minimizing the change of total free energy $\Delta\mathscr{F}$ of the system, which can be written as

$$\Delta\mathscr{F} = \Delta\mathscr{E}_{\text{surf}} + \mathscr{E}_{\text{edge}} + \Delta\mathscr{E}_{\text{elastic}}, \tag{4.1}$$

where $\Delta\mathscr{E}_{\text{surf}}$ is surface energy of the tilted facets, $\mathscr{E}_{\text{edge}}$ is the short-range energy of edges and $\Delta\mathscr{E}_{\text{elastic}}$ is the elastic relaxation energy due to the discontinuity of the surface stress tensor σ_{ij} at crystal edges[66]. This thermodynamic approach has successfully been used to explain the formation of three types of modes during thin film deposition: the layer-by-layer mode (Frank-van de Merwe

or FM growth), the island mode (Volmer-Webber or VW growth) and the layer-plus-island mode (Stranski-Krastanov or SK growth) with an equilibrium phase diagram of a lattice-mismatched heteroepitaxial system[4]. The geometries and equilibrium shapes of quantum dots are well analyzed theoretically [65, 66]. The essence of this approach is that the system considered must be macroscopically large enough to apply classical elasticity theory and that all kinetic processes are ignored.

The second description of self-organization refers to a dynamic process, in which the structure formation achieved in thermodynamic systems away from equilibrium. Since quantum dot formation is a process that includes nucleation, size growth and coarsening of different phases, the whole system can be regarded as a reaction-diffusion type. One famous model to describe this kinetic process is the classical Lifshitz-Slyozov-Wagner (LSW) theory[78], which is used to explain the coarsening procedure called Ostwald ripening. In the LSW theory, an atomic cluster is considered as a particle with a certain size, and that clusters are distributed dilutely. This implies an assumption that the particle size is small compared to the distance between particles. The evolution of the dots or the second phase is characterized by the particle-radius distribution $n(r,t)$, where $n(r,t)\,dr$ is the number of particles per unit volume at time t with radius between r and $r+dr$. By the conservation law, the distribution function satisfies the partial differential equation (PDE) as[55]

$$\partial_t n + \partial_r\big(V \cdot n\big) = 0, \tag{4.2}$$

where $V = dr/dt$ denotes the growth rate of a particle with radius r at time t. Lifshitz and Slyozov, and independently Wagner, quantitatively analyzed the asymptotic behavior of the particle-size distribution in three dimensions. They

showed that in the limit $t \to \infty$, the radius of the particles (or the linear dimension of islands) increases following a simple dynamic scaling law, say, $\bar{R}^3 = Kt$, where $\bar{R}$ is the average particle size and K is the rate constant. Although this analysis predicts Ostwald ripening of the microstructure of solid-liquid mixtures, it obviously contradicts self-organization phenomena during the deposition of hetereptaxial thin films. The significant point here is that interparticle diffusional interaction are assumed to be absent and that the interfacial energy is the driving force for the process according the Gibbs-Thomson law for local equilibrium. Hence, equilibrium shapes and mutual arrangements of the dots are unchanged.

Another dynamic model which avoids the shortcoming's of the LSW theory is the Asaro-Tiller-Grinfeld (ATG) model[2], in which the surface profile of a bulk material is described by mass transport due to the surface diffusion of atoms. Considering the conservation of the mass flux on a solid film surface, the dynamic rate equation can be written as

$$\frac{\partial \mathbf{r}}{\partial t} = -\Omega(\nabla_{\mathrm{S}} \cdot \boldsymbol{\mathcal{J}}_{\mathrm{S}})\mathbf{n}, \tag{4.3}$$

where $\mathbf{r}$ is the position of surface atoms and $\mathbf{r} = [x, y, h(x, y, t)]$. Ω denotes the atomic volume and $\mathbf{n}$ denotes the normal vector of the surface. $\boldsymbol{\mathcal{J}}_{\mathrm{S}}$ is the surface atom flux which is taken to be proportional to the surface gradient of the diffusion potential:

$$\boldsymbol{\mathcal{J}}_{\mathrm{S}} = -\frac{D_{\mathrm{S}}\nu}{k_{\mathrm{B}}T}\nabla_{\mathrm{S}}\Big(\mathscr{E}_e + \sigma_{ij}\,\kappa_{ij}\Big) \qquad \text{on} \quad z = h(x, y, z), \tag{4.4}$$

where D_{S} is the surface diffusion coefficient of atoms, ν is the surface density of lattice sites, k_{B} is the Boltzmann constant, T is the absolute temperature. $\mathscr{E}_e$ is the elastic energy due to bulk elastic deformation. This can be induced by

thermal expansion, lattice mismatch relaxation, and/or defect relaxation of the bulk. The surface energy is the product of the surface tension σ_{ij} and the surface curvature κ_{ij}. By numerically solving Equations (4.3) and (4.4), the morphology of the surface is simulated. Stability analysis can provide useful information on the critical thickness of a dislocation-free solid films [72], and the nonlinear patterns during thin film growth [70]. The equilibrium morphology of an epitaxial strained layer, which wets the substrate (SK growth) can also be calculated [71]. In the framework of this approach, self-organization is understood as a balance between the volume elastic energy and the surface energy. This may give a similar interpretation to the equilibrium self-organization process described at the beginning of this section (see Equation 4.1).

Another treatment of the problem is based on the coverage of adsorbates on the surface as the key variables. By considering each species of ad-atoms to occupy one lattice site on the surface as a phase and the vacancy do a second phase, the problem acquires a good similarity with that of phase separation in alloys. One of the fundamental governing equations for phase separation in alloys is the celebrated Cahn-Hilliard (C-H) nonlinear diffusion equation. This equation is *again* based on the mass conservation law as [11]

$$\partial_t c_i(\mathbf{r}, t) = \nabla M_{ij} \nabla \frac{\delta \mathscr{F}}{\delta c_j(\mathbf{r}, t)}. \tag{4.5}$$

where a continuum and conserved order parameter, c_i, usually considered as the concentration of atomic species, i, is the parameter that describes the evolution of self-organized structures. Specifically in surface atomic cluster formation problems, only a scaler is meaningful and then c denotes the concentration or coverage of second phase particles or adsorbates on the surface. M_{ij} is related to atom or interface mobility. The variational derivative of the free energy $\mathscr{F}$ leads to

a nonlinear partial differential equation for the evolution of order parameter, c. For an isotropic case with a constant mobility M, the general form of the C-H equation becomes:

$$\partial_t c = M\Big[\nabla^2 f'(c) - \epsilon^2 \nabla^4 c\Big], \tag{4.6}$$

where $f'(c)$ is a specific function related to the diffusion flux. The fourth order derivative term represents the effects of the interfaces between the phases.

It is easy to see that self-organization described by Equation 4.6 stems also from the interplay between interatomic diffusion and interface energies. The power of this approach is that it interprets both phase transitions and atomic interactions.

The conventional way in the literature to determine the local free energy function $f'(c)$ is to write a Ginzburg-Landau (GL) energy functional where a polynomial expansion is made to express the potential having a double-well shape around the critical point [59]. The advantage of this Landau approach is that it retains the linear relation around the critical point and makes the instability analysis possible. However the drawback is that this expression cannot give the correct information when the system is away from the critical point.

Another remark on the Cahn-Hilliard type modelling is that the continuity of the variable c implies a continuous interfaces between adsorbates and vacancies. Other modelling approaches, such as the level-set method, similar to the idea of the phase separation in alloys, are based on tracking the evolution of sharp interfaces. Indeed the LSW theory belongs to the sharp-interface approaches. In the present work, we will only focus on the C-H type of models.

It is noted that in the alloy phase separation problem, two types of order

parameters exist. One is the composition order-parameter, which is obviously a conserved quantity. It obeys the Cahn-Hilliard type nonlinear diffusion equation. The coverage c plays the same role in the adatom cluster formation problem. It should be mentioned that there is possibly another ghost order parameters ϕ in the phase separation problem, which is *not* a conserved quantity and obeys the Allen-Cahn equation instead [29]. It may become necessary if we consider both adatom clustering and the phase changes of clusters.

4.2 Multiscale Modelling Methods

Since most of the models proposed to understand self-organization effects are based on a conservation law of some continuum variables (e.g. the particle radius distribution function $n(\mathbf{r}, t)$, the position vector of the surface atom volumes $\mathbf{r}$ and the coverage $c(\mathbf{r}, t)$), the question then arises as to whether there is a need to adopt a first-principle approach, e.g. atomistic simulations, to study the self-organization. In fact, numerous computer simulations, such as molecular dynamics (MD) and Monte Carlo (MC) methods, have been performed in the literature and revealed detailed information on thin films [20, 28]. In most cases, the length scale of the system characterized by the applied external field is on the order of microns. However, self-organized patterns are usually much finer, with a length scale on the order of tens of nanometers. Thus coupling between these scales becomes a *multiscale* modelling problem. Atomistic simulations can only provide information on some of the physical mechanisms. Indeed, we will use the Kinetic Monte Carlo (KMC) method to study one aspect of the problem in the last chapter of the present thesis. It is not sufficient to explore the effects of coupling between self-(nano-sized) and forced-(macroscopic) organizations solely by MD or MC simulations. In MD simulations, the required deposition rate needs

to be unrealistically high so that it possibly gives rise to unrealistically large roughness. And the computational time in Monte Carlo methods to simulate thin-film growth under realistic deposition rates is still excessive.

A recent interpretation of "multi-scale modelling" classifies simulations bridging different scales as three methods: hierarchical, concurrent and multi-scale boundary conditions [38]. The basic idea of *hierarchical* approaches is simply a parameter-passing scheme, in which some key parameters are calculated from the fine scale by atomic physics and used in the macroscopic theory. In *concurrent* approaches, simulations at different length scales (e.g. MD, MC, and FEM) are performed simultaneously and the physical parameter is transferred by some artificial handshake rules. A representative successful model is the quasi-continuum method [67]. The *multi-scale boundary condition* method is quite similar to concurrent approaches, but it replaces the handshake region by a set of next-to-interface atoms from the coarse grain region.

In the present thesis, however, we will adopt another viewpoint to the word "multi-scale modelling". In order to make things clearer, let's look back at the types of problems in a wider viewpoint for which multiscale modelling is needed. Basically, there are two types of physical problems that need bridging different scales. The first type is that the local microscopic behavior itself is the object of the study and it is subjected to the macroscopic body, such as the nano-indentation on a surface of a bulk and micro-fluidic devices in a moving fluid. The second type of problems is that microscopic properties do have dramatic effects on the macroscopic behavior. An excellent example is the study of macroscopic quantum phenomena such as superconductivity and superfluidity. Another perfect example is the nature of microscopic defect patterns during plastic deformation and fatigue. A usual modelling idea in physics is to obtain the

complete information of the system by an "ab inito" method, which means that the motion of a mechanical system is described by its degrees of freedom. All of atomistic simulations, dislocation dynamics etc. follow this route. We may call it is a "motion"-based viewpoint since the model is based on the description of the exact motion of each physical quantities (single atoms or single dislocations etc.). This "motion" viewpoint is good in studying the first type of problems. However, if a very large number of degrees of freedom must be considered in a system, the methods of "motion" mechanics becomes completely impracticable. An alternative way is to utilize the statistical physics which deals with the "state" not the "motion" of the system in the presence of a very large number of particles. With this "state" viewpoint, phenomena in the second type of problems can be considered as phase transition problems. Several systematic approaches, such as Landau theory and renormalization group theory, have been developed along this lines.

All three multiscale modelling methods summarized in Liu's review paper [38] follow the motion-based idea, in which the degrees of freedom to be considered are not too large[†]. The quasi-continuum method, for example, is an excellent extension of the mechanical description with the application of powerful mathematical techniques (e.g. finite element methods). On the other hand, kinetic theories in the form of traditional rate equations combined with the *state* description by statical physics provide general methods of theoretical analysis which interpret the effects of microscopic properties on macroscopic bodies. Macroscopic theories such as London Theory and Ginzburg-Landau Theory of superconductivity belong to this category. The attempt to apply the field-theory to model polycrystalline plasticity by Hasebe is also a good example of state-based multiscale modelling [23]. In most cases, self-organization phenomena are similar to phase

[†]For example, in nano-indentation only the local microscopic deformation is considered.

transition problems. This is the reason why the mechanisms of self-organized pattern formation are proposed mostly within the framework of kinetic rate theory.

In our research on pattern formation of self- and force- organized atomic clusters, we will follow the rate equation approach. Furthermore, to simplify the problem, we will not consider 3-D island formation, but only 2-D monolayer cluster formation on the surface. Thus, a phase-field equation of a modified Cahn-Hilliard type with a variable of the coverage $c(\mathbf{r}, t)$ for surface atomic clusters will be set up instead of the elastic surface roughening equations of an Asaro-Tiller type with a variable of the position vector $\mathbf{r}(t)$ that describes the surface. Specifically, within the framework of the conservation law of adatoms, nearest-neighbor interaction terms are obtained by formulating possible states of all individual adparticles with two-body interactions by statistical physics, in which the mean field approximation is introduced. This can be regarded as a "bottom-up" procedure where microscopic information is brought and transformed into the macroscopic scale. For long-range interactions between the clusters via the substrate and applied external fields, we will adopt an important assumption used in the concurrent quasi-continuum approach which hypothesizes that the infinite crystal with discretized atoms deforms according to a locally continuum deformation gradient. This is the so-called *Cauchy-Born* rule, which provides a "top-down" passage from the macroscopic elastic deformation to the microscopic model. In addition to the rate-equation approach, we perform KMC simulations to determine the atomistic nature of organized clusters in Chapter VI. As the general idea of the KMC approach, the energies of the cluster diffusion are evaluated by the random cluster scaling theory. Obviously the two approaches are parallel and not unified in one frame of the modelling.

CHAPTER III

Proposed Phase Field Model of Self-Organized Surface Atom Clusters

5 Kinetic Equation

Let us consider the local atomic coverage of the substrate $c(\mathbf{r}, t)$ as the variable. By the conservation law of adatoms, a continuous phase field model can be constructed as a result of reaction and diffusion processes within the framework of chemical kinetics via the following equation

$$\frac{\partial c}{\partial t} = R(c) - \nabla \cdot \boldsymbol{\mathcal{J}}, \tag{5.1}$$

where $c = c(\mathbf{r}, t)$ is defined as the average occupancy number or average number of atoms per lattice site. $R(c)$ is the reaction rate. The reaction process is restricted to only the adsorption and desorption rates (α and β) in the absence of chemical reactions with the substrate and precursor molecule dissociation. Generally α and β should be functions of the physical parameters of the deposition mechanisms and may also be coverage dependent as in the case of reacting adsorbed layers [25]. However, for some non-equilibrium processes, such as sputtering or laser-assisted deposition, the reactions are not thermally activated. Thus, in a first approximation, we will simply consider the reaction rates to be constant, and express the net adsorption rate as

$$R(c) = \alpha(1-c) - \beta c. \tag{5.2}$$

$\boldsymbol{\mathcal{J}}$ in Equation 5.1 denotes the atomic diffusion flux on the substrate. When the interactions between adsorbed atoms are important, the usual Fick's law cannot be applied in the adsorbed layer and the diffusion activity is governed by a spatially varying chemical potential. In this case, a convenient way is to consider the vacancy which is an empty site unoccupied by adatoms as a "ghost" atom. Thus for a single species adsorbate layer, the system contains two-species. Linear non-equilibrium thermodynamics gives a relationship between fluxes and thermodynamic forces as [22]

$$\begin{aligned} \boldsymbol{\mathcal{J}}_{\mathrm{A}} &= \mathcal{L}_{\mathrm{AA}}\mathbf{X}_{\mathrm{A}} + \mathcal{L}_{\mathrm{AV}}\mathbf{X}_{\mathrm{V}} \\ \boldsymbol{\mathcal{J}}_{\mathrm{A}} &= -\boldsymbol{\mathcal{J}}_{\mathrm{A}}, \end{aligned} \tag{5.3}$$

where $\boldsymbol{\mathcal{J}}_{\mathrm{A}}$ and $\boldsymbol{\mathcal{J}}_{\mathrm{V}}$ are the fluxes of occupied and vacancy sites, respectively. $\mathbf{X}_{\mathrm{A}}$ and $\mathbf{X}_{\mathrm{V}}$ are the associated thermodynamic forces. $\mathcal{L}$ is the atomic mobility. Using Gibbs-Duhem and Onsager's reciprocity relations, one has

$$\mathcal{L}_{\mathrm{AA}} = -\mathcal{L}_{\mathrm{AV}} = -\mathcal{L}_{\mathrm{VA}} = \mathcal{L}_{\mathrm{VV}} = \mathcal{L}. \tag{5.4}$$

Thus we can use the general expression of the mobility as $\mathcal{L} = D/k_{\mathrm{B}}T$, D is the surface diffusion coefficient. Basically, the diffusion coefficient should depend on coverage and the influence of the presence of other clusters or other sinks. For example, in the case of hopping types of atomic motions, an appropriate expression can be written as $D = D_0 c(1-c)$. However, as a first approximation, we will simply ignore the dependence of D on the coverage c. At the same time, for diffusion induced by thermally activated atomic jumps, we have $D =$

$D_0 \exp(-\Omega/k_{\mathrm{B}}T)$. At sufficiently high temperatures, such that $k_{\mathrm{B}}T \gg \Omega$, we could also ignore the temperature dependence of D.

In the case of an isothermal process, thermodynamic forces are the gradients of the chemical potentials. Using the fact that the chemical potential is the functional derivative of the free energy, the atomic mass flux $\boldsymbol{\mathcal{J}} \equiv \boldsymbol{\mathcal{J}}_{\mathbf{A}}$ becomes

$$\boldsymbol{\mathcal{J}} = \mathcal{L}\,\nabla(\mu_{\mathrm{A}} - \mu_{\mathrm{V}}) = -\mathcal{L}\,\nabla\mu_c = -\mathcal{L}\,\nabla\frac{\delta\mathscr{F}}{\delta c}, \tag{5.5}$$

where $\mathscr{F}$ is the free energy of the adsorbed atoms. Thus, an explicit expression for this functional is needed to obtain. Here we consider $\mathscr{F}$ having two part,

$$\mathscr{F} = \mathscr{F}_a + \mathscr{F}_s, \tag{5.6}$$

where the subscripts of a and s denote the local nearest-neighbor (N-N) interaction between adatoms and the global interactions from the substrate, respectively.

6 Nearest-Neighbor Interactions

Due to the atomistic nature of the N-N interactions between individual adatoms, as mentioned in Section 4.2 statistical physics is usually applied to formulate the free energy $\mathscr{F}_a$. When the spatial fluctuations of the coverage about its mean value are small, it is convenient to introduce a mean-field approximation in which a fluctuating local coverage is replaced by a spatially uniform average value. In the monolayer atomic clustering problem, the model should be understood to describe the very early nucleation stage of cluster evolution after the wetting layer is formed. Thus the mean-field approximation applied in the following model is a valid assumption. It is known that there are formulations of mean-field theory for

an Ising system, such as the Bragg-Williams and variational mean-field theories. In the current section, the Bragg-Williams approach will be presented. The model with a variational mean-field theory which is more versatile and elegant has been developed by D. Walgraef [79] illustrated in details in Appendix A.

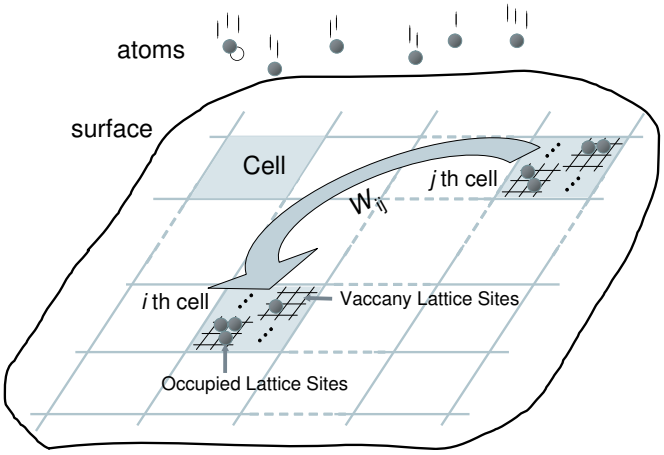

Figure 6.1: Bragg-William approach in the phase field modelling.

For a macroscopic surface area, we can imagine dividing it into a set of mesoscopic cells. Each cell can be treated via statistical mechanics as a grand canonical ensemble, which means it exchanges energies and particles with other cells. Here we assume that only two-body interactions between adatoms are important. As shown in Figure 6.1 considering the i^{th} mesoscopic cell, the number of substrate sites and the number of adsorbates within the cell are respectively denoted by $N_S^{(i)}$ and $N_A^{(i)}$. The total number of possible states in this cell, that is the partition function $\mathcal{Z}^{(i)}$ can be written as:

$$\mathcal{Z}^{(i)} = \frac{N_S^{(i)}!}{N_A^{(i)}!\left(N_S^{(i)} - N_A^{(i)}\right)!}\left[\prod_{j=1}^{N_{cell}} \exp\left(-\frac{\mathscr{V}_e^{(ij)}}{k_B T}\right)\right] \cdot \mathcal{Z}_s^{(i)}, \tag{6.1}$$

where N_{cell} denotes the total number of cells; $\mathscr{V}_e^{(ij)}$ is an effective elastostatic interaction energy between the i^{th} and j^{th} cells, which is an interaction energy

mediated via the substrate; $\mathscr{Z}_s^{(i)}$ denotes the partition function due to all the other interactions. Furthermore, if we apply the mean field approximation on cells and define $\mathscr{W}^{(ijk)}$ as an effective pair interaction energy between the j^{th} cell and the k^{th} ad-particles in the i^{th} cell, then

$$\mathscr{V}_e^{(ij)} = \sum_{k=1}^{N_A^{(i)}} \frac{N_A^{(j)}}{N_S^{(j)}} \mathscr{W}^{(ikj)}. \tag{6.2}$$

If the adatoms in each cell are assumed to be distributed randomly, we can further write Equation (6.2) with the effective pair interaction energy between the i^{th} cell and the j^{th} cell as:

$$\mathscr{V}_e^{(ij)} \approx N_A^{(i)} \left(\frac{N_A^{(j)}}{N_S^{(j)}} \right) \mathscr{W}^{(ij)}. \tag{6.3}$$

Using Sterling formula, the N-N free energy of the i^{th} cell can be obtained[†]:

$$\begin{aligned}
\mathscr{F}_a^{(i)} &= -k_B T \ln Z_a^{(i)} \\
&= -k_B T \Bigg\{ N_S^{(i)} \ln N_S^{(i)} - N_A^{(i)} \ln N_A^{(i)} - \left(N_S^{(i)} - N_A^{(i)} \right) \ln \left(N_s^{(i)} - N_A^{(i)} \right) \\
&\qquad - \sum_{j=1}^{N_{cell}} \frac{N_A^{(j)}}{N_S^{(j)}} \frac{N_A^{(i)} \mathscr{W}^{(ij)}}{k_B T} \Bigg\} \\
&= k_B T \left\{ N_A^{(i)} \ln \frac{N_A^{(i)}}{N_S^{(i)}} + \left(N_S^{(i)} - N_A^{(i)} \right) \ln \frac{N_S^{(i)} - N_A^{(i)}}{N_S^{(i)}} + \sum_{j=1}^{N_{cell}} \frac{N_A^{(j)}}{N_S^{(j)}} \frac{N_A^{(i)} \mathscr{W}^{(ij)}}{k_B T} \right\}.
\end{aligned} \tag{6.4}$$

Considering the concentration in this cell c_i, which is N_A/N_S, the free energy per substrate lattice point is:

[†]This step signifies that the model is not a motion-based but a state-based approach.

$$
\begin{aligned}
f_a^{(i)} &= k_B T \left\{ \frac{N_A^{(i)}}{N_S^{(i)}} \ln \frac{N_A^{(i)}}{N_S^{(i)}} + \frac{\left(N_S^{(i)} - N_A^{(i)}\right)}{N_S^{(i)}} \ln \frac{N_S^{(i)} - N_A^{(i)}}{N_S^{(i)}} + \sum_{j=1}^{N_{cell}} \frac{N_A^{(j)}}{N_S^{(j)}} \frac{N_A^{(i)}}{N_S^{(i)}} \mathscr{W}^{(ij)} \right\} \\
&= k_B T \left\{ c_i \ln c_i + (1 - c_i) \ln (1 - c_i) + \sum_j c_i c_j \mathscr{W}_{ij} \right\}. \qquad (6.5)
\end{aligned}
$$

The total free energy of a system becomes:

$$
\mathscr{F}_a = k_B T \sum_i \left\{ c_i \ln c_i + (1 - c_i) \ln (1 - c_i) + \sum_j c_i c_j \mathscr{W}_{ij} \right\}. \qquad (6.6)
$$

Using the relation: $2c_i c_j = c_i^2 + c_j^2 - (c_i - c_j)^2$,

$$
\mathscr{F}_a = k_B T \sum_i \left\{ c_i \ln c_i + (1 - c_i) \ln (1 - c_i) + \frac{1}{2} \sum_j \mathscr{W}_{ij} c_i^2 - \frac{1}{4} \sum_{ij} \mathscr{W}_{ij} (c_i - c_j)^2 \right\}. \qquad (6.7)
$$

The continuum expression can be obtained by taking the continuous limit of the above discrete one ($\sum_i \to \int d\mathbf{r}$, $c_i \to c(\mathbf{r})$, and $\mathscr{W}_{ij} \to \epsilon^{(a)}(\mathbf{r}, \mathbf{r}')$), in which we transit from an average over a collection of lattice sites to an average over coarse-grained cells. Assuming that we only consider nearest-neighbor interactions (e.g. $\epsilon^{(a)}(\mathbf{r}, \mathbf{r}') \approx -\gamma\epsilon\, \delta(|\mathbf{r} - \mathbf{r}'| = a)$ where γ is the lattice coordination number, ϵ is the pair interaction energy and a is the lattice constant, we could obtain the interfacial terms using the fact that

$$
\begin{aligned}
c(\mathbf{r})^2 + c(\mathbf{r}')^2 - (c(\mathbf{r}) - c(\mathbf{r}'))^2 &= 2c(\mathbf{r})c(\mathbf{r}') \\
\int_{\mathrm{S}} d\mathbf{r}'\, \gamma\epsilon\, \delta(|\mathbf{r} - \mathbf{r}'| - a) c(\mathbf{r}')^2 &\approx \gamma\epsilon c(\mathbf{r})^2 \\
\int_{\mathrm{S}} d\mathbf{r}'\, \gamma\epsilon\, \delta(|\mathbf{r} - \mathbf{r}'| - a) [c(\mathbf{r}) - c(\mathbf{r}')]^2 &\approx a^2 \gamma\epsilon |\nabla c(\mathbf{r})|^2.
\end{aligned}
$$

Finally we have [79]

$$\int_S d\mathbf{r}'\epsilon^{(a)}(\mathbf{r},\mathbf{r}')c(\mathbf{r})c(\mathbf{r}') = -\epsilon_0 c(\mathbf{r})^2 + \xi_0^2|\nabla c(\mathbf{r})|^2, \tag{6.8}$$

in which $\epsilon_0 = \gamma\epsilon$, $\xi_0^2 = a^2\gamma\epsilon$ and the integral is taken over the surface.

Thus Equation (6.7) becomes

$$\mathscr{F}_a = \int_S d\mathbf{r}\left[k_{\mathrm{B}}Tf(\mathbf{r}) - \frac{1}{2}\epsilon_0 c(\mathbf{r})^2 + \frac{1}{2}\xi_0^2|\nabla c(\mathbf{r})|^2\right], \tag{6.9}$$

where $f(\mathbf{r}) = [1-c(\mathbf{r})]\ln[1-c(\mathbf{r})] + c(\mathbf{r})\ln[c(\mathbf{r})]$.

And the chemical potential of N-N interactions is

$$\mu_a = k_{\mathrm{B}}T\ln\Big(\frac{c}{1-c}\Big) - \epsilon_0 c - \xi_0^2\nabla^2 c. \tag{6.10}$$

7 External Field Effects

We can treat the coverage-independent part of the substrate-mediated free energy by two-body interactions as we did for N-N interactions, which finally will lead to an integral term similar to that in Equation (6.8). This treatment is physically equivalent to considering the adatoms as point defects. Although the formulation is successfully adopted in describing structural transformations in solids [30, 80], the situation is different on the surface. Both the energy calculation [36] and the Monte Carlo simulation carried out in Chapter VI show that this point-defect type interaction on the surface will be so small that it can be completely neglected. However, the interaction between atomic clusters on the surface must be taken into account. Here, we adopt a continuum approach as a convenient way to formulate this many-body interaction effect. The discontinuity of intrinsic

surface stress between adatom clusters and the substrate provide a large driving force to self-organization [65, 1].

On the edge of a cluster, the discontinuity can be replaced by a pair of tangential force dipoles as Marchenko and Parshin indicated [41]. The relation between the force density (f_α) and surface intrinsic stresses ($\sigma_{\alpha\beta}$) is well-known in elasticity theory as:

$$f_\alpha(\mathbf{r}) = \frac{\partial \sigma_{\alpha\beta}(\mathbf{r})}{\partial x_\beta}. \tag{7.1}$$

where the subscripts of α and β denotes the indices (1 or 2) on the surface and the repeated index implies to be a summation index. In our monolayer model, the intrinsic stress of clusters is understood as being effective, and is a function of the concentration at position $\mathbf{r}$. To first order approximation [35], it follows from Vegard's law that we have:

$$\sigma_{\alpha\beta}(\mathbf{r}) = \sigma_{\alpha\beta}\, c(\mathbf{r}), \tag{7.2}$$

where $\sigma_{\alpha\beta}$ is considered to be a material constant on the homogeneous substrate surface. In the isotropic case where

$$\sigma_{\alpha\beta} = \sigma \delta_{\alpha\beta}, \tag{7.3}$$

the free energy induced by the substrate can be generally expressed as the force times the displacement ($\mathbf{u}$) [1]

$$\mathscr{F}_{s0} = -\int_S d\mathbf{r}\, f_\alpha\, u_\alpha = -\int_S d\mathbf{r}\, [\sigma \nabla_\alpha c(\mathbf{r})]\, u_\alpha. \tag{7.4}$$

Thus using the interchangable property of the derivative and variational operators and integrating it by parts with Gauss's Thoerem, the chemical potential which is the variational derivative of the free energy simply becomes:

$$\mu_s(\mathbf{r}) = \sigma u_{\alpha,\alpha}\,. \tag{7.5}$$

Here, if we ignore the interactions between adatom clusters and apply a nonuniform displacement field on the surface, we obtain a non-variable part of μ^s which is independent of the concentration as

$$\mu_{s0}(\mathbf{r}) = \sigma\big[\varepsilon_{xx}(\mathbf{r}) + \varepsilon_{yy}(\mathbf{r})\big]. \tag{7.6}$$

where $\varepsilon_{\alpha\beta}$ is the external strain field in the substrate. According to Marchenko [41], the elastic energy per adatom is approximated as $\sigma_{\alpha\beta}\,\varepsilon_{\alpha\beta}$. It is easy to see that atomic clusters here are considered as parts of the substrate surface to store the elastic energy. It should be noted that by Equation (5.5), the term μ_{s0} is taken into account only when the field from the substrate is nonuniform. This means a uniform strain field, such as coherent lattice mismatch in heteroepitaxial structures will not influence a self-organized patterns on the surface.

8 Cluster-Cluster Interactions

If the effects of cluster-cluster interaction in Equation (7.5) are to be considered, we could express the long-range interaction term in the usual Green's function method by substituting Equation (7.2) in (7.1) without any external strain field on the substrate:

$$\mathscr{F}_{sc} = -\frac{1}{2}\iint d\mathbf{r}\, d\mathbf{r}' \sigma_{\alpha\mu} \nabla_{\mu} c(\mathbf{r}) G_{\alpha\beta}(\mathbf{r}-\mathbf{r}') \sigma_{\beta\nu} \nabla'_{\nu} c(\mathbf{r}'), \tag{8.1}$$

where the energy is defined to be positive for attractive interactions. $G_{\alpha\beta}(\mathbf{r}-\mathbf{r}')$ is the surface Green's function which denotes the displacement component α at position $\mathbf{r}'$ caused by a unit force acting at a position $\mathbf{r}$ in the direction β. It is also noted from the symmetry considerations that we must have

$$G_{\alpha\beta}(\mathbf{r}-\mathbf{r}') = G_{\alpha\beta}(\mathbf{r}'-\mathbf{r}) = G_{\beta\alpha}(\mathbf{r}-\mathbf{r}').$$

The formal method for the Green's function in half anisotropic materials is the Stroh formalism proposed by Ting [76] and Pan [56]. However, the Green's function $G_{\alpha\beta}(\mathbf{r},\mathbf{r}')$ for half-space elastic medium is given by Maradudin and Wallis by taking the Fourier transform over the x and y directions [40]:

$$G_{ij}(\mathbf{r},\mathbf{r}') = \int \frac{d^2\mathbf{q}}{(2\pi^2)} G_{ij}(\mathbf{q}|zz') \exp\left[\mathrm{i}\mathbf{q}\cdot(\mathbf{r}_{\shortparallel}-\mathbf{r}'_{\shortparallel})\right], \tag{8.2}$$

where $i,j = 1,2,3$. The subscripts of $\shortparallel$ denotes the surface components x and y. According to Maradudin et al. [40, 58], the Green's Function in the transformed space, $G_{ij}(\mathbf{q}|zz')$, which is defined with a vector basis, can be expressed as tensor components via rotating the coordinate space over the angle in the reciprocal space θ by the simple relation:

$$G_{ij}(\mathbf{q}|zz') = \sum_{mn} \mathcal{S}^{-1}_{im}(\theta)\, \mathcal{G}_{mn}(q|zz')\, \mathcal{S}_{nj}(\theta). \tag{8.3}$$

The transformation matrix $\boldsymbol{\mathcal{S}}$ is given by

$$\boldsymbol{\mathcal{S}} = \begin{pmatrix} \cos\theta & \sin\theta & 0 \\ -\sin\theta & \cos\theta & 0 \\ 0 & 0 & 1 \end{pmatrix} \qquad \boldsymbol{\mathcal{S}}^{-1} = \begin{pmatrix} \cos\theta & -\sin\theta & 0 \\ \sin\theta & \cos\theta & 0 \\ 0 & 0 & 1 \end{pmatrix}, \tag{8.4}$$

where $\cos\theta = q_x/q$, $\sin\theta = q_y/q$. It is also noted that the functions $\mathcal{G}(q|zz')$ depend only on the magnitude of (q_x, q_y).

For a semi-infinite isotropic elastic medium occupying the half-space $z > 0$ and bounded by a stress-free surface at the plane $z = 0$, the speeds of sound for transverse and longitudinal waves c_t and c_l are related to Lamé coefficients μ and λ as

$$c_l = \sqrt{\frac{(\lambda + 2\mu)}{\rho}} \qquad \text{and} \qquad c_t = \sqrt{\frac{\mu}{\rho}}, \tag{8.5}$$

where ρ is the density of the material. For reference, we list the conversion relations between the shear modulus μ, the Poission ratio ν, and the stiffness matrix components (c_{11} and c_{12}) for an isotropic material as:

$$\mu = c_{44} = \frac{1}{2}(c_{11} - c_{12}); \qquad \lambda = c_{12} = \frac{2\mu\nu}{1 - 2\nu}. \tag{8.6}$$

All the components of the tensor $\mathcal{G}_{mn}(q|zz')$ for an isotropic material can be explicitly calculated in an analytical form and are listed in Appendix B. For an anisotropic crystal with cubic symmetry, explicit solutions can be numerically obtained by the formulations presented in Maradurin's papers [40].

Using the same techniques as in deriving Equation (7.6) and applying the isotropic condition (Equation 7.3), we obtain the variable part of chemical potential (μ_{sc}) as

$$\mu_{sc} = \sigma^2 \int_S d\mathbf{r}' \Big[\nabla_\alpha G_{\alpha\beta}(\mathbf{r} - \mathbf{r}') \, \nabla'_\beta c(\mathbf{r}') \Big]. \tag{8.7}$$

Substituting Equations (6.10), (7.6) and (8.7) into Equation (5.5) and then into (5.1), we finally have the kinetic equation of the model

$$\begin{aligned} \partial_t c &= \frac{1}{\tau}(c_0 - c) + \frac{D_0}{k_\mathrm{B}T} \nabla^2 \Bigg[k_\mathrm{B}T \ln\Big(\frac{c}{1-c}\Big) - \epsilon_0 c - \xi_0^2 \nabla^2 c \\ &\quad + \sigma a^2 \big[\varepsilon_{xx}(\mathbf{r}) + \varepsilon_{yy}(\mathbf{r}) \big] + \sigma^2 a^4 \int d\mathbf{r}' \, \nabla_\alpha G_{\alpha\beta}(\mathbf{r} - \mathbf{r}') \, \nabla'_\beta c(\mathbf{r}') \Bigg], \end{aligned} \tag{8.8}$$

where $c_0 = \alpha/(\alpha + \beta)$, and $\tau^{-1} = \alpha + \beta$[†]. The introduction of the square of the lattice constant a^2 per surface stress is by consideration of appropriate units. It is important to note that each term in the above equation is per atom and that we evaluate the long-range terms by averaging over one lattice square.

[†]Here, α and β denotes the adsorption and desorption rates. It should be distinguished from the Greek subscripts as surface indices

CHAPTER IV

Development of Numerical Spectral Method

9 Global Interpolation

Due to the high nonlinearity in Equation 8.8, it is not feasible to pursue any analytical solution of the problem. The first choice for a numerical solution to Equation 8.8 is the finite difference (FD) method. For Cahn-Hilliard type PDEs, a splitting scheme in the FD method can guarantee the accuracy of high order derivatives [19]. A multigrid method can also be implemented in the FD scheme to obtain a good balance between ultra-fine spatial grids and the efficiency of computations. The splitting scheme and multigrid methods are using a "local" interpolation of the data of adjacent points. These methods are good choices if the geometry of the system is extremely irregular with complex boundary conditions.

However if the problem has a simple geometry and periodic boundary conditions, spectral methods become a better choice. In contrast to the local interpolation in FD methods, the spectral method relies on "global" interpolation of data with grid points over the whole domain. The key here is to represent the unknown function with a group of basic known functions. This function representation is very analogous with vector representation by a set of linearly independent vectors. By the *orthogonality* of these basis functions, the problem is converted to solving the corresponding coefficients. Actually the numerical integration methods with various Guassian quadratures also apply the global representation ideas.

The major advantage of spectral method is that it can give much better accuracy for solving certain classes of problems, such as the ability to completely eliminate aliasing effects[†]. With the emergence of the algorithm of Fast Fourier Transform (FFT) algorithm in the early 70's, spectral methods have been fully developed in numerical computations. Examples are psedo-spectral techniques for nonlinear terms in partial differential equations and the τ method for various boundary conditions. However, it should be mentioned again that the spectral approach is not useful in dealing with problems having complicated geometries[‡].

Mathematically, any function can be represented as:

$$f(x) = \sum_{q=-\infty}^{+\infty} \hat{f}_q \phi_q(x), \tag{9.1}$$

where $\phi_q(x)$ are basis or "trial" functions. They constitute a specific function space, such as the Fourior (trigmetric) space, Chebyshev space or Legendre space. $\hat{f}(q)$ are the coefficients in the function space. Basis functions are designed to be orthogonal by defining an inner product as:

$$\langle \phi_q, \phi_l \rangle = \int_a^b \phi_q(x) \phi_l^*(x) w(x)\, dx = 0 \qquad \text{if} \quad q \neq l. \tag{9.2}$$

Substituting Equation (9.1) in the inner product of $\langle f, \phi_q \rangle$ and using the orthognality of Equation (9.2), we obtain:

$$\hat{f}_q = \frac{\langle f, \phi_q \rangle}{||\phi_q||^2}, \tag{9.3}$$

[†]The term aliasing usually refers to the distortion that occurs due to the truncation of the nonzero wave vectors in the transformed space. It usually happens when a non-periodic problem is approximately treated to be periodic.

[‡]In this case, finite element methods (FEM) is of course a reasonable choice. But the main difficulty in FEM is to construct a proper Ginzburg-Landau free energy [5], especially for a nonlinear PDE in our problem.

and the function in real space can be expanded as a generalized Fourier series:

$$f(x) = \sum_{q=-\infty}^{+\infty} \frac{\langle f, \phi_q \rangle}{||\phi_q||^2} \phi_q(x). \tag{9.4}$$

The selection of a function space for a specific problem is much determined by its boundary conditions. If periodic boundary conditions are to be used, then Fourier functions are the best choice and $\phi_q(x) = e^{iqx}$. If the boundary is not periodic such that $-1 \leq x \leq 1$, a natural representation is with a Chebyshev polynomials, that is $\phi_q(x) = T_q(x)$ where $T_q(x) = \cos(q \cos^{-1} x)$. Although there are other classes of spectral representations for basis functions, such as Legendre polynomials etc., the Fourier and Chebyshev representations are the two most widely used classes in numerical calculations due to the development of FFT and cosine transform algorithms.

To make numerical computations of a differential equation with a global approximation, an important idea is to enforce a weak form of the problem. The weak form is commonly defined by the method of weighted residuals. Let us consider a very general differential equation:

$$\frac{\partial u}{\partial t} = \mathcal{L}(u) + \mathcal{N}(u), \tag{9.5}$$

where $\mathcal{L}$ and $\mathcal{N}$ denote the linear and nonlinear operators of the variable c, respectively. Suppose that the problem is 1-D, and that the B.C.'s are periodic with a period of 2π. Using the Fourier representation, we have:

$$u_N(x) = \sum_{q=-N/2}^{N/2-1} \hat{u}_q(t)\, e^{iqx}. \tag{9.6}$$

We define a residual of the problem $\mathcal{R}_N = \partial_t u_N - \mathcal{L}(u_N) - \mathcal{N}(u_N)$ and make:

$$\int_0^{2\pi} \mathcal{R}_N(x)\psi_q^*(x)\,dx = 0, \tag{9.7}$$

where $\psi_q(x)$ are test functions. Different spectral methods can arise with different classes of the test functions ψ_q. If the class of test functions is the same as the class of basis functions, we have the "Galerkin" method. With Equation (9.6) in Fourier space, it has $\psi_q(x) = e^{iqx}$. If we set the residual to zero at discrete points in physical space, the technique is called a "Collocation" method. It is easy to see that the Galerkin method allows the problem in the transformed and physical space to be converted only when the output is needed. In this context, we will just focus on the Galerkin approach. More precisely, we will develope the Fourier-Galerkin approach to solve the problem with periodic boundary conditions. The details of spectral methods, such as Chebyshev-Collocation-τ methods, can be found in the books by Canuto [12] and Gottlieb [21].

10 Application to the Kinetic Equation

First we illustrate the spectral method to formulate and numerically solve a typical isotropic Cahn-Hillard equation. Consider the following equation:

$$\partial_t c = M[\nabla^2 f(c) - \epsilon^2 \nabla^4 c], \tag{10.1}$$

where the boundary condition is periodic at $[0, 2\pi]$, and the initial condition is $c(x, y, 0) = c_0(x, y)$. M and ϵ are both constants. We use the Fourier-Galerkin approach:

$$c(x, y, t) = \sum_{q_x, q_y = -\frac{N}{2}}^{\frac{N}{2}-1} \hat{c}(q_x, q_y, t)\, e^{i(q_x x + q_y y)}. \tag{10.2}$$

Substituting the above equation into Equation (10.1) it is easy to see that if nonlinear terms are absent, Equation (10.1) converts to a set of de-coupled equations. However, if nonlinear terms are present, the solution results in coupled matrices, which are generally difficult to solve. For example, if the nonlinear term is quadratic, the number of operations will be on the order of N^4, which is too costly. Instead, since it is known that the number of operators in 2-D fast fourier transform algorithms is on order of $O(N^2 \log^2 N)$ [10], we can calculate nonlinear terms in physical space and then transform them back to Fourier space. This is what is called a "Psuedospectral" technique. Such a technique allows computations of the nonlinear terms economically, even when transforming data back and forth. However, it should be noted that psuedospectral methods will always induce aliasing of the data. For simple quadratic terms, such as $c\nabla c$, an additional technique named "3/2 rule" can be applied to completely eliminate aliasing effects [12]. For general situations, the easiest way to avoid aliasing is to choose N_x and N_y sufficiently large so that the largest frequency data become negligible.

Effectively, Equation (10.1) in numerical spectral methods has the same form as in the Fourier transform method:

$$\frac{d\hat{c}(\mathbf{q},t)}{dt} = -Mq^2\{\hat{f}(c)\}_{\mathbf{q}} - M\epsilon^2 q^4 \hat{c}(\mathbf{q},t), \tag{10.3}$$

where $q_x = -\frac{N_x}{2}, \ldots, \frac{N_x}{2} - 1$ and $q_y = -\frac{N_y}{2}, \ldots, \frac{N_x}{2} - 1$.

To make a time advancement, the explicit Euler scheme for time integration steps should always be avoided for numerical stability problems. No matter how small the time step (Δt) is, the simple explicit Euler scheme is unstable. The practical choice for a stable time marching scheme is either a semi-implicit second-order Adams-Bashforth/backward differentiation (AB/BDF [14]

or a semi-implicit Adams-Bashforth/Crank-Nicolson(AB/CN)) scheme [12]. The key idea of both methods is to treat linear operators implicitly and nonlinear operators explicitly. Specifically, to make nonlinear terms explicit, we can use Adams-Bashforth extrapolation as:

$$\{\hat{f}(c^n)\}_{\mathbf{q}} \simeq \frac{1}{2}\Big[\{\hat{f}(c^{n+1})\}_{\mathbf{q}} + \{\hat{f}(c^{n-1})\}_{\mathbf{q}}\Big]. \tag{10.4}$$

And the second-order BDF/AB scheme of Equation (10.3) is:

$$\begin{aligned}(3 + 2M\epsilon^2\Delta t q^4)\hat{c}^{n+1}(\mathbf{q}) &= 4\hat{c}^n(\mathbf{q}) - \hat{c}^{n-1}(\mathbf{q}) \\ &\quad + 2M\Delta t q^2\Big[2\{\hat{f}(c^n)\}_{\mathbf{q}} - \{\hat{f}(c^{n-1})\}_{\mathbf{q}}\Big]. \end{aligned}\tag{10.5}$$

For the first iteration step, the first-order semi-implicit scheme is applied:

$$(1 + \epsilon^2\Delta t q^4)\hat{c}^{n+1}(\mathbf{q}) = \hat{c}^n(\mathbf{q}) - M\Delta t q^2\hat{c}^n(\mathbf{q}). \tag{10.6}$$

Due to the convolutional form of the integral in Equation (8.7), we can write the kinetic equation (8.8) in the transformed space by denoting the variables in the Fourier space as subscripts of $\mathbf{q}$ as:

$$\begin{aligned}\partial_t c_{\mathbf{q}} &= \frac{1}{\tau}(c_{0\mathbf{q}} - c_{\mathbf{q}}) - \frac{D_0}{k_{\mathrm{B}}T}q^2\Bigg[\sigma a^2 \mathrm{Tr}(\boldsymbol{\varepsilon})_{\mathbf{q}} + k_{\mathrm{B}}T\Big\{\ln\Big(\frac{c}{1-c}\Big)\Big\}_{\mathbf{q}} \\ &\quad - \Big(\epsilon_0 + \xi_0^2 q^2 + \sigma^2 a^4 q_\alpha q_\beta G_{\alpha\beta}(\mathbf{q})\Big)c_{\mathbf{q}}\Bigg]. \end{aligned}\tag{10.7}$$

The corresponding equation (10.5) of the second-order scheme becomes:

$$\left[3+2\Delta t\left(\frac{1}{\tau}+\epsilon_0+\xi_0^2q^2+\sigma^2a^4q_\alpha q_\beta G_{\alpha\beta}(\mathbf{q})\right)\right]c_{\mathbf{q}}^{n+1}=$$
$$4c_{\mathbf{q}}^{n}-c_{\mathbf{q}}^{n-1}+2\Delta tD_0q^2\left[2\left\{\ln\left(\frac{c^n}{1-c^n}\right)\right\}_{\mathbf{q}}-\left\{\ln\left(\frac{c^{n-1}}{1-c^{n-1}}\right)\right\}_{\mathbf{q}}\right]$$
$$+2\Delta t\left[\frac{1}{\tau}c_{0\mathbf{q}}-\frac{D_0}{k_{\mathrm{B}}T}q^2\sigma a^2\mathrm{Tr}(\boldsymbol{\varepsilon})_{\mathbf{q}}\right]. \tag{10.8}$$

And the corresponding equation (10.6) of the first-order scheme is:

$$\left[1+\Delta t\left(\frac{1}{\tau}+\epsilon_0+\xi_0^2q^2+\sigma^2a^4q_\alpha q_\beta G_{\alpha\beta}(\mathbf{q})\right)\right]c_{\mathbf{q}}^{n+1}=$$
$$c_{\mathbf{q}}^{n}+\Delta tD_0q^2\left\{\ln\left(\frac{c^n}{1-c^n}\right)\right\}_{\mathbf{q}}+\Delta t\left[\frac{1}{\tau}c_{0\mathbf{q}}-\frac{D_0}{k_{\mathrm{B}}T}q^2\sigma a^2\mathrm{Tr}(\boldsymbol{\varepsilon})_{\mathbf{q}}\right]. \tag{10.9}$$

The steps for solving Equation (8.8) can be summarized in the following:

1. Transform the original equation into the Fourier space as Equation (10.7). Nonlinear terms can be considered as forcing terms.
2. Make the time and space discretization (Δt and N_x, N_y).
3. Use FFT to obtain c in Fourier space as $\hat{c}^n$.
4. Increase time from t to $t+\Delta t$.
5. Use FFT to obtain the nonlinear terms in the Fourier space as $\{\hat{f}(c)\}_{\mathbf{k}}$.
6. If it is the start of iteration, use Equation (10.9). Otherwise, use Equation (10.8).
7. Use the Inverse-FFT to obtain $\hat{c}^n$ in the physical space as c.

8. Update the nonlinear terms in the physical space using calculated value of c from Step 7.

9. Repeat step 4.

11 Parallel Computations

In a split-radix FFT algorithm [10], the data has to be divided into 2^n, where n is an integer appreciated with the grid size. This means that if the system in our problem becomes much bigger than the intrinsic characteristic wavelength, a grid of 512×512 or 1024×1024 or even more has to be used. The huge amount of data will require intensive computations, especially during back-and-forth FFT in the pseudo-spectral method for nonlinear terms in Equation (10.7). An efficient way to speed up calculations is to carry the heavy computational tasks over multiple processors, that is to utilize parallel computation techniques.

A direct method of parallel computations to solve the current PDE (Equation 10.7) is to replace the standard split-radix FFT subroutine for single processor to that for multi-processors without changing the main algorithm. There are some multiprocessor FFT algorithms can be used [75]. However, since unavoidable time consumptions for transferring the data speed up, it is easy to show that the FFT routine itself will not have a significant improvement if implemented on multiprocessors. A more convenient way is to manipulate some steps in the whole algorithm with multiple processors and keep the FFT routine in the single processor mode. One step that can be changed to a parallel mode is computing different pseudo-spectral terms. This means that the terms needed to make the FFT separately are submitted to different processors simultaneously. Another aspect that can be improved by parallel computing is the problem's dimension.

Since the surface problem has two dimensions, further computational task in the FFT routine for multidimensional problems can be further parallelized.

In the current problem, the multiprocessor algorithm exhibits both of the two aspects mentioned above. Since the present kinetic equation becomes completely decoupled in the Fourier-Garlerkin space, the first aspect is to carry out the calculations of $\hat{c}^{n+1}$ on spatial grid points of the discretized equation (10.7) over different processors simultaneously, that is to separate the total $N_x \times N_y$ spatial grids into m smaller regions. For example, processes will contain regions of $(0, N_x/m) \times N_y, (N_x/m + 1, 2N_x/m) \times N_y, \ldots, (N_x - N_x/m + 1, N_x) \times N_y$. The second aspect of parallel coding is how to handle pseudo-spectral terms, which requires the calculations to be taken back-and-forth between the spectral space and the physical space. Since the FFT routine adopted in our code is the split-radix code for 2-D problems, the parallel code developed here is to use every processor for one nonlinear term.

At the programming level, commonly used parallel methods include shared memory models, message passing models, thread models, and hybrid models etc. The message-passing paradigm is well suited for computing on distributed-memory machines, and is adopted in our parallel coding for the current problem. In the message-passing model, a set of tasks that use their own local memory during computation and the data exchange is performed by sending and receiving messages between different machines. Currently, there are two most frequently used tools for parallel programming according to the message-passing paradigm: PVM (Parallel Virtual Machine) and MPI (Message Passing Interface), in which the PVM is a comparatively older message-passing standard and the MPI has come into the mainstream more recently than the PVM and is now used as an industry standard. The parallel code of the current problem is written by the

MPI in `Fortran` 90. The "interface" in the MPI contains a rich set of pre-existing functions for performing point-to-point, many-to-one and many-to-many communications. Specifically in our code, besides the common functions of `MPI_Send` and `MPI_Recv`, collective communication commands are widely used. For example, the command `MPI_BCAST` is used for broadcasting (sending) various input parameters to every processor. The combination of the commands `MPI_Gather` and `MPI_Barrier` are used for sending the distributed data (such as the 2-D matrix of $\hat{c}^n(q_x, q_y)$) to process with the root while the combination of the commands `MPI_Scatter` and `MPI_Barrier` are used to distribute the date from the root to various processors.

It is easy to see that there is a possible drawback in the parallel algorithms proposed above, and that is the imbalance of the computational load among processors. One reason is that in the Fourier space, the wave vectors will quickly emerge to some characteristic value such that the computational region will not be needed for quickly decaying. Unbalanced computational tasks also occur when the amount of parallel linear terms is more than the pseudo-spectral nonlinear terms. Both of these situations can be avoided by carefully planning of the computational algorithm. However, it is found that if the number of processors is kept on the order of 4 to 6, we can achieve the required computational results without much trouble. For example, for a grid of 256×256 and using 4 processors, a full simulation can be generated within 2 days.

CHAPTER V

Simulation Results

12 Intrinsic Self-Organization with Cluster-Cluster Interactions

BEFORE we include all the effects of various interactions in an model (e.g. nearest-neighbor (N-N) interactions, cluster-external field (C-E) interactions and cluster-cluster (C-C) interactions), we consider the effects of C-C interactions on the natural self-organization behavior of surface clusters. Thus we assume that there is no applied external field ($\varepsilon_{\alpha\alpha} = 0$) or the external field is uniform ($\nabla^2\varepsilon_{\alpha\alpha} = 0$). More generally, Equation (8.8) can be written in a dimensionless form as:

$$\begin{aligned}\tau\partial_t\hat{c} &= (\hat{c}_0 - \hat{c}) \\ &\quad + \hat{D}\nabla^2\Bigg[-\frac{T_c}{T}\hat{c} + \frac{1}{4}\ln\Big(\frac{1+2\hat{c}}{1-2\hat{c}}\Big) - \frac{\xi_0^2}{4k_{\rm B}T}\nabla^2\hat{c} \\ &\quad + \frac{\sigma^2 a^4}{4k_{\rm B}T}\int d\mathbf{r}'\,\nabla_i G_{ij}(\mathbf{r}-\mathbf{r}')\,\nabla'_j\hat{c}(\mathbf{r}')\Bigg], \qquad (12.1)\end{aligned}$$

where $\hat{c} = c - \frac{1}{2}$, $\hat{D} = 4\tau D_0$ and $T_c = \epsilon_0/4k_{\rm B}$. Considering small perturbations ς about the steady state $\hat{c}_0$ ($\varsigma = \hat{c} - \hat{c}_0$), we can expand the entropy mixing term in a first order Taylor series and use the relation

$$\int d\mathbf{r}'\,\nabla_i G_{ij}(\mathbf{r}-\mathbf{r}')\,\nabla'_j\hat{c}(\mathbf{r}') \quad \longrightarrow \quad q_i q_j\big\{G_{ij}\big\}_{\mathbf{q}} c_{\mathbf{q}}$$

to rewrite Equation (12.1) in the Fourier space as

$$\tau\partial_t\varsigma(\mathbf{q}) = -\left[1+q^2\frac{\hat{D}^*T_c^*}{T}\left(\frac{T}{T_c^*}-1+A^2q^2 - B^2q_iq_jG_{ij}(\mathbf{q})\right)\right]\varsigma(\mathbf{q}), \tag{12.2}$$

where $T_c^* = T_c(1-4\hat{c}_0^2)$, $D^* = \hat{D}/(1-4\hat{c}_0^2)$, $A^2 = \xi_0^2/4k_{\mathrm{B}}T_c$ and $B^2 = \sigma^2/4k_{\mathrm{B}}T_c$. It can be seen that a dimensionless form of the governing equation recombines the various control parameters (such as τ, D_0, c_0, ϵ_0, σ, a etc.) into the above four parameters. The marginal stability curve is given by

$$T = q^2D^*T_c^*\frac{1-A^2q^2+B^2q_iq_jG_{ij}(\mathbf{q})}{1+q^2D^*}. \tag{12.3}$$

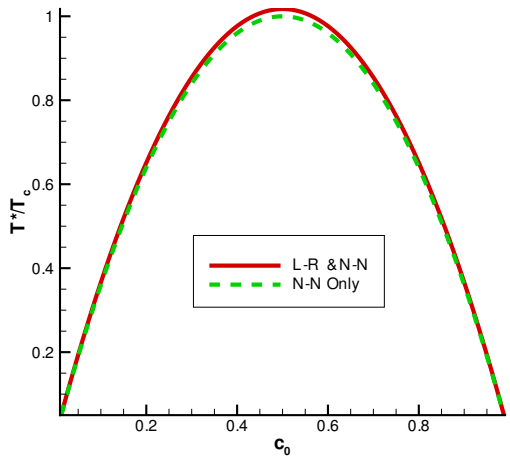

Figure 12.1: Comparison between the cases having only N-N terms and having both N-N and C-C terms.

After numerically calculating the maximum point of T in the above equation, we obtain the relation between the critical temperature T^* and the control parameter c_0. In Figure 12.1, we compare the two cases with N-N interactions

only and with both C-C and N-N terms respectively. It is shown that cluster-cluster interactions have a destabilizing effect. The maximum change occurring at $c_0 = 0.5$ is about $1.75\% T_c$.

Besides this destabilizing effects, C-C interactions have more important effects on patterning. In Figure 12.2, we compare the case with a small length scale of a surface ($100 \times 100\,\mathrm{nm}^2$) without external fields at an average coverage of $c_0 = 0.5$. The system should develop a stripe pattern [79], similar to the simulations of Proville [59]. It is noted that in the case of C-C interactions, stripes becomes sharper and are oriented along the anisotropy axes of the material. In Figure 12.3, the simulation is carried over a large system ($1 \times 1\mu m^2$) without dislocation network underneath the surface. It is seen by comparing with Figure 12.3 that with C-C interactions, the density of dots is increased but the average size of dots becomes smaller. Also the denuded zone is much sharper if no C-C interaction is presented.

13 Directed Self-Organization by Interfacial Dislocations

In this and next section, we will work out several examples for applying our phase field model with the external fields. Specifically, in this section, we will consider the external elastic field induced by interfacial dislocations in details and compare with the experimental results presented in Section 3.2. In the next section, we will present the theoretical modelling work for the external field generated by inclusions and electromagnetic laser fields.

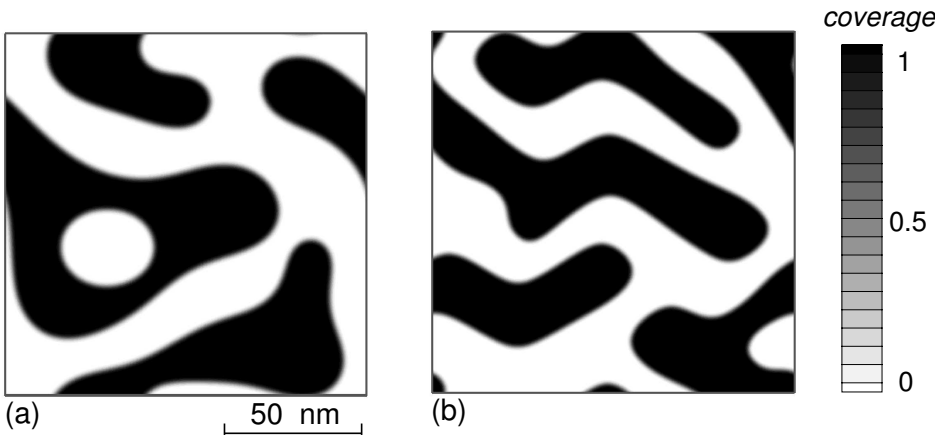

Figure 12.2: The equilibrium results at the time of 10 μs with the average coverage of $c_0 = 0.5$ where the gray scale is proportional to coverage. (a): N-N interactions only. (b): N-N and C-C interactions

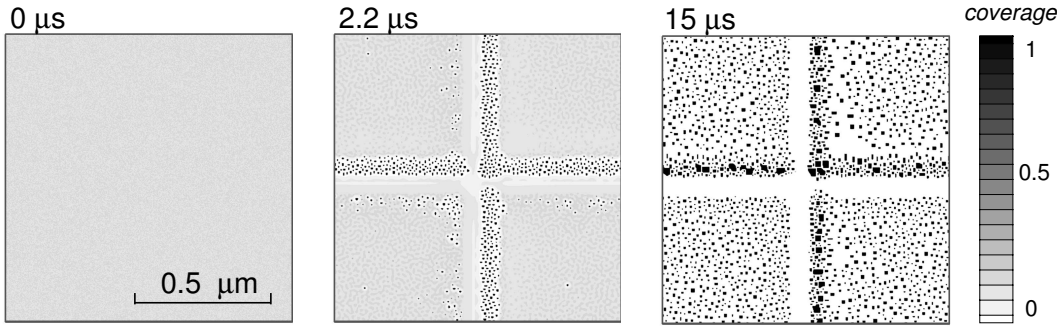

Figure 12.3: Cluster evolution process of N-N interaction only with two crossing interfacial dislocations buried at 80nm below the surface where the gray scale is proportional to coverage.

13.1 Elastic Field by Dislocations

An important application of the proposed dislocation model is the self-organization of Ge quantum dots on SiGe heteroepitaxial structures, where the external strain field is induced by an interfacial dislocation network in partially relaxed buffer layers, as shown in Section 3.2.

As shown in Section 7, the chemical potential induced by external fields (μ_{s0}) is independent of the local coverage and has the form of $\sigma u_{\alpha,\alpha}$. It can be shown that in some cases it is convenient to calculate this part by solving for displacement field since the derivative disappears in the Fourier-Galerkin transformed space. In the dislocation case, however, it would be straightforward to obtain μ_{s0} directly from the strain field.

In the present work, the model can be simplified as a system with a semi-infinite substrate and a thin film above it, where the interfacial dislocation in between is infinitely straight and is considered to be immobile. As mentioned in Section 3.2, the Burger's vector of interfacial dislocations is of the mixed type. But since screw components can induce only the shear strain, we see from Equation 7.6 that only edge components contribute to the strain interaction energy. Figure 13.4 shows a thin film and substrate structure with a single straight, infinitely long dislocation whose Burger's vector has only an edge component. Normally the two materials (film and substrate) have not only different elastic constants but also different lattice constants. Because of epitaxial deposition, a mismatch strain $\tilde{\varepsilon}_0$ will exist in both thin film and substrate. It is important to notice that this strain is stress-free (or by Mura's definition *eigenstrain*). The total strain on the surface can then be written as

$$\varepsilon_{\text{total}} = \varepsilon_{\text{mismatch}} + \varepsilon_{\text{dislocation}},$$

where $\varepsilon_{\text{dislocation}}$ is the strain induced by interfacial dislocations and $\varepsilon_{\text{mismatch}}$ is the strain induced by the mismatch strain $\tilde{\varepsilon}_0$. It should be emphasized that in the current model we assume both the interface and the top surface to be flat. In reality, the interface will be distorted into a wavy shape [37]. In the case of large distances between dislocations, however, the magnitude of distortion is so small that it can be neglected. As for the top surface, it usually becomes faceted and rough when the lattice mismatch is present. However, the deposition of a capping layer supplies additional atoms to fill in the troughs of the rough surface [32]. The presence of interfacial dislocations after the critical thickness is reached relaxes the deformation of surfaces induced by the lattice mismatch. Since $\tilde{\varepsilon}_0$ uniformly exists along the whole flat interface, it is easy to see that the relaxed strain ($\varepsilon_{\text{relax}}$) is also uniform along the flat surface. From the final kinetic equation (8.8), it has already been known that the spatially independent part of the field has no contribution to the equation.

The formal way to solve the elastic field generated from interfacial dislocations in multi-layer structures developed by Willis's method is to use the Fourier transform over the x and y directions and solve ordinary differential equations with the continuous and stress-free boundary conditions [17, 81]. However, in the present simulation we use a simplified approach by considering a 2-D plain-strain problem with an infinitely straight dislocation in a homogenous isotropic half-space material (Figure 13.4).

Using the complex variable representation method [74], we have the strain field given by a simple equation:

$$\varepsilon_{xx} = \frac{2}{\pi} \frac{(c_{11} - c_{12})}{(c_{11} + c_{12})} \frac{(b_x x + b_z h) x h}{(x^2 + h^2)^2}. \tag{13.1}$$

The elastic stiffness coefficients are set as $c_{11} = 15.79 \times 10^{11}$ erg/cm^3, $c_{12} =$

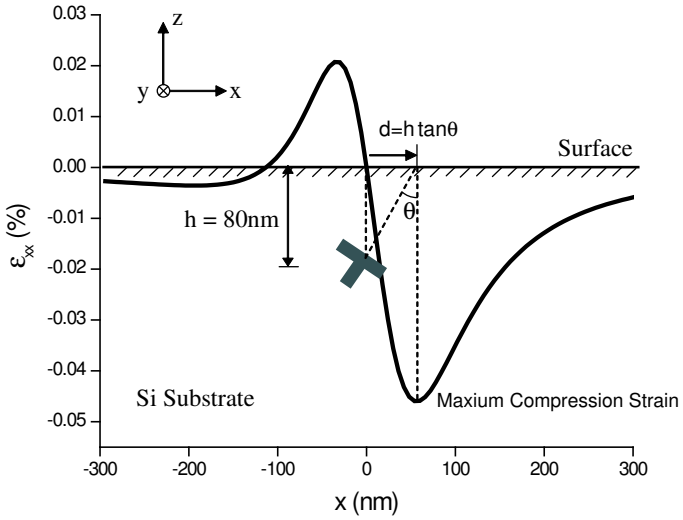

Figure 13.4: Surface strain field of an interfacial dislocation buried at 80nm underneath the Si surface, calculated by complex variable methods. The material parameters used is shown in Table C.1

6×10^{11} erg/cm^3 and $c_{44} = 7.65 \times 10^{11}$ erg/cm^3 for Si [24]. It should be noted that the interfacial dislocation is of the mixed type with both edge and screw components as shown in Figure 13.5.

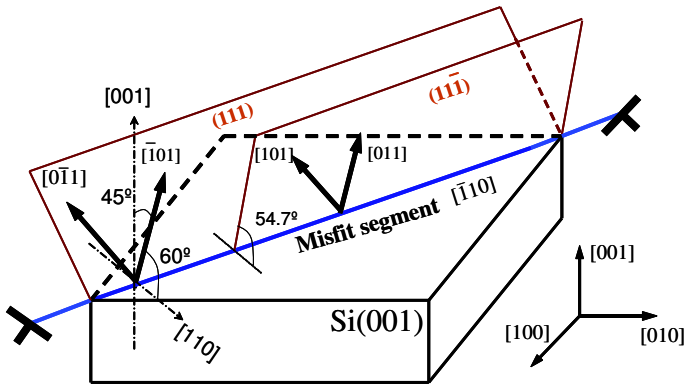

Figure 13.5: The slip planes of the interfacial dislocations with both edge and screw components

The edge component of the Burger's vector of an interfacial dislocation in a partially relaxed SiGe buffer layer is estimated directly from the equivalent lattice constants as $b_x \approx -1.93\,\text{Å}$ and $b_z \approx -2.73\,\text{Å}$, in which the negative sign means the extra half plane is downwards to infinity.

In Appendix C, we give a full solution of the elastic field by an interfacial dislocation in multi-layer structures [17, 81]. The effect of the inhomogeneity in the structure is shown to be very small in the case of the SiGe material system, as illustrated in Figure 13.6. Thus it is precise enough to use the simple solution by the complex variable methods instead of the full solution in our simulation. In addition, from Figure 13.6, it is noted that the maximum compressive region on the surface is not always at the intersection of slip plane with the surface plane. It depends on the Burger's vector orientation, the position of the extra half plane and the slip plane.

We may notice from the Figure 13.4 and Figure 13.6 that the position of

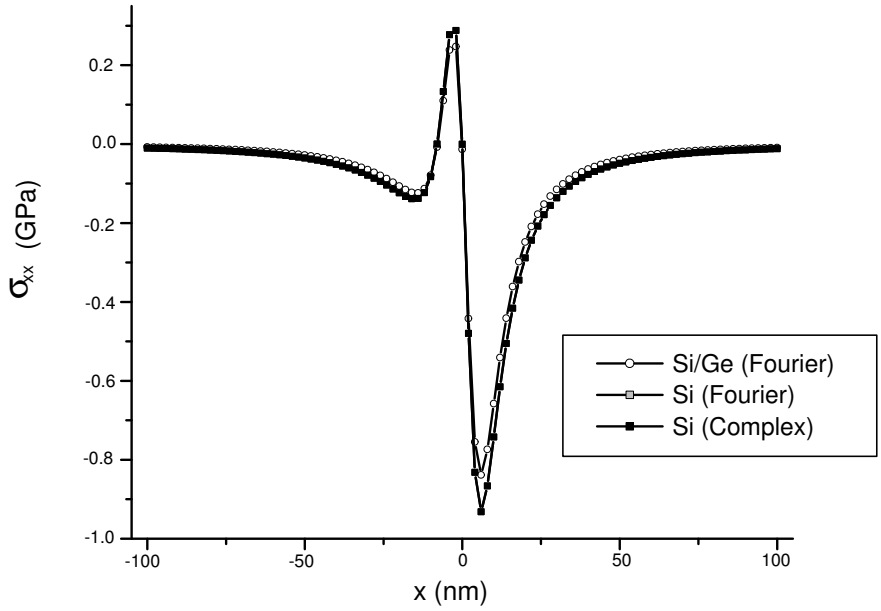

Figure 13.6: Comparison of σ_{xx} between inhomogeneous system (Si/Ge) and the homogeneous system (Si) with a single dislocation at 8nm below the surface.

the maximum compressive strain is at the intersection of the extension of the extra half plane and the surface. It can be shown that if the extra half plane is in the upper buffer layer, the maximum compressive region will be at the intersection of the slip plane and the surface. It is also found that the strain field decays to zero in the range of $1\,\mu$m. In the experiments of Kim *et al.*[32, 34], the distance between dislocations is about $9\,\mu$m. Thus, it is reasonable to use the single dislocation solution (Equation 13.1) as the periodic network solution if the length scale of the simulated surface is on the order $1\,\mu$m. As shown in the experiment, the distance between two parallel dislocations is usually on the order of μm, which is much larger than the thickness of the thin film. Thus it is reasonable to ignore the dislocation-dislocation interaction. For intersecting dislocations, it is noted that the component σ_{xx} is large if computed along the x-direction and small computed along the y direction. To a first approximation,

we can also ignore interactions between intersecting dislocations that comprise an interfacial network. If the solution is determined in $z-y$ plane, then by making the coordinate transformation: $x \rightarrow z$ and $y \rightarrow y$, the elastic field is obtained for $w^{(i)}$, $v^{(i)}$, $\sigma_{yy}^{(i)}$, $\sigma_{zz}^{(i)}$, $\sigma_{yz}^{(i)}$ according to the dislocation array in $z-y$ plane.

Solutions for dislocation networks can be constructed by superposing single dislocation solutions given above. Assuming $d_x^{(k_x)}$ and $d_z^{(k_z)}$ are the k^{th} dislocations' locations along the x and z directions, respectively, the solution becomes:

$$\begin{aligned} u_{xi} &= \sum_{k=1}^{n_x} u_{xi}\left(x-d_x^k, y\right), \\ u_{yi} &= \sum_{k_x=1}^{n_x}\sum_{k_z=1}^{n_y}\left[u_{yi}\left(x-d_x^{k_x}, y\right)+u_{yi}\left(z-d_z^{k_z}, y\right)\right], \\ u_{zi} &= \sum_{k=1}^{n_z} u_{zi}\left(z-d_z^k, y\right). \end{aligned} \tag{13.2}$$

In the $x-y$ plane problem, since an edge dislocation line is along the z-direction, the deformation along the z direction is zero, which implies a plain strain state. It is the same for the $z-y$ plane. Hence, we have:

$$\begin{aligned} \sigma_{xx} &= \sum_{k_x=1}^{n_x}\sum_{k_z=1}^{n_y}\left[\sigma_{xx}\left(x-d_x^{k_x}, y\right)+\nu\sigma_{zz}\left(z-d_z^{k_z}, y\right)\right], \\ \sigma_{yy} &= \sum_{k_x=1}^{n_x}\sum_{k_z=1}^{n_z}\left[\sigma_{yy}\left(x-d_x^{k_x}, y\right)+\sigma_{yy}\left(z-d_z^{k_z}, y\right)\right], \\ \sigma_{zz} &= \sum_{k_x=1}^{n_x}\sum_{k_z=1}^{n_y}\left[\sigma_{zz}\left(x-d_x^{k_x}, y\right)+\nu\sigma_{xx}\left(z-d_z^{k_z}, y\right)\right]. \end{aligned} \tag{13.3}$$

A calculated stress map with a capping layer for a 80 nm-thick film is shown in Figure 13.7.

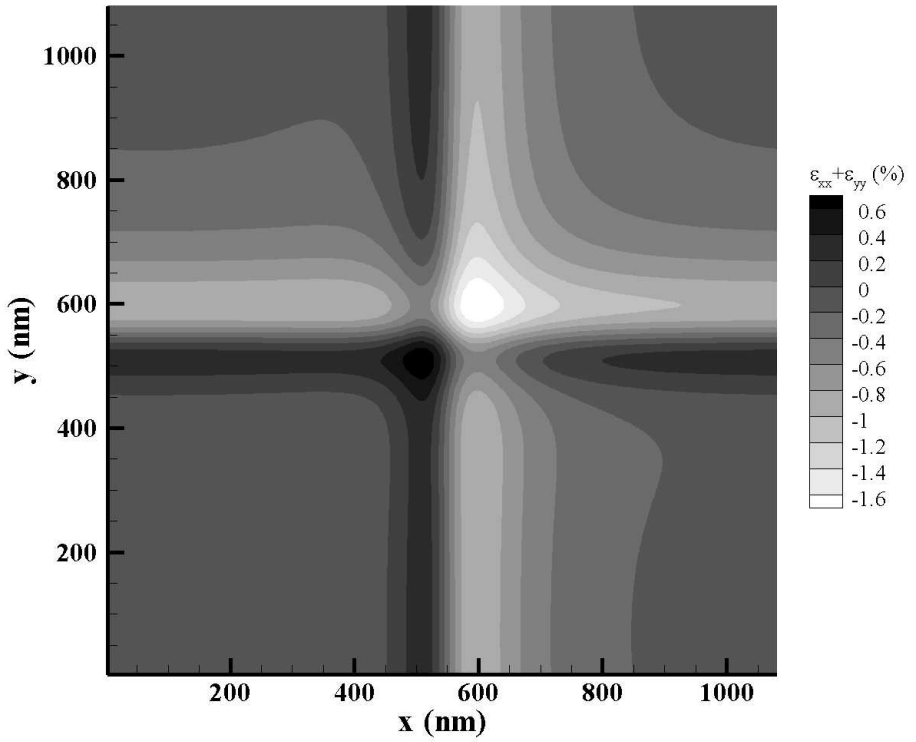

Figure 13.7: Strain field for a thin film structure of 1×1 interfacial dislocation buried at 80nm away from buffer layer.

13.2 Results and Comparisons with Experiments

To illustrate the predictive capabilities of our model, we consider Ge atoms are deposited on a $Si_{0.75}Ge_{0.25}$ substrate. The lattice constant for Ge, a, is 5.06 Å at room temperature. We take the Ge-Ge bond energy to be 0.3 eV where the experimental conditions of Kim *et al.*[34]. The adsorption and evaporation rates are assumed to be $1.67 \times 10^{-5}\,\mathrm{cm^2 s^{-1}}$ and $1.67 \times 10^{-6}\,\mathrm{cm^2 s^{-1}}$, respectively. The surface diffusion of Ge adatoms is strongly dependent on the temperature T and the coverage c. For hopping types of motion, it is reasonably assumed that $D_s = D_0\, c(1-c)$. However this dependence should only change the linear stability analysis quantitatively. For diffusion induced by thermally activated atomic jumps and at low temperatures, we should have $D_s = D_0 \exp(-E_s/T)$ [79]. We take $D_0 = 2.57 \times 10^{-7}\mathrm{cm^2 s^{-1}}$ [33]. For calculations related to elastic interactions, we use the intrinsic surface stress σ as 100 meVÅ^{-2} for Ge(001), which is assumed to be equal to the Si(001) 2×1 surface by an order-of-magnitude estimation [65].

It should be noted that from Walgraef's results [79], the characteristic length of self-organized patterns without the external perturbation is only on the order of 10nm. Compared with the length scale of the stress field from interfacial dislocations, the difference of dot- or stripe- patterns will not be obvious. For convenience the present work will be focused on an average coverage c_0 below the critical coverage in which the so-called 0 hexagons of dot pattern are selected. In practice, we choose $c_0 = 0.0025 \sim 0.15$. In real experiments, Ge quantum dots are deposited with Ge coverage ranging from 3Å to 12Å and then quenched to room temperature. Since the above formulation is for monolayer cluster formation and the Ge wetting-layer thickness is approximately 3ML $\approx$ 4.2Å [53], the dynamic process in our model should be understood as the nucleation stage after a perfect wetting layer has formed at room temperature. In the following results, the $1\,\mu\mathrm{m}^2$

surface is divided into 256×256 grid points, which keeps at least 2 points in the intrinsic characteristic length of the self-organized pattern.

All of our simulations begin with a small perturbation around c_0. Figure 13.8, Figure 13.9 and Figure 13.10 show the kinetic evolution processes for $c_0 = 0.025$, $c_0 = 0.05$ and $c_0 = 0.15$ respectively. It is observed that during the first $10^{-1}\mu$s, a pattern quickly emerges with the intrinsic length scale of a self-organized structure. At the same time its global distribution is slightly adjusted by the external fields. As the evolution process continues, for $c_0 = 0.025$, the dots nucleate exclusively at the intersections of dislocation lines. However for $c_0 = 0.05$ all dots except those along dislocations are completely wiped out by the applied strain field at about $1\,\mu$s. Then a clear distribution of dots is formed along dislocation lines. For the case of $c_0 = 0.15$, the dots keep growing by association. The pattern becomes especially denser in the region with the maximum compressive field along the dislocations until reaching equilibrium. A blurred denuded zone with a length scale of the order of 0.1μm is formed in the maximum compression region on the other side of dislocations. These results clearly show the three quantitative stages of nucleation which is consistent with experimental AFM images [34].

In order to quantitatively describe different distributions of surface atomic clusters, we construct a quantity that is analogous to the mass moment of inertia:

$$I_{xx} = \int d^2r\,(x - x_c)^2 c(\mathbf{r}), \tag{13.4}$$

where x_c is the x component of the center of mass and is defined as

$$x_c = \frac{\int d^2r\, xc(\mathbf{r})}{\int d^2r\, c(\mathbf{r})}.$$

To make things clearer, we carry out calculations for one buried dislocation along y direction and compare the results with different average coverage c_0. In this

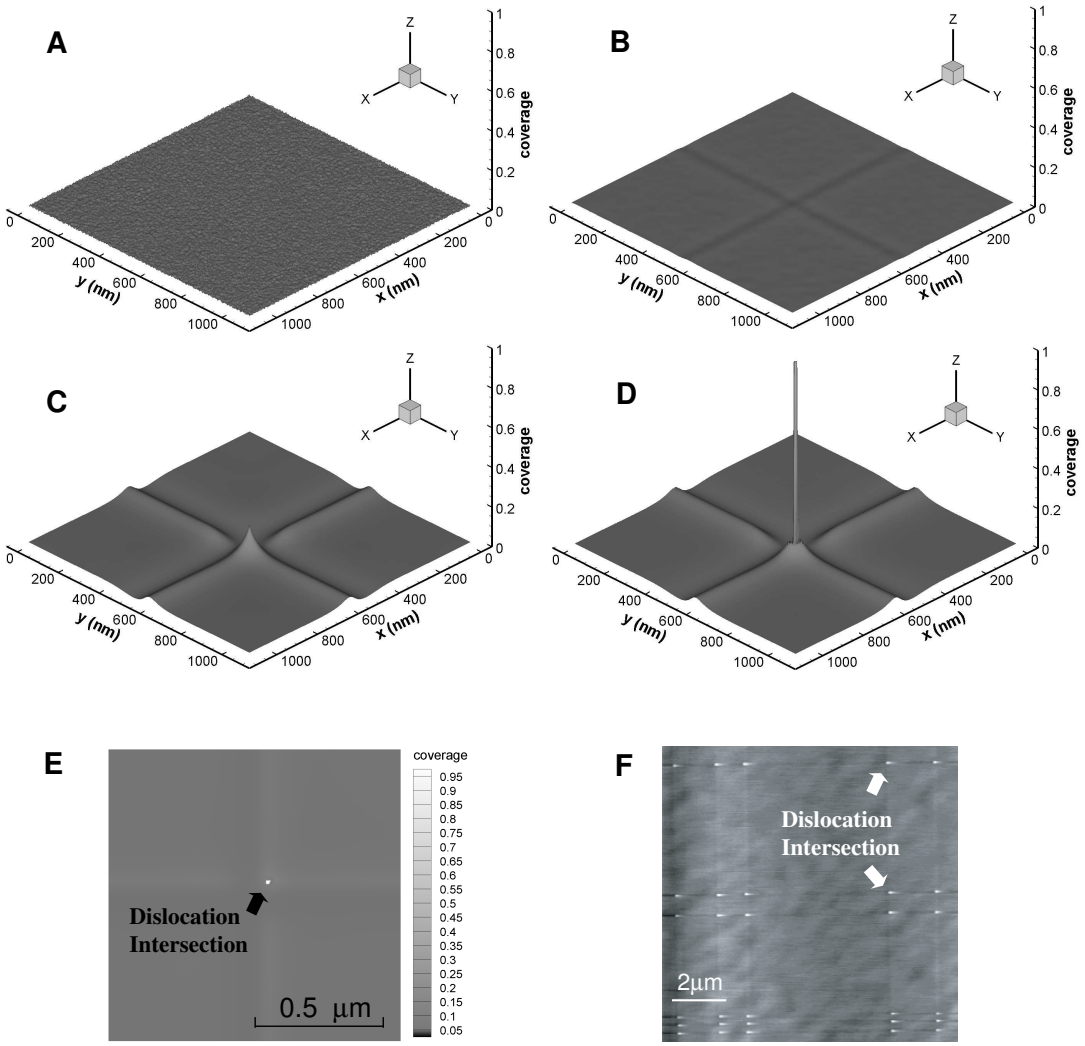

Figure 13.8: The evolution process of surface island formation by self-and-forced organization effects, starting with a small perturbation around $c_0 = 0.025$. The strain field is provided by two buried dislocations (along x and y direction and intersected at the center) at a depth of 80nm underneath the surface. (A) to (D) are the 3D-view simulation results at the time of $0\,\mu$s, $1.1\,\mu$s, $6.0\,\mu$s, and $9.3\,\mu$s, respectively. (E) is the equilibrium state in a 2D view at $9.3\,\mu$s. (F) is the experimental data by Kim et al. at the coverage of 4.0 Å [34] (i.e. $c_0 \sim 0$ Å).

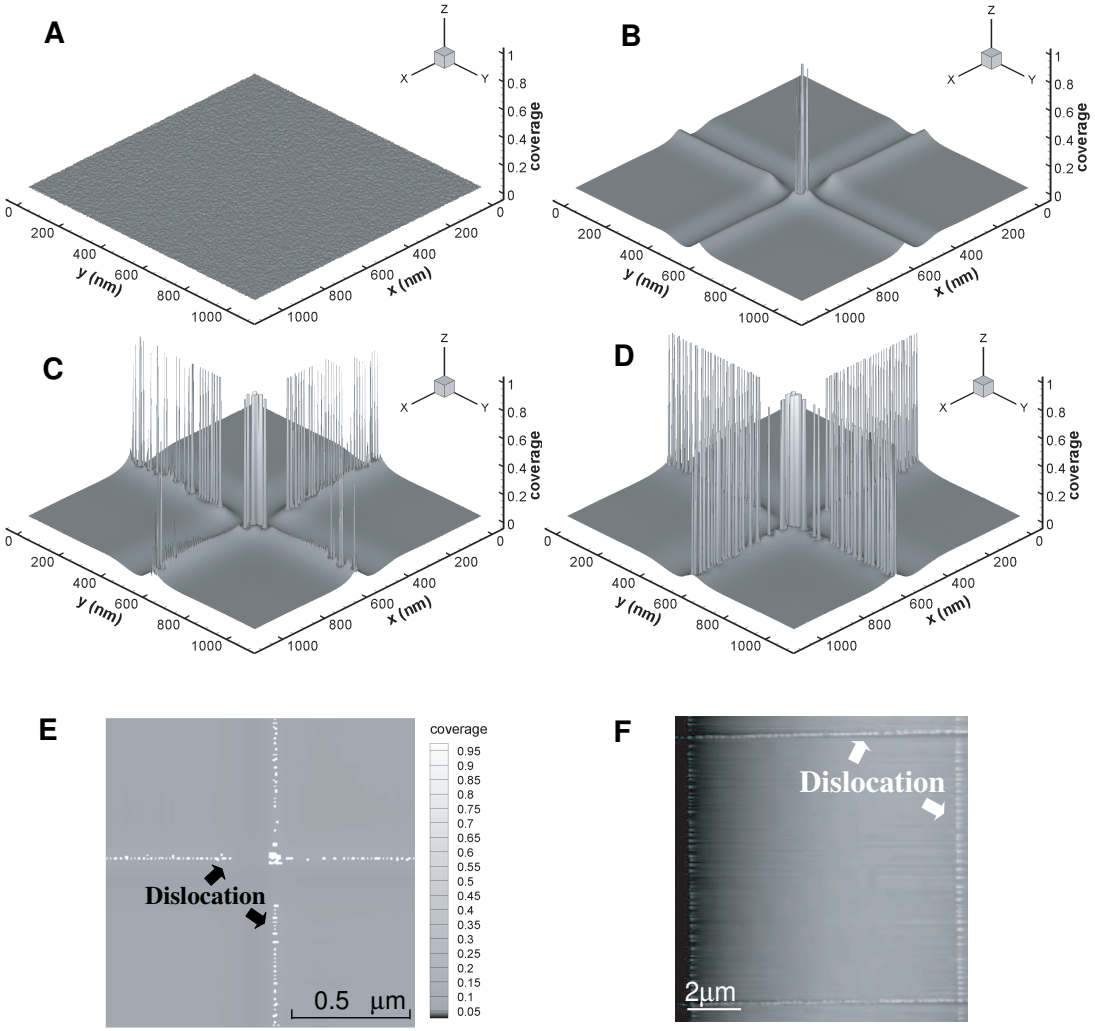

Figure 13.9: The evolution process of surface island formation by self-and-forced organization effects, starting with a small perturbation around $c_0 = 0.05$. The strain field is provided by two buried dislocations (along x and y direction and intersected at the center) at a depth of 80nm underneath the surface. (A) to (D) are the 3D-view simulation results at the time of $0\,\mu$s, $8.25\,\mu$s, $10.45\,\mu$s, and $15.95\,\mu$s, respectively. (E) is the equilibrium state in a 2D view at $18\,\mu$s. (F) is the experimental data by Kim et al. at the coverage of 4.5 Å [34] (i.e. $c_0 \sim 0.5$ Å).

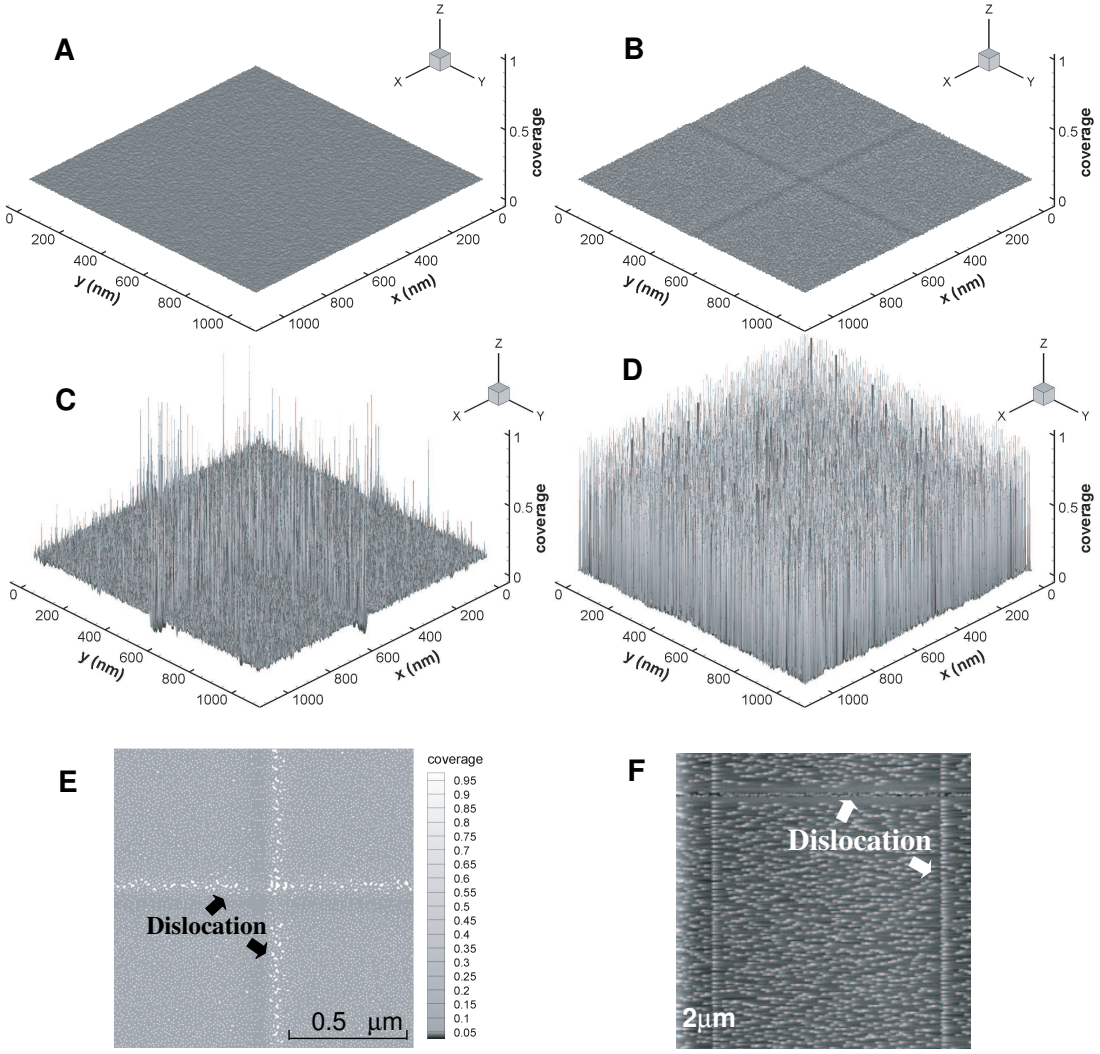

Figure 13.10: The evolution process of surface island formation by self-and-forced organization effects, starting with a small perturbation around $c_0 = 0.15$. The strain field is provided by two buried dislocations (along x and y direction and intersected at the center) at a depth of 80nm underneath the surface. (A) to (D) are the 3D-view simulation results at the time of $0\,\mu$s, $0.22\,\mu$s, $0.55\,\mu$s, and $1.1\,\mu$s, respectively. (E) is the equilibrium state in a 2D view at $10.45\,\mu$s. (F) is the experimental data by Kim et al. at the coverage of 6.0 Å[34] (i.e. $c_0 \sim 2$ Å).

case, the smaller the value I_{xx}, the larger the influence of the external field. It is shown in the Figure 13.11 that when c_0 is very small, say 0.01, the adatom cluster is uniformly distributed, and the distribution is shaped by the external field. In this case, instability does not take place and dots do not form. When c_0 increases to 0.05, an instability takes place and there will be a strong effect from the strain field at a time of about 10μs, and all stripes emerge into one sharp soliton profile. In this case, the forced-organized pattern becomes dominant. As c_0 is set to be larger than 0.05, say equals to 0.15, the self-organized pattern interacts with the forced pattern. It can be seen that there is a high density of atomic clusters on the maximum compression area along the dislocation line and a sparse distribution on the other area. It should be emphasized that the formation of the soliton profile is explained by the resonance of the wavevector and the amplitude of the external field and the unstable modes of the self-organized pattern-forming instability. This coupling is clearly a function of the average coverage c_0.

Although our simulation results show a good agreement to the observed experimental data, we have to point out that the applicability of the proposed phase-field theory is limited. As described in the previous chapters, the nearest-neighbor interaction chemical potential part in our continuum model is derived by the Bragg-Williams approach, which is based on the mean-field assumptions. It is a valid approximation only if the spatial fluctuations of the coverage about its mean value are small. However, since the deposition of atoms is usually extremely low in the real experiments($< 1\%$), it would become questionable whether a fluctuating local coverage can be replaced by a spatially uniform average value. Another limitation of our continuum theory is that we focus only on the monolayer system formed above the wetting layer. In reality, due to energetics of the adatoms and the effects of inter-layer diffusion the stable monolayer can hardly exist during the experiments. Thus, our model cannot provide any information

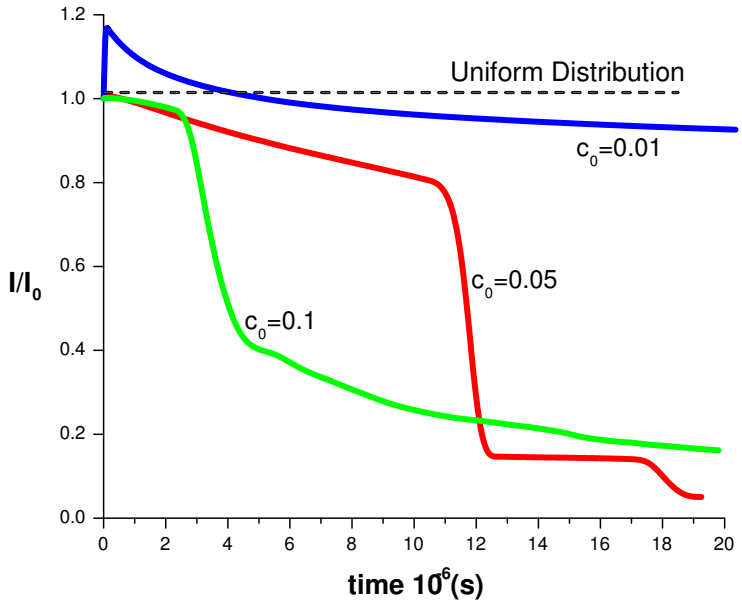

Figure 13.11: The mass moment of inertia as a function of time for a buried dislocation at 80nm depth from the surface and along the y direction.

about the information about the shape and facets of the dots. It can only be understood to provide the dynamic nucleation information during the early stage of deposition.

14 Directed Self-Organization by Other External Field

14.1 Periodic Inclusions

As shown in Section 7, the contribution of external strain to the chemical potential, which is the variational derivative of the free energy, can be written as:

$$\mu_{s0}(\mathbf{r}) = \sigma u_{\alpha,\alpha} = \sigma\left[\varepsilon_{xx}(\mathbf{r}) + \varepsilon_{yy}(\mathbf{r})\right]. \tag{14.1}$$

This is obviously independent of coverage. We can use a direct solution of

the strain field by infinite straight dislocations. However in the general case, the direct solution of the strain field is difficult, and it might require us to pursue the solution in a transformed Fourier space, and then transform it back to real space. Thus, a convenient way is to incorporate Equation 14.1 into the kinetic equation and solve for the displacement field in the transformed space. The Green's function method is a formal approach for an arbitrary elastic case, such as inclusions, dislocations and void lattices.

Formally, the displacement field induced by stress-free strain (eigenstrain) ε^*_{ij} can be expressed as an integral [54]:

$$u_\alpha(\mathbf{r}) = -\int_V d^3\mathbf{r}'\, C_{jlmn}\varepsilon^*_{mn}(\mathbf{r}')G_{\alpha j,l}(\mathbf{r}-\mathbf{r}'). \tag{14.2}$$

Note that in the above equation, the letter index represents the 3-D volume index on x, y and z. Since buried inclusions lie beneath the surface, then

$$\varepsilon^*_{mn}(\mathbf{r}) = \varepsilon^*_{mn}(\mathbf{r}_{\shortparallel}, z) \tag{14.3}$$

$$G_{ij,l}(\mathbf{r}-\mathbf{r}') = G_{ij,l}(\mathbf{r}_{\shortparallel}-\mathbf{r}'_{\shortparallel}; z, z'), \tag{14.4}$$

where the $\mathbf{r}_{\shortparallel}$ denotes a position vector along the surface (x and y direction). As mentioned before, the Green's Function in Fourier space can be obtained explicitly for the crystal with isotropic, cubic or hexagonal symmetries [40, 58]. General anisotropic cases can be investigated by the generalized Stroh foralism [76, 56].

For the stress-free strain $\varepsilon^*_{mn}(\mathbf{r})$, we assume that it is uniform and dilatational, which means:

$$\varepsilon^*_{mn}(\mathbf{r}_{\shortparallel}, z) = \varepsilon^*\vartheta(\mathbf{r}_{\shortparallel}, z)\delta_{mn}, \tag{14.5}$$

where δ_{ij} is Kronecker delta tensor and $\vartheta(\mathbf{r})$ is the shape function of the inclusion defined as [30]:

$$\vartheta(\mathbf{r}) = \begin{cases} 1 & \text{if } \mathbf{r} \text{ is inside the inclusion} \\ 0 & \text{otherwise.} \end{cases} \tag{14.6}$$

In the elastic inclusion case, where the elastic constants C_{ijmn} are assumed to be same as in the substrate, we have $\varepsilon^* = \Delta a/a$, where a is the lattice constant and Δa is the difference between the substrate and the inclusion. It is also noted that in a numerical sense, the above formulation also deals with a periodic boundary condition, which fit the requirement of the periodic void lattice structure.

Suppose that the material, except the inclusions, is homogenous. Due to the convolutional form in the above integration, the surface chemical potential in 2-D Fourier space ($\mathbf{q} = (q_x, q_y)$) can be simplified especially along x and y directions. For an isotropic material, substituting Equation (14.5) and (14.6) into Equation (14.2), we have

$$u_\alpha(\mathbf{r}) = -(c_{11} + 2c_{12})\varepsilon^* \int_V d^3\mathbf{r}'\, \vartheta(\mathbf{r}_{\shortparallel}; z') \big[G_{\alpha\beta,\beta}(\mathbf{r}_{\shortparallel} - \mathbf{r}'_{\shortparallel}; 0, z') + G_{\alpha\underline{z},\underline{z}}(\mathbf{r}_{\shortparallel} - \mathbf{r}'_{\shortparallel}; 0, z) \big], \tag{14.7}$$

where no summation is applied on the underlined index. Making the Fourier transform along x and y and taking the divergence of the above equation and then substituting into Equation (7.6), we obtain the chemical potential in a hybrid $(\mathbf{q}, z)$ space as:

$$\mu_1^s(\mathbf{q}) = q_\alpha (c_{11} + 2c_{12})\varepsilon^* \sigma \int dz'\, \vartheta(\mathbf{q}, z') \big[q_\beta G_{\alpha\beta}(\mathbf{q}; 0, z') + \mathbf{i} G_{\alpha\underline{z},\underline{z}}(\mathbf{q}; 0, z') \big], \tag{14.8}$$

where $\mathbf{i} = \sqrt{-1}$.

We can also develop the chemical potential for crystals with cubic symmetry. It is easy to show that the equation for cubic crystals is exactly the same as Equation (14.8), except that we have to use the Green's function for half-space material with cubic symmetry.

It is noted that by using Equation (14.8) we reduce the computation of the chemical potential $\mu_{s0}(\mathbf{q})$ in the Fourier spacean inclusion with an arbitrary shape to an integral in one dimension. Thus, it has a significant efficiency in the Fouier-Garlerkin approach in the kinetic model. In the future steps, the coverage-independent term calculated by Equation (14.8) can be substituted in the governing equation (10.7) and the same numerical calculation can be taken as described in Section 10.

14.2 An External Electromagnetic Field

In the case of interfacial dislocations and the inclusion/void lattice situation, the external field interferes with the self-organization of adatoms via the substrate elastic deformation. Additionaly the long-range interactions between adatoms are also mediated by the substrate. The mechanisms of forming self-organized nanostrcutures by a laser field are more complicated than the previous substrate-mediated elastic field, since the electronic properties of atoms have to be taken into account. A well-known explanation is based on the evaluation of the interaction between the external laser field and adatoms. This interaction is induced by two types of forces: a spontaneous force and a dipole force. The spontaneous force comes from the repeated adsorption and re-radiation of one photon by an atom. It plays the major role, especially during cooling (collimation) of atoms by the laser field. The dipole force arises when the atom has an oscillating dipole

driven by the laser field. The corresponding force is proportional to the intensity gradient in a variable electromagnetic field. This concept was first proposed by Ashkin [3]. If the laser beam is tightly focused, a neutral atom of polarizability α can be "trapped" at the focus of a laser beam, which is called a *laser tweezer*. The potential associated with the dipole force can be written simply as [45]

$$U(\mathbf{r}) = \frac{\hbar\Delta}{2} \ln\left(1 + \frac{I(\mathbf{r})}{I_0} \frac{\Gamma^2}{\Gamma^2 + 4\Delta^2}\right), \tag{14.9}$$

where $\hbar$ is Planck's constant divided by 2π, Δ is the de-tuning of the laser from atomic resonance frequency, I is the laser intensity, I_0 is the atomic saturation intensity, and Γ is the natural atomic resonance line width. The dipole force ($\mathbf{F}$) experienced by the atom is given by

$$\mathbf{F}(\mathbf{r}) = -\nabla U(\mathbf{r}). \tag{14.10}$$

Thus by calculating the trajectories of deposited atoms falling over about 0.3 mm, a distribution of atoms can be obtained consistent with experimental results.

Although the established field-atom-interaction mechanism works very well in analyzing the dot formation of Chromium atoms and some other types of atoms (especially group III atoms: Al, Ge and In [60]), there is an interesting experimental result on helium atoms performed by Petra et al. [57]. In Figure 14.12 a comparison is made between simulated and experimental results.

Although the intensity profiles for linearized and circular polarized light are not significantly different[†], it is clear that the experiments on helium atoms with

[†]If the two standing waves are superimposed in the x and y directions, the intensity profile is proportional to $\left[\sin(x)+\sin(y)\right]^2$ in the case of linear polarized lights, and $\sin^2(x)+\sin^2(y)+\left[\sin(x)+\sin(y)\right]^2$ in the circular polarization case.

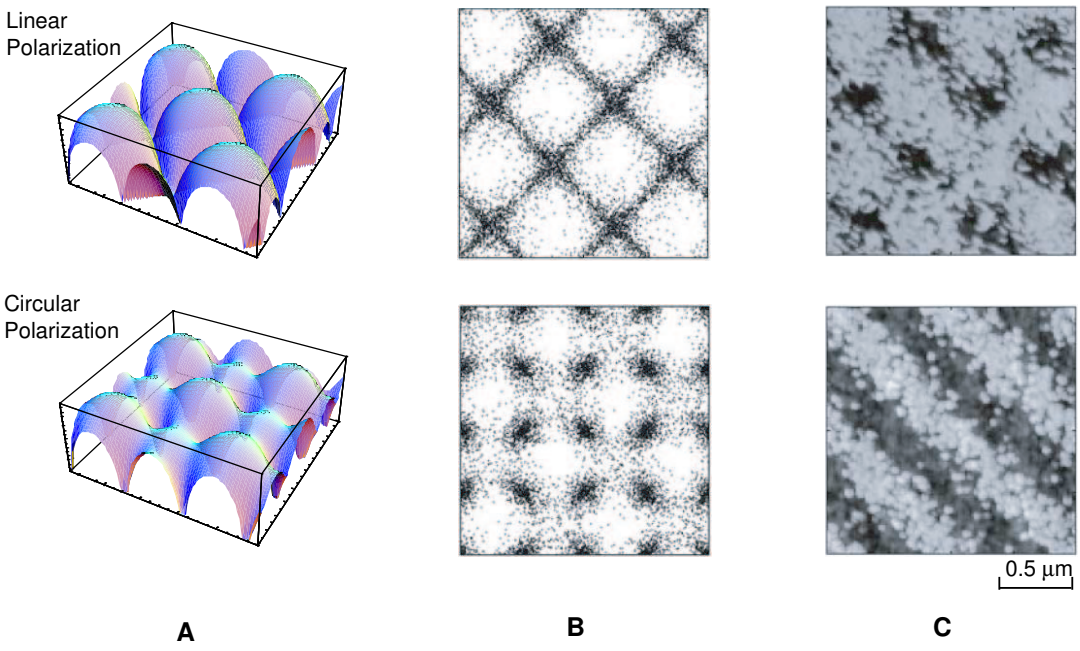

Figure 14.12: Comparison of calculated results by the trajectory method, experimental results for a linearized light field (upper row) and circular light field (lower row). (A) Calculation of the laser potential profile. (B) the calculated atomic distributions and (C) the experimental results [57].

circular polarization are not in agreement with the trajectory model. Furthermore, the structures with distinct strip patterns in circular fields seem to indicate some links to our mesoscopic models.

In fact, the trajectory model simplifies the problem by two important assumptions in the simulation. First, there is neither short-range nor long-range interaction between deposited atoms. The other assumption is that atoms after deposition on the substrate will not diffuse. These two assumptions are valid in the experiments of McClelland [46], where chromium is a self-passivating metallic material, and after deposition Cr atoms are soon passivated by the surface so that they have a very low surface mobility, even at a high temperature of 1500 °C. Thus the trapping effect of laser on Cr atoms dominates the atomic distribution on the substrate during the deposition process. On the other hand, helium atoms are not passivated on the surface and they have a large surface diffusion coefficient so that our model, which includes both field-atoms and atom-atom interactions and the diffusion activity provides a possible way to reveal the mechanisms in Petra's experiment. Especially nowadays many new technologies have been developed to fabricate nanosized structures by depositing charged atoms or macro-particles on the liquid or on "smooth" inert surfaces. Our model is expected to have a wider application in the future.

Following a the similar treatment to that of Chapter III, it is easy to see that in considering two-body interactions only (i.e. no cluster effect), the nearest-neighbor interaction term remains the same as before and the free energy of the field-atom interaction is proportional to the coverage. The chemical potential μ_{s0} is given by

$$\mu_{s0}(\mathbf{r}) = U(\mathbf{r})a^2, \tag{14.11}$$

where $U(\mathbf{r})$ is the potential energy according to Equation 14.9 and a is the lattice constant.

However, the long-range interaction term should have a different consideration since the kernel in the global integration is related to the intensity of the laser field and is thus non-uniform. The potential energy by long-range interactions can be written as:

$$\mathcal{F}_{\mathrm{LR}} = \frac{1}{2}\sum_{i,j} W_{ij} c_i c_j \rightarrow \frac{1}{2}\iint W_{LR}(\mathbf{r},\mathbf{r}')c(\mathbf{r})c(\mathbf{r}')\,d\mathbf{r}\,d\mathbf{r}' \tag{14.12}$$

where the bold typeface denotes a vector. W_{LR} is generally a function of the vectors $\mathbf{r}$ and $\mathbf{r}'$ and the unit is energy per atom. In most cases, the function is proportional to the field intensity (I) at $\mathbf{r}$ and $\mathbf{r}'$, and the type of long-range interaction (Φ). It can be written as a form with separate variables:

$$W_{\mathrm{LR}}(\mathbf{r},\mathbf{r}') = K_d I(\mathbf{r})\Phi(\mathbf{r}-\mathbf{r}')I(\mathbf{r}'). \tag{14.13}$$

Making use of Fourier representations:

$$\begin{aligned} I(\mathbf{r})c(\mathbf{r}) &= \int \frac{d^3q}{(2\pi)^3}\{I\cdot c\}_{\mathbf{q}}\, e^{i\mathbf{q}\cdot\mathbf{r}} \\ \Phi(\mathbf{r}-\mathbf{r}') &= \int \frac{d^3q}{(2\pi)^3}\Phi_{\mathbf{q}}\, e^{i\mathbf{q}\cdot(\mathbf{r}-\mathbf{r}')}, \end{aligned} \tag{14.14}$$

and with the application of the relation:

$$\int e^{i(\mathbf{q}+\mathbf{q}')\cdot\mathbf{r}}\,d\mathbf{r} = (2\pi)^3\delta(\mathbf{q}+\mathbf{q}'), \tag{14.15}$$

in Equation (14.12), we obtain:

$$\mathscr{F}_{\mathrm{LR}} = \frac{K_d}{2} \int \frac{d^3q}{(2\pi)^3} \Phi_{\mathbf{q}} \Big| \{I \cdot c\}_{\mathbf{q}} \Big|^2. \tag{14.16}$$

The variational derivative of Equation (14.12) yields:

$$\begin{aligned} \left\{ \frac{\delta \mathscr{F}_{\mathrm{LR}}}{\delta c} \right\}_{\mathbf{r}} &= K_d \int \frac{d^3q}{(2\pi)^3} I(\mathbf{r}) e^{-i\mathbf{q}\cdot\mathbf{r}} \, \Phi_{\mathbf{q}} \, \{I \cdot c\}_{\mathbf{q}} \\ &= K_d \int \frac{d^3q}{(2\pi)^3} I(\mathbf{r}) e^{-i\mathbf{q}\cdot\mathbf{r}} \, \Phi_{\mathbf{q}} \int d^3r' I(\mathbf{r}') c(\mathbf{r}') e^{-i\mathbf{q}\cdot\mathbf{r}'}. \end{aligned} \tag{14.17}$$

In the Fourier space, we have:

$$\begin{aligned} \left\{ \frac{\delta \mathscr{F}_{\mathrm{LR}}}{\delta c} \right\}_{\mathbf{q}} &= \int d^3r \left\{ \frac{\delta \mathscr{F}_{\mathrm{LR}}}{\delta c} \right\}_{\mathbf{r}} e^{-i\mathbf{q}\cdot\mathbf{r}} \\ &= K_d \int \frac{d^3q'}{(2\pi)^3} \left[\int d^3r I(\mathbf{r}) e^{-i(\mathbf{q}+\mathbf{q}')\cdot\mathbf{r}} \right] \Phi_{\mathbf{q}'} \{I \cdot c\}_{\mathbf{q}'} \end{aligned} \tag{14.18}$$

Thus, the Fourier component of the variational derivative of the long-range potential energy is generally coupled with the full spectra in the wave vector space, which offers great difficulties in both analytic and numerical methods. However, we can easily find that if $I(\mathbf{r})$ is taken out of the integral in the first bracket, with Equation (14.15), Equation (14.18) can be greatly simplified. An obvious example is $I(\mathbf{r}) = \text{const.}$, which corresponds to all cases where long-range interactions are not induced by the external fields but by their own properties, such as Coulomb interactions between equal-charged particles and dipolar interactions in magnetic spin systems. Besides the constancy of $I(\mathbf{r})$, there is another situation which can simplify the problem. Let us denote the characteristic length of the external fields as l, the effective length of long-range interactions as r_l and the wavelength of the pattern (related to c) as λ. If $l > \lambda \gg r_l$, this means that over the length scale of r_l, long-range interactions have a significant change, while

the field can be approximately considered to be locally constant. Thus, we can rewrite the long-range potential energy in real space as:

$$\mathcal{F}_{\mathrm{LR}} \approx \frac{K_d}{2} \iint d\mathbf{r}\, d\mathbf{r}'\, \Phi(\mathbf{r}-\mathbf{r}') I(\mathbf{r}')^2 c(\mathbf{r}) c(\mathbf{r}'). \tag{14.19}$$

The variational derivatives in real and Fourier space become:

$$\begin{aligned}
\left\{\frac{\delta \mathscr{F}_{\mathrm{LR}}}{\delta c}\right\}_{\mathbf{r}} &= \frac{K_d}{2} \int d\mathbf{r}\, \Phi(\mathbf{r}-\mathbf{r}') I(\mathbf{r}')^2 c(\mathbf{r}') + \frac{K_d}{2} I(\mathbf{r})^2 \int d\mathbf{r}\, \Phi(\mathbf{r}-\mathbf{r}') c(\mathbf{r}') \\
&\approx K_d \int d\mathbf{r}\, \Phi(\mathbf{r}-\mathbf{r}') I(\mathbf{r}')^2 c(\mathbf{r}') \qquad (14.20) \\
\left\{\frac{\delta \mathscr{F}_{\mathrm{LR}}}{\delta c}\right\}_{\mathbf{q}} &= K_d \Phi_{\mathbf{q}} \{I^2 c\}_{\mathbf{q}}. \qquad (14.21)
\end{aligned}$$

Here we just give an intuitive picture about length scales. From Walgraef's work [79], where only nearest neighbor interactions are considered, the effective interaction length is of the order of the lattice constant (a), and the characteristic wavelength of the patterns is of the order of $100a$ (λ_{nn}). Practically, the cutoff distance of long-range interactions between particles is of the order of $10a$ (r_l). Let's assume the scales are linear, the patterns generated by long-range interactions will be possibly on the order of $1000a$ (λ_l). If the wavelength of the external field is in the micro scale, it meets the condition

$$l > \lambda_l \gg r_l > a.$$

The term of $\{I^2 c\}_{\mathbf{q}}$ in Equation (14.21) exhibits the advantages of the model. If long-range interactions are comparable to or greater than nearest neighbor interactions, the wavelength of the patterns of the system will appear with a large scale, which represents realistic results corresponding to the experiments.

The remaining task is to consider both external field term (Equation 14.11) and the long-range interaction term (Equation 14.21 with a proper interaction

potential $\phi^{\ddagger}$) in Fourier space into the kinetic equation (10.7). The similar numerical calculation can be taken as described in Section 10.

‡If the deposited atoms are neutral, $\phi(\mathbf{r}-\mathbf{r}')$) has a dipole form [51]. If the atoms are charged, ϕ is a Coulomb type interaction and $\sim r^{-1}$, then in Fourier space, $\phi_{\mathbf{q}}$ has a form of q^{-2}.

CHAPTER VI

Atomistic Modelling of the Early Clustering Stages

15 Single Atom Diffusion

In the previous chapters, a phase field model has shown that the spontaneous ordering of atomic clusters can be changed by a fairly weak external elastic field. As pointed out in Section 4.2, this approach is a continuum description. However, at very low coverage, the validity of the continuum description becomes questionable. Moreover, inclusion of entropy contributions becomes less accurate for very small coverage because of its logarithmic divergence. Clustering of surface atoms during the early stages of deposition is more appropriately described as a nucleation process at the atomic level. For these reasons, we devote this chapter to modelling the early stage of surface cluster nucleation. The atomistic model that will be described here combines empirical interatomic potential determination of energetics with the Kinetic Monte Carlo (KMC) approach.

It is known that during physical adsorption, an adatom deposited on the substrate performs thermally activated hopping between possible lattice sites. The hopping activity is statistically determined by the energy barrier. In a system with identical but distinguishable particles, Maxwell-Boltzmann statistics govern the process, which means that the probability per unit time for a possible adatom

jump, i, to take place is given by

$$p_i = \nu_0 \exp\Big(-\frac{E_i}{k_{\mathrm{B}}T}\Big), \tag{15.1}$$

where ν_0 is a constant, and for the current problem it can simply be taken as the Debye frequency $10^{13}\,\mathrm{s}^{-1}$. k_{B} is the Boltzmann constant and T is the absolute temperature. E_i denotes the total energy barrier, which depends on the surface properties, stress fields and neighboring adatoms, that is

$$E_i = \Delta E_i^{\mathrm{S}} + E_i^{\mathrm{m}} + \Delta E_i^{\mathrm{A}}, \tag{15.2}$$

in which ΔE_i^{S} is the difference of binding energies of two lattice sites. E_i^{m} is the migration energy barrier and ΔE_i^{A} is the activation energy change by the stress field.

The material system considered in the current study is the SiGe semiconductor. It is known that there is always a reconstruction structure on the Si(001) surface, which involves the formation of Si dimers [50]. The bond length is approximately 2.31 Å [39]. Normally the dimers might appear buckled which means one of the two dimer atoms should be upper and the other is lower [77]. Since the buckling is very small (the angle of the tilted bond is about 15°), it is reasonable to ignore this detailed structure. Figure 15.1 illustrates a top view of the reconstructed Si(001) surface. Here, an atomic surface model is adopted similar to the reference [69]. The possible diffusion pathways of adatoms on the surface are indicated by the dash lines. There are $P1(MFHCHFM)$ and $P2(MBQBM)$ and $P3(MAPDQBM)$. In the absence of a external field, the potential energies along the corresponding diffusion pathways at the M site are based on the results of first principles calculations [69].

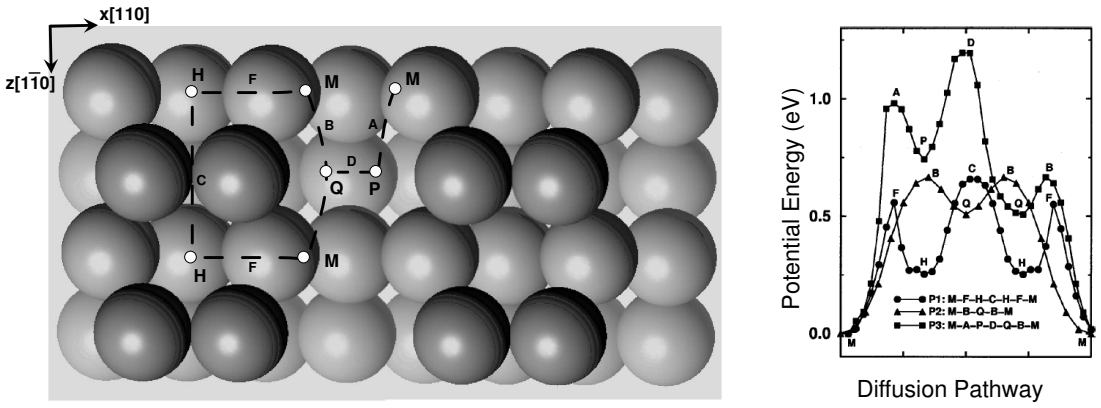

Figure 15.1: Schematic top view of the Si (001)-2×1 reconstructed surface (left) and first principles calculations of the potential energies (refereed to the adsorption energy) at the M site along two diffusion pathways (right) [69].

Due to changes in lattice distances by the elastic strain, the potential energy of surface atoms is changed, and adsorbed atoms would have a different diffusion energy barrier. It is indeed shown by many investigations that there is an effect of the elastic strain field on atomic diffusion. For example, Schroeder used a classical Lennard-Jones (LJ) pair potential model to calculate the energy profiles of the FCC, BCC and Simple Cubic (SC) crystalline surfaces and found that the strain field changes the saddle point energy much more than the binding energies [62]. He also found that tensile strain increases the barrier and compressive strain decreases the barrier. The magnitude of these changes is about 0.15 eV per 1% strain. A more complicated case is considered by Hoshino [26] via *ab inito* calculations for the migration of Si adatoms on a strained Si(111) surface. The inhomogeneity of the Si surface induced by the adatom makes the two different activation energies (negative of the energy barrier) change, with a maximum of 0.05 eV per 1% strain. Based on first principles calculations, Shu summarized the change in the surface diffusion barrier by a strain fields as a linear relation [69]:

Pathways	P1	P2	P3
E_i^0 (eV)	0.65	0.66	1.19
$A\Delta\sigma_{xx}$ (eV)	0.94	2.43	3.32
$A\Delta\sigma_{yy}$ (eV)	-6.23	-0.15	-6.60

Table 15.1: The strain-free diffusion barriers and the activation strain tensor along the three diffusion pathways on a Si(001) surface by first principles calculation [69].

$$\begin{aligned} E_i &= E_i^0 + A\big[(\sigma_{xx}^{\rm sad} - \sigma_{xx}^{\rm min})\epsilon_{xx}^{\rm min} + (\sigma_{yy}^{\rm sad} - \sigma_{yy}^{\rm min})\epsilon_{yy}^{\rm min}\big] \\ &= E_i^0 + A\Delta\boldsymbol{\sigma}\boldsymbol{\epsilon}^{\rm ext}, \end{aligned} \tag{15.3}$$

where A is the surface area. $\boldsymbol{\sigma}$ denotes the intrinsic surface-stress tensor as before. But here, $\boldsymbol{\sigma}$ is the true value induced by ad-particles at the saddle and minimum points denoted by the superscripts respectively. The numerical value of $A\Delta\boldsymbol{\sigma}$ is given in Table 15.1. It can be noticed that a compressive (or tensile) strain may either increase or decrease the diffusion barrier as seen by negative signs of $A\Delta\sigma_{yy}$.

Unfortunately, although Shu claimed in his paper that the effect of strain on diffusion (about 0.1 eV per 2% strain) is quantitatively significant, in practice the applied external field which exhibits a significant effect on self-organization is much less than 0.1% strain. For example, the strain field of buried interfacial dislocations can be estimated as $\nu b/h$, where ν is Poission's ratio, b is Burger's vector and h is the thickness of the substrate layer on the surface. In the experiments on Ge self-assembled quantum dots on partially relaxed SiGe buffer layers [32, 34], the thickness is about 80nm and the length of the Burger's vector is about 0.2nm. Thus, the strain magnitude is only on the order of 0.1%. Thus, the

diffusion energy barrier changes only by 0.01 eV or less. This value is obviously much smaller than the strain-free diffusion barriers. These quantitative aspects will now be quantified by Kinetic Monte Carlo (KMC) simulations.

KMC methods are based on the assumption of ergodicity, which asserts that all possible states in a stochastic system will be experienced by a nonzero positive probability without the dependence of any initial conditions. This assumption allows us to sample out the time domain from a statistical distribution of the system. Specifically for a discrete lattice structure, the KMC procedure practically means a full list of all possible events (atomic hopping) of the whole systems (all adatoms). Each event is denoted by a random number from 0 to 1, and that is equaled to the corresponding probability per unit time. The selection of a event (e.g. one adatom makes a jump) is controlled by a random number in the range $(0, 1)$. The reciprocal of the atomic jump probability per unit time is a residence time for an atom that moves by that specific type of jump. Since jump probabilities of all different types of jumps are independent, the overall probability per unit time for the system to change its state by any type of jump step is just the sum of all possible specific jump probabilities. Therefore, the residence time for the system in a specific configuration is the reciprocal of this overall jump probability. Whenever a jump is to be made, the specific one is determined by a random choice based on the relative probabilities of all potential jumps. Hence, the time increment step for one jump is:

$$\Delta t_{jump} = -\ln(\eta) \left(\sum_{i=1}^{N} p_i \right)^{-1}, \tag{15.4}$$

where, η is a random number uniformly distributed in the range $(0, 1)$, N is the total number of deposited adatoms.

Thus, from Equations (15.1) and (15.4), the time (Δt_{jump}) that a jump to be

biased by the energy barrier's change of the 0.01 eV from the external field can be estimated as

$$\frac{\Delta t_{jump}}{t_{jump}} \sim \frac{e^{-\Delta E/k_{\mathrm{B}}T}}{e^{-E/k_{\mathrm{B}}T}} \sim 10^{10}, \tag{15.5}$$

which is unrealistically long. Therefore the effect of the external strain field on single adatoms will not influence the organization of the atomic clusters during the early clustering stages.

16 Island Diffusion

A possible reason that single atom diffusion is not able to explain quantum dot self-assembly that is observed experimentally is that the model for single atoms does not account for interactions between atoms, including both two-body and many-body ones. Physically, when adatoms jump close enough to one another, they will form clusters. As the size of a cluster becomes large enough, a new surface (actually a new phase) is formed. Thus the effects of external elastic fields on clusters will be much larger than its effects linearly summed on the individual atoms. This mechanism is consistent with the continuum treatment mentioned in previous chapters. However the explicit form of the nonlinear dependence has to be determined by an atomistic approach.

There are several mechanisms for explaining the diffusion of an atom cluster, including the random motion of periphery atoms, vacancy migration across the cluster, evaporation and condensation of atoms in the island and dislocation motion in the island, all of which can induce the shift of the mass center of an island [44]. In our case, since small-size quantum dots are defect-free, we will focus on the motion around the periphery and the evaporation/condensation

processes. During the simulation of island diffusion, a simplification is made in which the reconstructed dimer structure of the surface is ignored and only the regular crystal structure is considered. The validity of this assumption is due to the existence of surface steps. It is known that the orientations of different surface steps are totally randomly distributed, and that the normal size of each step is much smaller than the average diffusion length of atom clusters. Thus the random distribution of surface steps dominates any local diffusion anisotropy due to the dimer surface reconstruction. The thermodynamic investigations of Metiu [48] indicate that the equilibrium shape of an island is roughly square. We assume here that the island will re-arrange all its atoms automatically by a spiral way. The basic idea to solve the island diffusion problem here is to deal with the whole atom cluster as one entity. For simplicity, every motion of an island is assumed to be a jump of the island's mass center from one regular lattice site to a nearest neighbor. Hence, this motion should be looked at a final result of many periphery atoms' edge diffusion.

To consider the bias effect of an applied strain field on cluster diffusion, a simple idea similar to that proposed by Mattson et al. [42] is adopted. We consider the island to be fixed on surface and calculate the binding energy as a function of island size. Here, we will use the Modified Embedded Atom Method (MEAM) for Si surface is. In this approach, a semi-empirical formula for the total energy is expressed as:

$$E = \sum_i \sum_{j \neq i} \frac{1}{2} \phi \left(r_{ij} \right) + \sum_i F \left(\rho_i \right), \tag{16.1}$$

where ρ_i is the electron density at the position of atom i, and is a function of the positions of all atoms in the system. ϕ is the pair potential and F is the embedding energy function, both of which are given by Baskes [7] as:

$$F(\rho_i) = A_E E_c \left(\frac{\rho_i}{\rho_X(r_e)}\right) \ln\left(\frac{\rho_i}{\rho_X(r_e)}\right) \tag{16.2}$$

$$\phi(R_i) = -2\frac{E_c}{Z}\left[\left[1+\eta+0.05\eta^3\right]e^{-\eta} + A_E\left(\frac{\rho_X(R_i)}{\rho_X(r_e)}\right)\ln\left(\frac{\rho_X(R_i)}{\rho_X(r_e)}\right)\right], \tag{16.3}$$

where A_E, E_c and $\rho_X(r_e)$ are material constants, $R_i = \left(\widetilde{1}+\widetilde{\varepsilon}_i\right) r_i - r_{ad}^{SP}$,

$$\rho_i = \frac{2\rho_i^{(0)}}{1+\exp\left[-\sum_{l=1}^{3} t^{(l)}\left(\rho_i^{(l)}\Big/\rho_i^{(0)}\right)^2\right]} \tag{16.4}$$

$$\left(\rho_i^{(l)}\right)^2 = \sum_{j\neq i}\sum_{k\neq i} f^{(l)}(r_{ij})\, f^{(l)}(r_{ik})\, L^{(l)}(\cos\theta_{jik}) \tag{16.5}$$

$$f^{(l)}(r_{ij}) = f_e e^{-\beta^{(l)}(r_{ij}/r_e-1)}. \tag{16.6}$$

$L^{(l)}, l = 0 \sim 3$ are the unnormalized Legendre polynomials.

$$\eta = \alpha\left(\frac{R}{r_e}-1\right), \qquad \alpha = \sqrt{\frac{9\Omega_e B}{E_c}}, \tag{16.7}$$

with Ω_e the equilibrium atomic volume and B the bulk modulus.

The parameters for the MEAM of Si [6] and Ge [7] are listed in Table 16.2 and the geometric factors in MEAM are listed in Table 16.3 [27]:

The excess island binding energy is shown in Figure 16.2. The result shows that a semiconductor island has a remarkably different behavior from a metal island. We fit the results for the island binding energy with a 3^{rd} order polynomial function,

$$E_{bc}^{(i)}(N,\varepsilon) \approx \left(0.0174N^3 - 0.675N^2 + 29.55N - 72.56\right)\cdot\left[\varepsilon_x(x,y) + \varepsilon_z(x,y)\right], \tag{16.8}$$

	Si	Ge		Si	Ge
$t^{(1)}$	2.05	4.02	$\beta^{(0)}$	4.4	4.55
$t^{(2)}$	4.47	5.23	$\beta^{(1)}$	5.5	5.5
$t^{(3)}$	-1.8	-1.6	$\beta^{(2)}$	5.5	5.5
f_e	0.1705	0.1705	$\beta^{(3)}$	5.5	5.5
r_e(Å)	2.350	2.450	E_c(eV)	4.63	3.85
A_E	1.00	1.00	α	4.893	4.98

Table 16.2: Parameters in MEAM of Si and Ge

$S^{(0)}$	$S^{(1)}$	$S^{(2)}$	$S^{(3)}$	Z_0	C_{max}	C_{min}
1	0	0	32/9	4	2.8	2.0

Table 16.3: Geometric factors in MEAM

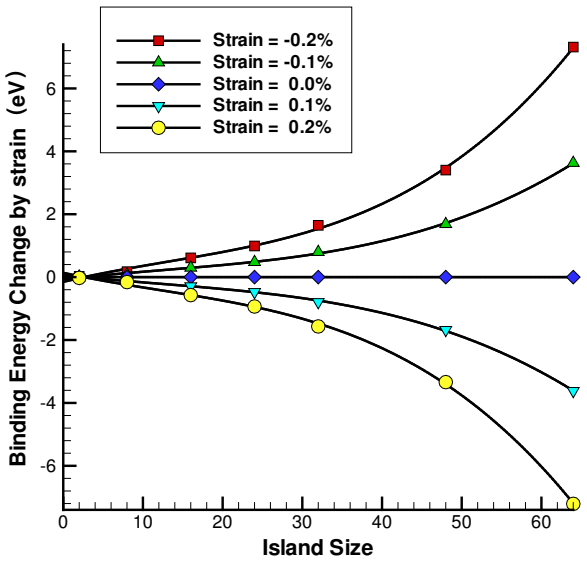

Figure 16.2: Binding energy change of an island as a function of size

where $E_{bc}^{(i)}$ is the change of binding energy of an island with size N. The superscript (i) means that the center of mass of the island is at the lattice site i with the position of (x, y). Following by the same method of single atom diffusion, the activation energy barrier of an island on a strained surface can be written as:

$$E_a^{(i)} = E_{a0}^{(i)}(N) + E_{bc}^{(i)}(N, \varepsilon(\overline{x}, \overline{y})) - E_{bc}^{(i)}(N, \varepsilon(x, y)), \tag{16.9}$$

where $E_{a0}^{(i)}$ is the activation energy of the island without a strain field. The dependence of the activation energy on the island size and temperature has been determined by Mills *et al.* [49]. It can be found that the activation energy changes very small for different island sizes (from $N = 250$ to 2000). Thus, we assume here that the semiconductor surface has a constant value: $E_{a0}^{(i)} \approx 0.79\,\mathrm{eV}$.

The "random cluster scaling theory" (RCST) gives the island diffusion coefficient as [68]:

$$D^{(i)} \sim N^{-3/2} e^{-E_a^{(i)}/k_B T}, \tag{16.10}$$

where $D^{(i)}$ is the diffusion coefficient of island diffusion. If we assume that islands perform uncorrelated random walk, then

$$D^{(i)} \propto \langle \nu_h \rangle \left\langle \delta d_{c.m.}^2 \right\rangle, \tag{16.11}$$

where $\langle \nu_h \rangle$ is the jump rate for island diffusion; $\langle \delta d_{c.m.}^2 \rangle$ is the mean-square displacement of the island mass center per jump event. Since in our accelerated model, every jump distance is assumed to be fixed no matter what size the island is, this means:

$$\left\langle \delta d_{c.m.}^2 \right\rangle = const. \tag{16.12}$$

Obviously, we have:

$$\langle \nu_h \rangle = \nu_0 N^{-3/2} e^{-E_a^{(i)} \big/ k_B T}. \tag{16.13}$$

We choose the rate constant as: $\nu_0 = 10^{13}\,\mathrm{s}^{-1}$. The evaporation process in an island can be simulated by the chemical kinetics analysis, as discussed in details by Shao *et al.* [63], Mattsson *et al.* [43]. Based on the fact that the evaporation is a first-order rate process, we adopt the following relation:

$$p\,(t)\,dt = k_e dt \exp\left[-k_e t\right]. \tag{16.14}$$

Here $p(t)dt$ is the probability that an island with size N will emit one atom between t and $t + dt$ by setting the time of the last emission action to zero. k_e is the evaporation rate constant and is dependent on size N and temperature T, and is of the form [63, 43]:

$$k_e = A \exp\left[-E_e/k_B T\right] N^{1/2} \exp\left[B \big/ N^{1/2}\right], \tag{16.15}$$

where A, B and E_e are constants. For $T < 650\,\mathrm{K}$, $A = 0.063$, $B = 4.07$; for $650\,\mathrm{K} < T < 950\,\mathrm{K}$, $A = 0.051$, $B = 4.87$; and for $T > 950\,\mathrm{K}$, $A = 0.086$, $B = 4.55$ [63].

17 KMC Simulation Results

Our simulation follows the standard kinetic Monte Carlo method and is performed on a $350 \times 350\,\mathrm{nm}^2$ surface area. Two infinitely long straight dislocation lines are assumed to be buried 80nm underneath the surface at $x = 250\,\mathrm{nm}$ and $z = 250\,\mathrm{nm}$, respectively. Figure 17.3 shows the evolution diffusion process for 500

atoms on the top of the surface at a temperature of 650°C. The background contours represent the strain field imposed by the interfacial dislocation network. The white dots denote atoms. The clusters of adatoms which contain more than 6 atoms are shown by block arrows pointing to the nearest spot.

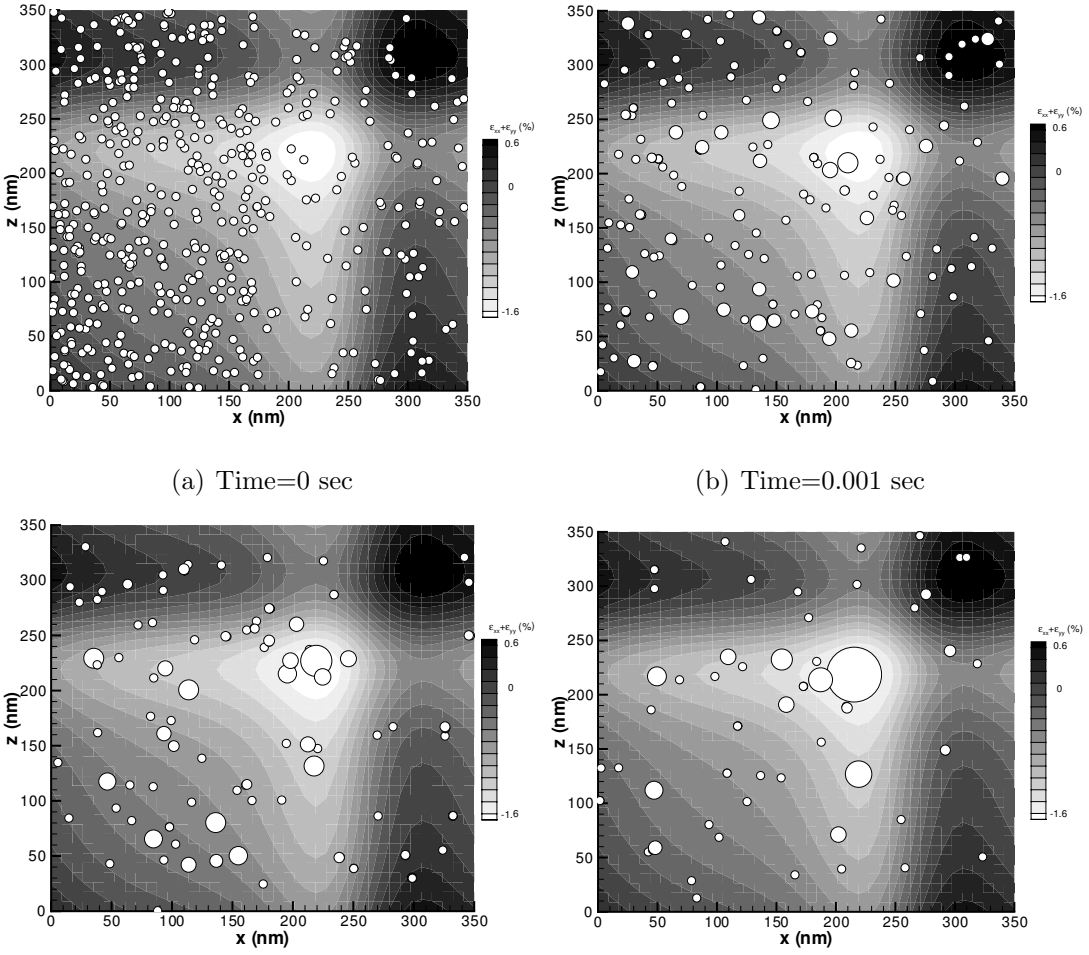

(a) Time=0 sec

(b) Time=0.001 sec

(c) Time=0.006 sec

(d) Time=0.033 sec

Figure 17.3: KMC simulation for 500 Ge atoms on (001) Si surface at 650°C. The small white dots denote single atoms. The larger (scale to island sizes) white dots denote the atomic clusters.

It is clear that by introducing island diffusion, Ge atom clusters tend to mi-

grate toward the maximum compression area on the Si surface, even though the external strain field variation is very small. Because of thermal emission, a population of single atoms coexists with islands, as can be seen in Figure 17.3.

Figure 17.4 compares the average mean square displacement for the atom-diffusion-only model and atom/cluster-diffusion model. The atom/cluster coupled diffusion model shows a larger diffusion length and much lower island density, which indicate that self-organization of islands is taking place during the diffusion. This can also explain why quantum dots nucleate at locations which have a larger distance than the average diffusion length of single atoms [32, 34].

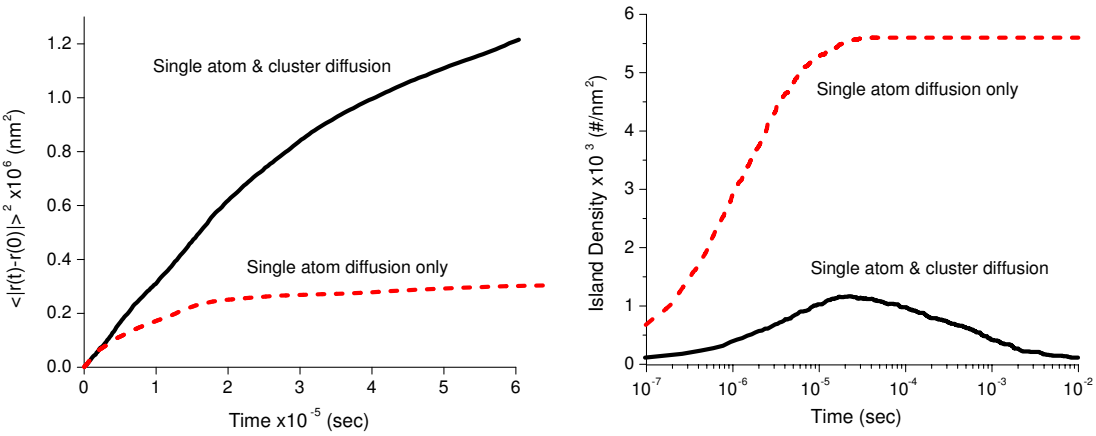

Figure 17.4: A comparison of the average mean square displacement (left) and the island density (right) under dislocation strain field for the atom-diffusion-only model and the atom/cluster-diffusion model

From the present simulations, we conclude that island diffusion plays a significant role in the self-organization of surface atomic clusters during the early stages of evolution. The results also indicate that in semiconductor systems, self-organization effect tends to be stronger than in metallic systems. Figure 17.5 confirms this conclusion.

The influence of temperature on atom and island diffusion is shown in Fig-

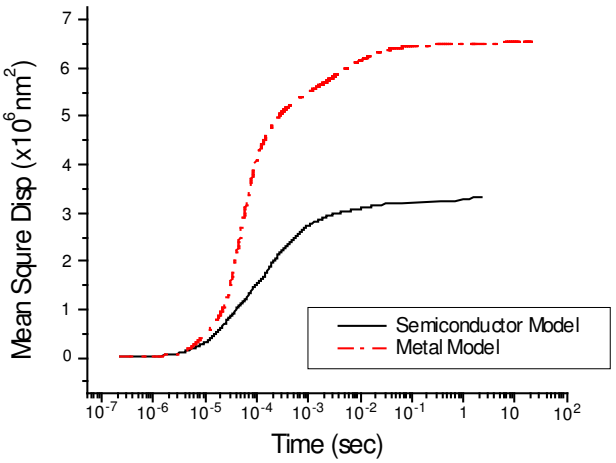

Figure 17.5: Comparison of the average mean square displacement of atom/cluster-diffusion model for semiconductors and metal systems.

ures 17.7, 17.8 and 17.9. In Figure 17.6, we define a total vector distance as

$$R_{tot} = \left| \sum_{i=1}^{n} \mathbf{R}_i \right| \Big/ \; n,$$

where $\mathbf{R}_i$ denotes the position vector of the i^{th} atom and n is the total number of atoms on the surface square†. If the maximum compressive position is defined as R_0, which is the expected equilibrium spot, Figure 17.7 shows the ratio of the total vector distance to the equilibrium spot as a function of time at three different substrate temperatures. It is concluded that equilibrium takes place very quickly at higher temperatures. The figure also reveals that atom emission from islands provides only a fluctuation effect, and has no remarkable influence on the diffusion process. Thus, ignoring the evaporation effect is a reasonable approximation similar to the conclusions of Bogicevic *et al.* [9].

†Note that the square has periodic boundary conditions and the total number of atoms in it is conserved.

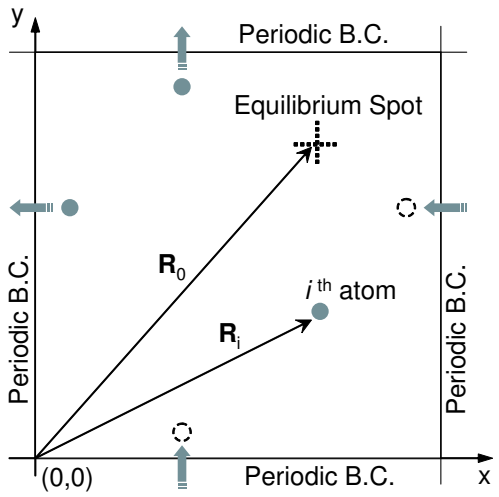

Figure 17.6: The Definition of vector distance of an atom.

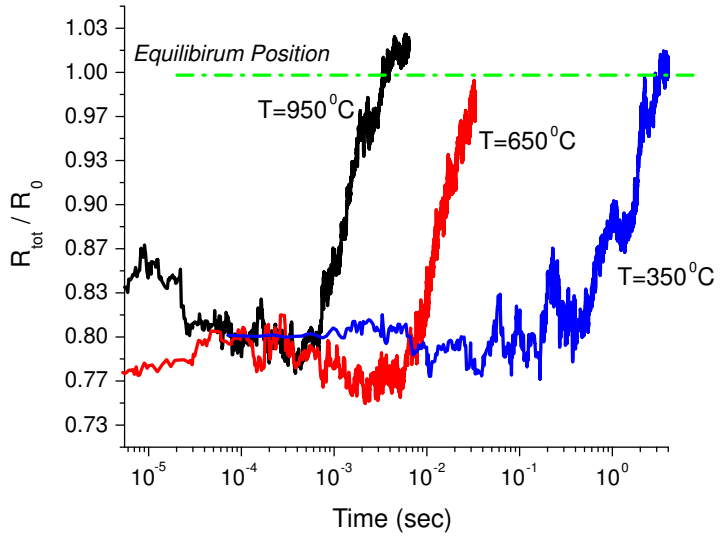

Figure 17.7: A comparison of the total vector distance as a function of time at three different temperatures

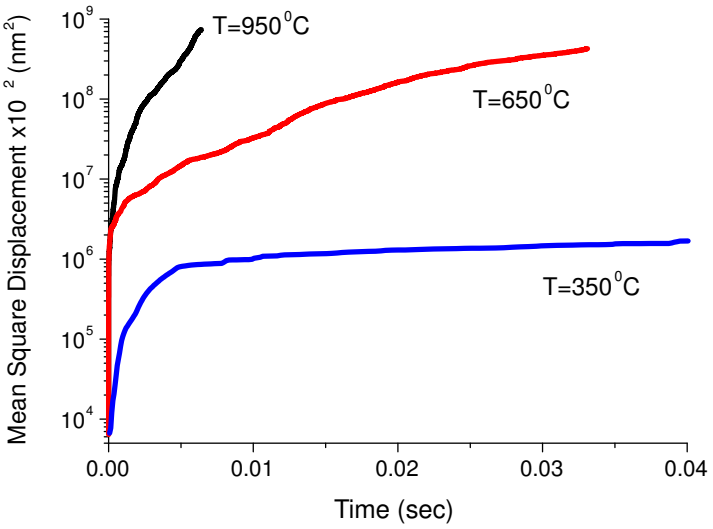

Figure 17.8: A comparison of the average mean square displacement for all atoms as a function of time at three different temperatures

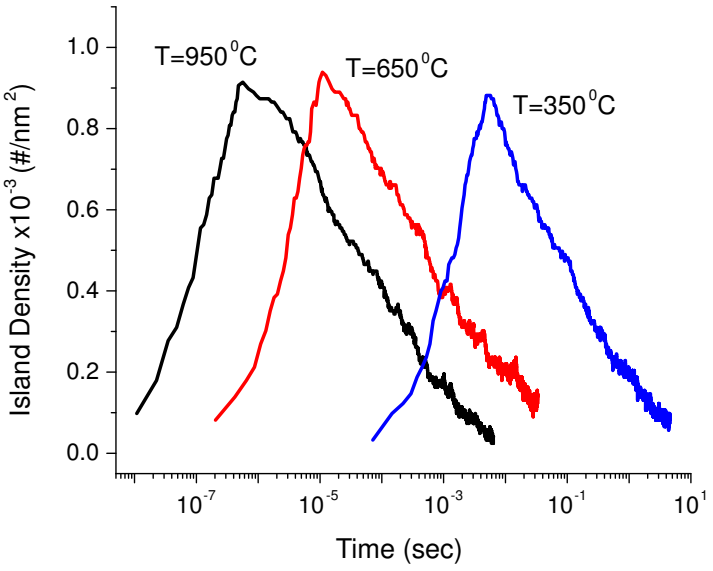

Figure 17.9: The comparison of Ge island density at three different temperatures

CHAPTER VII

Conclusions

THERE are in summary three main parts which constitute the present thesis. The first part is a *review* (Chapter II), in which we present a self-consistent survey of various experimental observations on intrinsic and directed self-organization of surface atomic clusters (Section 3). We also explore the role of external fields through existing experimental evidence. We then summarize the theoretical models on surface clustering and self-organizations during thin film growth (Section 4) and the interpretation of the "multi-scale" modelling concept. Based on this extensive review, a continuum description of a phase field model for the coverage, c, is selected for further development in the model of which the second part of the current thesis.

The second part (Chapters II to V) is concerned with *continuum modelling* and is the major bulk of the thesis, in which we set up a phase field model to describe monolayer cluster evolution on the surface. We include in this model with the effects of interactions mediated by the substrate, expressing these interactions via the gradient of the intrinsic surface stresses. The direct interaction between clusters and applied non-uniform strain fields is included in the model without the dependence on coverage, while the cluster-cluster interaction term is a variable part which is a function of c. It exhibits global effects because of the long-range nature of elastic interactions. In the case of interfacial dislocations, we mainly focus on applying our model to a surface of SiGe material system with interfacial

dislocation networks buried at 80 nm depth. From the numerical simulations, our model shows qualitative and quantitative agreement with experimental results. It is found that the spatial and size distribution of adatom clusters is a result of the interplay between self-organization and forced-organization effects provided by external fields, even for a strain field as weak as 0.01%. In the specific case of buried dislocations, for an average coverage greater than 0.15, monolayer clusters tend to agglomerate at the compressive side of dislocations. For an even lower coverage not below the critical coverage, such as 0.01, we could obtain dots distributed uniformly along the dislocation lines. The presence of cluster-cluster interactions in the model provides an extra force between clusters so that clusters have smaller sizes and denser distributions. This force also destabilizes the self-organized system. We also present two possible applications of our model on the two different types of external fields, i.e. inclusion strain fields and electromagnetic fields. The theoretical work related with these specific models are developed in this thesis and future numerical work is planned.

The third part (Chapter VI) is the *atomistic modelling* in which we discussed that the island diffusion plays a dominant role in forming the atomic cluster nucleus at the very early stage of evolution under an extremely weak inhomogeneous stain field. In this part of the research, we developed a Kinetic Monte Carlo methods on the basis of *ab initio* and empirical potentials and we use pathways on reconstructed Si surfaces and equivalent island diffusion kinetics.

Finally, it should be emphasized again that both our phase field model and KMC simulations are based on a monolayer structure of clusters. For the interfacial dislocation case in the SiGe system in comparison with experimental results [34], our model should be understood as for the cluster evolution after the wetting layer is formed. Since we only investigate the early stages of nucleation with

very low coverage, we reasonably ignored the effects of the mass redistribution between the wetting layer and quantum dots. In order to develop the 3-D island formation model, a multi-layer deposition process must be added in the present model. However, the current model has already provided the essence of the problem, which shows the various means of fabricating self-organized quantum dots by controlling parameters such as average coverage, temperature, strain fields and proper electromagnetic wave modes and amplitudes.

In the following, we list again the main achievements of the present research:

- We developed a phase field model with a continuum variable, coverage c, to describe the monolayer cluster formation on the surface. Especially we include the effects of field-adatom interactions and cluster-cluster interactions.

- We developed a numerical method to calculate the governing equations in the phase field model. The method is based on the Fourier-Galerkin spectral approach.

- We made the simulations on the external field generated by interfacial dislocation networks and a qualitative and quantitative agreement is obtained by comparisons with the experimental observations.

- We made a KMC simulation by empirical interatomic potential determination of energetics and island diffusion kinetics. The atomistic result reveals that island diffusion plays a dominant role in the early stage of nucleation.

APPENDIX A

Nearest-Neighbor Interactions by Variational Mean-Field Theory

THE general technique for developing mean-field theories based on a variational principal is reviewed and applied to the Potts model for charged systems by Chaikin [13]. Here the derivation follows the idea presented by Walgraef [79]. To determine $\mathscr{F}^{(a)}$, we begin with writing the Hamiltonian of a discrete lattice system of adparticles on a substrate between which two-body interactions exist.

$$\mathscr{H}^{(a)} = \frac{1}{2}\sum_{ij} \epsilon_{ij}^{(a)} s_i s_j, \tag{A.1}$$

where s_i is the occupation number at site i which takes values of 0 or 1. The two-body interaction energies, $\epsilon_{ij}^{(a)}$, are negative for attractive interactions. Due to the difficulty in having a precise evaluation of the partition function for this Hamiltonian, we first approximate it by the mean-field Hamiltonian

$$\mathscr{H}_0 = k_{\mathrm{B}} T \sum_i \lambda_i s_i, \tag{A.2}$$

where $k_{\mathrm{B}} T \lambda_i$ denotes the mean interaction energy between an adatom at site i. The corresponding mean field partition function is

$$\mathcal{Z}_0 = \prod_i \sum_{s_i=0,1} \exp(-\lambda_i s_i) = \prod_i \frac{1}{1-c_i}, \tag{A.3}$$

where $c_i = 1/(1+\exp\lambda_i) = \langle s_i \rangle_0$, which is the equilibrium average of the mean field occupancy number at site i. This is a continuous variable varying between 0 and 1, which is just the coverage of adsorbed particles. The mean-field free energy is

$$\mathscr{F}_0 = k_{\mathrm{B}} T \sum_i \ln(1-c_i). \tag{A.4}$$

By the variational mean-field theory, the exact free energy can be approximated as

$$\mathscr{F}^{(a)} \approx \mathscr{F}_0 + \langle \mathscr{H}^{(a)} - \mathscr{H}_0 \rangle_0. \tag{A.5}$$

Using Equations (A.1) and (A.2) we have

$$\langle \mathscr{H}^{(a)} - \mathscr{H}_0 \rangle_0 = \frac{1}{2} \sum_{ij} \epsilon_{ij}^{(a)} c_i c_j - k_{\mathrm{B}} T \sum_i \lambda_i c_i. \tag{A.6}$$

Equation (A.5) becomes

$$\mathscr{F}^{(a)} = k_{\mathrm{B}} T \sum_i \big[(1-c_i)\ln(1-c_i) + c_i \ln c_i\big] + \frac{1}{2} \sum_{ij} \epsilon_{ij}^{(a)} c_i c_j. \tag{A.7}$$

It is obvious that we obtained the same expression for the N-N free energy as in Equation 6.7

APPENDIX B

Green's Function for Half-Space

THE nonzero coefficients of $\mathcal{G}_{mn}$ described in Section 8 are listed below [40]:

$$\begin{aligned}\mathcal{G}_{11}(q|zz') &= -\frac{1}{4\,q\,c_t^2c_l^2}\Big\{\exp(-q|z-z'|)\big[(c_l^2+c_t^2)-(c_l^2-c_t^2)\,q|z-z'|\big]\Big\}\\ &\quad-\frac{\exp\big[-q(z+z')\big]}{4\,q\,c_t^2c_l^2}\left\{\frac{c_l^4+c_t^4}{c_l^2-c_t^2}-(c_l^2+c_t^2)\,q(z+z')\right.\\ &\qquad\left.+2(c_l^2-c_t^2)\,q^2zz'\right\} \qquad \text{(B.1)}\end{aligned}$$

$$\begin{aligned}\mathcal{G}_{13}(q|zz') &= -\frac{\mathbf{i}}{4\,q}\frac{c_l^2-c_t^2}{c_t^2c_l^2}\exp(-q|z-z'|)\,q|z-z'|\\ &\quad-\frac{\mathbf{i}}{4\,q}\exp\big[-q(z+z')\big]\left\{\frac{2}{c_l^2-c_t^2}-\frac{(c_l^2+c_t^2)}{c_t^2c_l^2}\,q(z-z')\right.\\ &\qquad\left.-\frac{2(c_l^2-c_t^2)}{c_t^2c_l^2}\,q^2zz'\right\} \qquad \text{(B.2)}\end{aligned}$$

$$\begin{aligned}\mathcal{G}_{31}(q|zz') &= -\frac{\mathbf{i}}{4\,q}\frac{c_l^2-c_t^2}{c_t^2c_l^2}\exp(-q|z-z'|)\,q|z-z'|\\ &\quad+\frac{\mathbf{i}}{4\,q}\exp\big[-q(z+z')\big]\left\{\frac{2}{c_l^2-c_t^2}+\frac{(c_l^2+c_t^2)}{c_t^2c_l^2}\,q(z-z')\right.\\ &\qquad\left.-\frac{2(c_l^2-c_t^2)}{c_t^2c_l^2}\,q^2zz'\right\} \qquad \text{(B.3)}\end{aligned}$$

$$\begin{aligned}\mathcal{G}_{33}(q|zz') &= -\frac{1}{4\,q\,c_t^2c_l^2}\Big\{\exp(-q|z-z'|)\big[(c_l^2+c_t^2)+(c_l^2-c_t^2)\,q|z-z'|\big]\Big\}\\ &\quad -\frac{\exp\big[-q(z+z')\big]}{4\,q\,c_t^2c_l^2}\Bigg\{\frac{c_l^4+c_t^4}{c_l^2-c_t^2}+(c_l^2+c_t^2)\,q(z+z')\\ &\qquad +2(c_l^2-c_t^2)\,q^2zz'\Bigg\} \qquad \text{(B.4)}\end{aligned}$$

$$\mathcal{G}_{22}(q|zz') = -\frac{1}{2\,q\,c_t^2}\exp\big(-q|z-z'|\big)-\frac{1}{2\,q\,c_t^2}\exp\big(-q|z+z'|\big). \qquad \text{(B.5)}$$

For references, the Green's function in physical space for the semi-infinite isotropic medium given by Mindlin [54] are listed below

$$\begin{aligned}G_{\alpha\beta}(\mathbf{x},\mathbf{x}') &= G_{\beta\alpha}(\mathbf{x},\mathbf{x}')\\ &= \frac{1}{16\pi\mu(1-\nu)}\Bigg[\frac{3-4\nu}{R_1}\delta_{\alpha\beta}+\frac{1}{R_2}\delta_{\alpha\beta}+\frac{(x_\alpha-x'_\alpha)(x_\beta-x'_\beta)}{R_1^3}\\ &\quad +\frac{(3-4\nu)(x_\alpha-x'_\alpha)(x_\beta-x'_\beta)}{R_2^3}\\ &\quad +\frac{2x_3x'_3}{R_2^3}\Bigg\{\delta_{\alpha\beta}-\frac{3(x_\alpha-x'_\alpha)(x_\beta-x'_\beta)}{R_2^2}\Bigg\}\\ &\quad +\frac{4(1-\nu)(1-2\nu)}{R_2+x_3+x'_3}\Bigg\{\delta_{\alpha\beta}-\frac{(x_\alpha-x'_\alpha)(x_\beta-x'_\beta)}{R_2(R_2(R_2+x_3+x'_3))}\Bigg\}\Bigg] \qquad \text{(B.6)}\end{aligned}$$

$$\begin{aligned}G_{3\beta}(\mathbf{x},\mathbf{x}') &= \frac{(x_\beta-x'_\beta)}{16\pi\mu(1-\nu)}\Bigg[\frac{(x_3-x'_3)}{R_1^3}+\frac{(3-4\nu)(x_3-x'_3)}{R_2^3}\\ &\quad -\frac{6x_3x'_3(x_3+x'_3)}{R_2^5}+\frac{4(1-\nu)(1-2\nu)}{R_2(R_2+x_3+x'_3)}\Bigg] \qquad \text{(B.7)}\end{aligned}$$

$$\begin{aligned}G_{\alpha3}(\mathbf{x},\mathbf{x}') &= \frac{(x_\alpha-x'_\alpha)}{16\pi\mu(1-\nu)}\Bigg[\frac{(x_3-x'_3)}{R_1^3}+\frac{(3-4\nu)(x_3-x'_3)}{R_2^3}\\ &\quad +\frac{6x_3x'_3(x_3+x'_3)}{R_2^5}-\frac{4(1-\nu)(1-2\nu)}{R_2(R_2+x_3+x'_3)}\Bigg] \qquad \text{(B.8)}\end{aligned}$$

$$G_{33}(\mathbf{x},\mathbf{x}') = \frac{1}{16\pi\mu(1-\nu)}\left[\frac{3-4\nu}{R_1}+\frac{8(1-\nu)^2-(3-4\nu)}{R_2}+\frac{(x_3-x_3')^2}{R_1^3}\right.$$
$$\left.+\frac{(3-4\nu)(x_3+x_3')^2-2x_3x_3'}{R_2^3}+\frac{6x_3x_3'(x_3+x_3')^2}{R_2^5}\right], \qquad \text{(B.9)}$$

where $\alpha,\beta = 1,2$, μ is the shear modulus and ν is Poisson's ratio.

$$\begin{aligned} R_1^2 &= (x_1-x_1')^2+(x_2-x_2')^2+(x_3-x_3')^2 \\ R_2^2 &= (x_1-x_1')^2+(x_2-x_2')^2+(x_3+x_3')^2. \end{aligned} \qquad \text{(B.10)}$$

APPENDIX C

Elastic Dislocation Fields of Multi-Layer Structures

THE formal approach to solve the elastic field of interfacial dislocations (or fractures) of multi-layer structures is to formulate the displacement by the Fourier transform method. Specifically for the 2-D problem (x is along the surface and y is along the depth of the structure), the transform can be taken along the x direction:

$$U^{(i)}(x,y) = \frac{1}{\sqrt{2\pi}} \int_{-\infty}^{+\infty} \Psi^{(i)}(\alpha, y)\, e^{-i\alpha x} d\alpha, \tag{C.1}$$

where i denotes i^{th} layer $(i = 1, ...n)$ and the dislocation lies at the interface between layers (i) and $(i+1)$.

$U^{(i)}$ is the displacement vector of the i^{th} layer and:

$$U^{(i)} = \left(u^{(i)}(x,y), v^{(i)}(x,y)\right)^T. \tag{C.2}$$

$\Psi^{(\mathrm{i})}$ is the complex transformed displacement vector of the i^{th} layer in Fourier space and:

$$\Psi^{(i)} = \left(\phi^{(i)}(\alpha, y), \psi^{(i)}(\alpha, y)\right)^T. \tag{C.3}$$

The displacement and transformed displacement can be decomposed to symmetric and anti-symmetric parts as shown in Figure C.1.

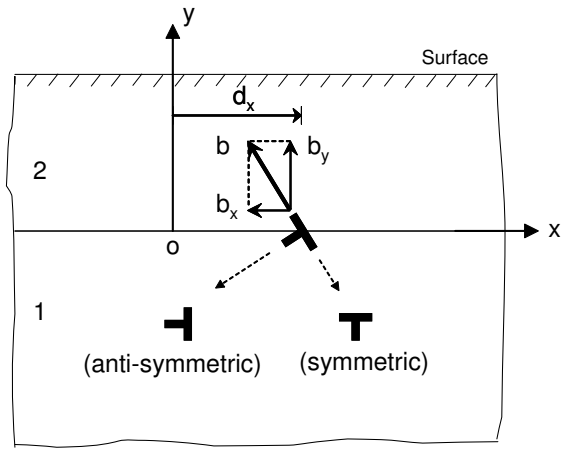

Figure C.1: Bonded layer structure with a single interfacial dislocation

$$U^{(i)} = U_s^{(i)} + U_a^{(i)}, \qquad \Psi^{(i)} = \Psi_s^{(i)} + \Psi_a^{(i)}. \tag{C.4}$$

Consider the solution for the symmetric case,

$$\begin{aligned} u_s^{(i)}(x,y) &= \frac{2}{\pi}\int_0^\infty \phi_s^{(i)}(\alpha,y)\sin\alpha x d\alpha \\ v_s^{(i)}(x,y) &= \frac{2}{\pi}\int_0^\infty \psi_s^{(i)}(\alpha,y)\cos\alpha x d\alpha. \end{aligned} \tag{C.5}$$

Using the Navier's equations for an isotropic, homogeneous medium, i.e.

$$\left(\lambda^{(i)} + \mu^{(i)}\right)\nabla\left(\nabla\cdot U_s^{(i)}\right) + \mu^{(i)}\nabla^2 U_s^{(i)} = 0. \tag{C.6}$$

The displacement vector can be obtained with unknown A_{sj}, which are the functions of α:

$$
\begin{aligned}
u_s^{(i)}(x,y) &= \frac{2}{\pi}\int_0^{+\infty}\left[\left(A_{s1}^{(i)}+A_{s2}^{(i)}y\right)e^{-\alpha y}+\left(A_{s3}^{(i)}+A_{s4}^{(i)}y\right)e^{\alpha y}\right]\sin\alpha x d\alpha \\
v_s^{(i)}(x,y) &= \frac{2}{\pi}\int_{-\infty}^{+\infty}\left\{\left[A_{s1}^{(i)}+\left(\frac{\kappa^{(i)}}{\alpha}+y\right)A_{s2}^{(i)}\right]e^{-\alpha y}\right. \\
&\qquad \left.+\left[-A_{s3}^{(i)}+\left(\frac{\kappa^{(i)}}{\alpha}-y\right)A_{s4}^{(i)}\right]e^{\alpha y}\right\}\cos\alpha x d\alpha,
\end{aligned}
\tag{C.7}
$$

where $\kappa^{(i)}=3-4\nu^{(i)}$ for plane strain and $\left(3-\nu^{(i)}\right)/\left(1+\nu^{(i)}\right)$ for plane stress. and $A_{sj}^{(i)}$ are functions of α, which will be determined from the boundary and the continuity conditions.

In a two-layered system, the functions $A_{sj}^{(i)}$ and $A_{aj}^{(i)}$ can be obtained as follows:

In the *symmetric* case:

$$
\begin{aligned}
\alpha A_{s1}^{(1)}+\alpha A_{s3}^{(1)}-\alpha A_{s3}^{(2)} &= b_x\cos\alpha t \\
-\alpha A_{s1}^{(1)}-\kappa^{(1)}+\alpha A_{s3}^{(1)}-\kappa^{(1)}A_{s4}^{(1)}-\alpha A_{s3}^{(2)}+\kappa^{(2)}A_{s4}^{(2)} &= 0 \\
-\alpha\mu^{(1)}A_{s1}^{(1)}-2\mu^{(1)}\left(1-\nu^{(1)}\right)A_{s2}^{(1)}-\alpha\mu^{(1)}A_{s3}^{(1)} & \\
+2\mu^{(1)}\left(1-\nu^{(1)}\right)A_{s4}^{(1)}+\alpha\mu^{(2)}A_{s3}^{(2)}-2\mu^{(2)}\left(1-\nu^{(2)}\right)A_{s4}^{(2)} &= 0 \\
-\alpha\mu^{(1)}A_{s1}^{(1)}-\mu^{(1)}\left(1-2\nu^{(1)}\right)A_{s2}^{(1)}+\alpha\mu^{(1)}A_{s3}^{(1)} & \\
-\mu^{(1)}\left(1-2\nu^{(1)}\right)A_{s4}^{(1)}-\alpha\mu^{(2)}A_{s3}^{(2)}+\mu^{(2)}\left(1-2\nu^{(2)}\right)A_{s4}^{(2)} &= 0 \\
-\alpha e^{2\alpha h}A_{s1}^{(1)}-\left[\alpha h+2\left(1-\nu^{(1)}\right)\right]e^{-2\alpha h}A_{s2}^{(1)} & \\
-\alpha A_{s3}^{(1)}-\left[\alpha h-2\left(1-\nu^{(1)}\right)\right]A_{s4}^{(1)} &= 0 \\
-\alpha e^{2\alpha h}A_{s1}^{(1)}-\left[\alpha h+\left(1-2\nu^{(1)}\right)\right]e^{-2\alpha h}A_{s2}^{(1)} & \\
+\alpha A_{s3}^{(1)}+\left[\alpha h-\left(1-2\nu^{(1)}\right)\right]A_{s4}^{(1)} &= 0.
\end{aligned}
\tag{C.8}
$$

Using 2-D stress-strain relations, the stresses can be evaluated as follows:

$$
\begin{aligned}
\sigma_{sxx}^{(i)} &= \frac{4\mu^{(i)}}{\pi}\int_0^\infty \left\{\left[\alpha\left(A_{s1}^{(i)}+A_{s2}^{(i)}y\right)-2\nu^{(i)}A_{s2}^{(i)}\right]e^{-\alpha y}\right. \\
&\quad \left.+\left[\alpha\left(A_{s3}^{(i)}+A_{s4}^{(i)}y\right)+2\nu^{(i)}A_{s4}^{(i)}\right]e^{\alpha y}\right\}\cos\alpha x d\alpha \\
\sigma_{syy}^{(i)} &= \frac{4\mu^{(i)}}{\pi}\int_0^\infty \left\{-\left[\alpha\left(A_{s1}^{(i)}+A_{s2}^{(i)}y\right)+2\left(1-\nu^{(i)}\right)A_{s2}^{(i)}\right]e^{-\alpha y}\right. \\
&\quad \left.+\left[-\alpha\left(A_{s3}^{(i)}+A_{s4}^{(i)}y\right)+2\left(1-\nu^{(i)}\right)A_{s4}^{(i)}\right]e^{\alpha y}\right\}\cos\alpha x d\alpha \\
\sigma_{sxy}^{(i)} &= \frac{4\mu^{(i)}}{\pi}\int_0^\infty \left\{-\left[\alpha\left(A_{s1}^{(i)}+A_{s2}^{(i)}y\right)+\left(1-2\nu^{(i)}\right)A_{s2}^{(i)}\right]e^{-\alpha y}\right. \\
&\quad \left.+\left[\alpha\left(A_{s3}^{(i)}+A_{s4}^{(i)}y\right)-\left(1-2\nu^{(i)}\right)A_{s4}^{(i)}\right]e^{\alpha y}\right\}\sin\alpha x d\alpha.
\end{aligned}
\tag{C.9}
$$

A similar procedure is followed for the anti-symmetric case with slight modifications (Equations from C.10 to C.13).

For the *anti-symmetric* case:

$$
\begin{aligned}
u_a^{(i)}(x,y) &= \frac{2}{\pi}\int_0^\infty \phi_a^{(i)}(\alpha,y)\cos\alpha x d\alpha \\
v_a^{(i)}(x,y) &= \frac{2}{\pi}\int_0^\infty \psi_a^{(i)}(\alpha,y)\sin\alpha x d\alpha.
\end{aligned}
\tag{C.10}
$$

By the same procedure as in the symmetric case, we have the following equations for solving $A_{aj}^{(i)}$:

$$
\begin{aligned}
\alpha A_{a1}^{(1)} + \alpha A_{a3}^{(1)} - \alpha A_{a3}^{(2)} &= 0 \\
-\alpha A_{a1}^{(1)} - \kappa^{(1)} + \alpha A_{a3}^{(1)} - \kappa^{(1)} A_{a4}^{(1)} - \alpha A_{a3}^{(2)} + \kappa^{(2)} A_{a4}^{(2)} &= b_y \sin \alpha t \\
-\alpha\mu^{(1)} A_{a1}^{(1)} - 2\mu^{(1)} \left(1-\nu^{(1)}\right) A_{a2}^{(1)} - \alpha\mu^{(1)} A_{a3}^{(1)} & \\
+2\mu^{(1)} \left(1-\nu^{(1)}\right) A_{a4}^{(1)} + \alpha\mu^{(2)} A_{a3}^{(2)} - 2\mu^{(2)} \left(1-\nu^{(2)}\right) A_{a4}^{(2)} &= 0 \\
-\alpha\mu^{(1)} A_{a1}^{(1)} - \mu^{(1)} \left(1-2\nu^{(1)}\right) A_{a2}^{(1)} + \alpha\mu^{(1)} A_{a3}^{(1)} & \\
-\mu^{(1)} \left(1-2\nu^{(1)}\right) A_{a4}^{(1)} - \alpha\mu^{(2)} A_{a3}^{(2)} + \mu^{(2)} \left(1-2\nu^{(2)}\right) A_{a4}^{(2)} &= 0 \qquad \text{(C.11)} \\
-\alpha e^{2\alpha h} A_{a1}^{(1)} - \left[\alpha h + 2\left(1-\nu^{(1)}\right)\right] e^{-2\alpha h} A_{a2}^{(1)} & \\
-\alpha A_{a3}^{(1)} - \left[\alpha h - 2\left(1-\nu^{(1)}\right)\right] A_{a4}^{(1)} &= 0 \\
-\alpha e^{2\alpha h} A_{a1}^{(1)} - \left[\alpha h + \left(1-2\nu^{(1)}\right)\right] e^{-2\alpha h} A_{a2}^{(1)} & \\
+\alpha A_{a3}^{(1)} + \left[\alpha h - \left(1-2\nu^{(1)}\right)\right] A_{a4}^{(1)} &= 0.
\end{aligned}
$$

The displacement and stress solutions are then given by:

$$
\begin{aligned}
u_a^{(i)}(x,y) &= \frac{2}{\pi} \int_0^{+\infty} \left[\left(A_{a1}^{(i)} + A_{a2}^{(i)} y \right) e^{-\alpha y} + \left(A_{a3}^{(i)} + A_{a4}^{(i)} y \right) e^{\alpha y} \right] \cos \alpha x d\alpha \\
v_a^{(i)}(x,y) &= \frac{1}{\pi} \int_{-\infty}^{+\infty} \left\{ \left[A_1^{(i)} + \left(\frac{\kappa^{(i)}}{\alpha} + y \right) A_2^{(i)} \right] e^{-\alpha y} \right. \qquad \text{(C.12)} \\
&\qquad \left. + \left[-A_3^{(i)} + \left(\frac{\kappa^{(i)}}{\alpha} - y \right) A_4^{(i)} \right] e^{\alpha y} \right\} \cos \alpha x d\alpha,
\end{aligned}
$$

$$
\begin{aligned}
\sigma_{axx}^{(i)} &= \frac{4\mu^{(i)}}{\pi}\int_0^\infty \Big\{\Big[-\alpha\left(A_{a1}^{(i)}+A_{a2}^{(i)}y\right)+2\nu^{(i)}A_{a2}^{(i)}\Big]e^{-\alpha y} \\
&\qquad -\Big[\alpha\left(A_{a3}^{(i)}+A_{a4}^{(i)}y\right)+2\nu^{(i)}A_{a4}^{(i)}\Big]e^{\alpha y}\Big\}\sin\alpha x d\alpha \\
\sigma_{ayy}^{(i)} &= \frac{4\mu^{(i)}}{\pi}\int_0^\infty \Big\{\Big[\alpha\left(A_{a1}^{(i)}+A_{a2}^{(i)}y\right)+2\left(1-\nu^{(i)}\right)A_{a2}^{(i)}\Big]e^{-\alpha y} \\
&\qquad +\Big[\alpha\left(A_{a3}^{(i)}+A_{a4}^{(i)}y\right)-2\left(1-\nu^{(i)}\right)A_{a4}^{(i)}\Big]e^{\alpha y}\Big\}\sin\alpha x d\alpha \\
\sigma_{axy}^{(i)} &= \frac{4\mu^{(i)}}{\pi}\int_0^\infty \Big\{-\Big[\alpha\left(A_{a1}^{(i)}+A_{a2}^{(i)}y\right)+\left(1-2\nu^{(i)}\right)A_{a2}^{(i)}\Big]e^{-\alpha y} \\
&\qquad +\Big[\alpha\left(A_{a3}^{(i)}+A_{a4}^{(i)}y\right)-\left(1-2\nu^{(i)}\right)A_{a4}^{(i)}\Big]e^{\alpha y}\Big\}\cos\alpha x d\alpha.
\end{aligned}
\tag{C.13}
$$

The medium is assumed to be traction-free at the top surface such that:

$$
\begin{aligned}
\sigma_{syy}^{(n)} &= \sigma_{ayy}^{(n)} = 0 \\
\sigma_{sxy}^{(n)} &= \sigma_{axy}^{(n)} = 0.
\end{aligned}
\tag{C.14}
$$

While at the interfaces, continuity is required in adjacent layers, such that:

$$
\begin{aligned}
u_s^{(i+1)} - u_s^{(i)} = u_a^{(i+1)} - u_a^{(i)} &= 0 \\
v_s^{(i+1)} - v_s^{(i)} = v_a^{(i+1)} - v_a^{(i)} &= 0 \\
\sigma_{syy}^{(i+1)} - \sigma_{syy}^{(i)} = \sigma_{ayy}^{(i+1)} - \sigma_{ayy}^{(i)} &= 0 \\
\sigma_{sxy}^{(i+1)} - \sigma_{sxy}^{(i)} = \sigma_{asxy}^{(i+1)} - \sigma_{axy}^{(i)} &= 0.
\end{aligned}
\tag{C.15}
$$

For an interface with a dislocation at $x = d_x$, we have:

$$\begin{aligned}
\frac{\partial}{\partial x}\left(u_s^{(1)} - u_s^{(2)}\right) &= b_x^e \delta\left(x - d_x\right) \\
\frac{\partial}{\partial x}\left(u_a^{(1)} - u_a^{(2)}\right) &= 0 \\
\frac{\partial}{\partial x}\left(v_s^{(1)} - v_s^{(2)}\right) &= 0 \\
\frac{\partial}{\partial x}\left(v_a^{(1)} - v_a^{(2)}\right), &= b_y^e \delta\left(x - d_x\right)
\end{aligned} \tag{C.16}$$

where $\delta(x - d_x)$ is the Dirac Delta function.

By numerical methods, the solutions for displacement and stress expressions can be obtained by substituting Equations (C.9, C.7) into Equations (C.14, C.15, C.16). The final displacement and stress fields are the sum of the symmetric and anti-symmetric parts.

The material constants used in the present calculation are selected as shown in Table C.1:

Material	Shear Modulus	Poisson Ratio	Lattice Constant	Burger's Vector
Si	79.9 GPa	0.266	5.43095 $\mathring{A}$	3.84026 $\mathring{A}$
Ge	67.0 GPa	0.280	5.64613 $\mathring{A}$	3.99241 $\mathring{A}$
$Si_{0.85}Ge_{0.15}$	77.965 GPa	0.268	5.46322 $\mathring{A}$	3.86308 $\mathring{A}$

Table C.1: Elastic and lattice constants for Si, Ge, and $Si_{0.85}Ge_{0.15}$

References

[1] O. L. Alerhand, D. Vanderbilt, R. D. Meade, and J. D. Joannopoulos. Spontaeous formation of stress domains on crystal surfaces. *Physical Review Letters*, 61:1973–6, 1988.

[2] R. Asaro and W. Tiller. Interface morphology development during stress-corrosion cracking .1. via surface diffusion. *Metallurgical Transactions*, 3(7):1789, 1972.

[3] A. Ashkin. Trappings of atoms by resonance radiation pressure. *Physical Review Letters*, 40:729–32, 1978.

[4] A. L. Barabási. Self-assembled island formation in heteroepitaxial growth. *Applied Physics Letters*, 70(19):2565–2567, May 1997.

[5] J. W. Barrett, J. F. Blowey, and H. Garcke. Finite element approximation of the Cahn-Hilliard equation with degenerate mobility. *SIAM J. Numer. Anal.*, 37(1):286–318, 1999.

[6] M.I. Baskes. Atomistic potentials for the molybdenum-silicon system. *Materials Science & Engineering A (Structural Materials: Properties, Microstructure and Processing)*, 261(1-2):165–8, March 1999.

[7] M. I. Baskes. Modified embedded-atom potentials for cubic materials and impurities. *Physical Review B*, 46(5):462727–42, August 1992.

[8] D. Bimberg, M. Grundmann, and N. N. Ledentsov. *Quantum Dot Heterostructures*. John Wiley & Sons, 1999.

[9] A. Bogicevic, S. Liu, J. Jacobsen, B. Lundqvist, and H. Metiu. Island migration caused by the motion of the atoms at the border: size and temperature dependence of the diffusion coefficient. *Physical Review B*, 57(16):R9459–62, 1998.

[10] E. Brigham. *The Fast Fourier Transform and its Applications*. Prentice-Hall, 1988.

[11] J. W. Cahn. On spinodal decomposition. *Acta Metall.*, 9(9):795–801, February 1961.

[12] C. Canuto and et al. *Spectral Methods in Fluid Dynamics*. Springer-Verlag, 1988.

[13] P. M. Chaikin and T. C. Lubensky. *Principles of Condensed Matter Physics*. Cambridge University Press, 2000.

[14] L.Q. Chen and J. Shen. Applications of semi-implicit Fourier-spectral method to phase field equations. *Computer Physics Communications*, 108:147–58, 1998.

[15] I. Eisele and W. Hansch. Nanostructures in silicon devices. *Thin Solid Films*, 369:60–4, 2000.

[16] H. Ellmer, V. Repain, S. Rousset, B. Croset, M. Sotto, and P. Zeppenfeld. Self-ordering in two dimensions: nitrogen adsorption on copper (100) followed by STM at elevated temperature. *Surface Science*, 476:95–106, 2001.

[17] F. Erdogan and G. Gupta. The stress analysis of multi-layered composites with a flaw. *International Journal of Solids and Structures*, 7:39–61, 1971.

[18] N. M. Ghoniem, D. Walgraef, and S. J. Zinkle. Theory and experiment of nanostructure self-organization in irradiated materials. *Journal of Computer-Aided Materials Design*, 8:1–38, 2002.

[19] N. M. Ghoniem and D. Walgraef. *Instabilities in Nonequilibrium Materials*. Oxford, 2005.

[20] G. H. Gilmer and P. Bennema. Simulation of crystal growth with surface diffusion. *Journal of Applied Physics*, 43(4):1347–60, 1971.

[21] D. Gottlieb and S. A. Orszag. *Numerical Analysis of Spectral Methods: Theory and Applications*. SIAM, 1977.

[22] De Groot and P. Mazur. *Non-Equilibrium Thermodynamics*. Dover, 1984.

[23] T. Hasebe. Physical and mathematical background of field theoretical multiscale polycrystalline plasticity model. In *8th National Congress on Computational Mechanics*, 2005.

[24] K. Hellwege and O. Madelung, editors. *Numerical Data and Functional Relationships in Science and Technology*, volume III. Springer, Berlin, 1982.

[25] M. Hildebrand, A. Mikhailov, and G. Ertl. Nonequilibrium stationary microstruc-tures in surface chemical reactions. *Physical Review E*, 58:5483–5493, 1998.

[26] T. Hoshino, M. Hata, and M. Tsuda. Migration of Si adatom on strained Si(111) surfaces. *Surface Science*, 481:205–214, 2001.

[27] H. Huang, N. M. Ghoniem, J.K. Wang, and M.I. Baskes. Molecular dynamics determination of defect energetics in $\beta - SiC$ using three representative empirical potentials. *Modelling Simul. Mater. Sci. Eng.*, 3:615–27, 1995.

[28] H. Huang, G. H. Gilmer, and T. Diaz de la Rubia. An atomistic simulator for thin film deposition in three dimensions. *Journal of Applied Physics*, 84:3636–49, 1998.

[29] K. Kassner, C. Misbah, J. Muller, J. Kappey, and P. Kohlert. Phase-field modeling of stress-induced instabilities. *Physical Review E*, 63(3):036117, February 2001.

[30] A. G. Khachaturyan. *Theory of Structural Transformations in Solids*. John Wiley & Sons, 1983.

[31] O. Kienzle, F. Ernst, M. Ruhle, O.G. Schmidt, and K. Eberl. Germanium quantum dots embedded in silicon: Quantitative study of self-alignment and coarsening. *Applied Physics Letters*, 74(2):269–71, January 1999.

[32] H. J. Kim, J. Y. Chang, and Y. H. Xie. Influence of a buried misfit dislocation network on the pyramid-to-dome transition size of Ge self-assembled quantum dots on Si(001). *Journal of Crystal Growth*, 247(3-4):251–4, 2003.

[33] H. J. Kim, Z. M. Zhao, J. Liu, V. Ozolins, J. Y. Chang, and Y. H. Xie. A technique for the measurement of surface diffusion coefficient and activation energy of Ge adatom on Si(001). *Journal of Applied Physics*, 95(11):6065–71, June 2004.

[34] H. J. Kim, Z. M. Zhao, and Y. H. Xie. Three-stage nucleation and growth of Ge self-assembled quantum dots grown on partially relaxed SiGe buffer layers. *Physical Review B*, 68:2053121–7, 2003.

[35] L. D. Landau and E. M. Lifshitz. *Fluid Mechanics*. Pergamon, New York, 1987.

[36] K. H. Lau and W. Kohn. Elastic interaction of two atoms adsorbed on a solid surface. *Surface Science*, 65:607–18, 1977.

[37] Z. L. Liau. Strained interface of lattice-mismatched wafer fusion. *Physical Review B*, 55:12899–901, 1997.

[38] W. K. Liu, E. G. Karpov, S. Zhang, and H. S. Park. An introduction to computational nanomechanics and materials. *Computer Methods in Applied Mechanics and Engineering*, 193:1529–78, 2004.

[39] K. Mae. Single adatom diffusion in homo- and heteroepitaxies of Si and Ge on $(100) - 2 \times 1$ surface modeled by MEAM. *Thin Solid Films*, 395:235–239, 2001.

[40] A. A. Maradudin and R. F. Wallis. Elastic interactions of point defects in a semi-infinite medium. *Surface Science*, 91:423–39, 1980.

[41] V. I. Marchenko and A. Ya. Parshin. Elastic properties of crystal surfaces. *Sov. Phys. JETP*, 52:129, 1980.

[42] T.R. Mattsson and H. Metia. Nucleation and coarsening during epitaxy on a substrate subject to periodic strain: Spatial ordering and size uniformity. *Journal of Chemical Physics*, 113(22):10323–32, December 2000.

[43] T.R. Mattsson, G. Millis, and H. Metiu. A new method for simulating the late stages of island coarsening in thin film growth: The role of island diffusion and evaporation. *Journal of Chemical Physics*, 110(24):12151–60, June 1999.

[44] T. R. Mattsson and H. Metiu. Kinetic Monte Carlo simulations of nucleation on a surface with periodic strain: Spatial ordering and island-size distribution. *Applied Physics Letters*, 75(7):926–928, August 1999.

[45] J. J. McClelland and R. J. Celotta. Laser-focused atomic deposition – nanofabrication via atom optics. *Thin Solid Film*, 367:25–7, 2000.

[46] J. J. McClelland, R. E. Scholten, E. C. Palm, and R. J. Celotta. Laser-focused atomic deposition. *Science*, 262(5):877–83, November 1993.

[47] G. Medeiros-Ribeiro, A.M. Bratkovski, T.I. Kamins, D.A.A. Ohlberg, and R.S. Wiliams. Shape transition of germanium nanocrystals on a silicon (001) surface from pyramids to domes. *Science*, 279(5349):353–5, 1998.

[48] H. Metiu and G. Rosenfeld. The evaporation rate of a one-atom-high island on a solid surface: a thermodynamic theory of the size dependence. *Surface Science*, 373:L357–362, 1997.

[49] G. Mills, T.R. Mattsson, L. Mollnitz, and H. Metiu. Simulations of mobility and evaporation rate of adsorbate islands on solid surfaces. *Journal of Chemical Physics*, 111(18):8639–50, November 1999.

[50] V. Milman. Ab initio study of epitaxial growth on stepped Si(100) surface. *International Journal of Quantum Chemistry*, 61:719–724, 1997.

[51] M. H. Mittleman. *Introduction to the Theory of Laser-Atom Interactions*. Plenum Press, New York, 1993.

[52] Nunzio Motta, Anna Sgarlata, Federico Rosei, P. D. Szkutnik, S. Nufris, M. Scarselli, and A. Balzarotti. Controlling the quantum dot nucleation site. *Materials Science and Engineering*, B101:77–88, 2003.

[53] Y.-W. Mo, D. E. Savage, B. S. Swartzentruber, and M. G. Lagally. Kinetic pathway in Stranski-Krastanov growth of Ge on Si(001). *Physical Review Letters*, 65:1020, 1990.

[54] T. Mura. *Micromechanics of Defects in Solids*. Martinus Nijhoff, Boston, USA, 1987.

[55] B. Niethammer. Derivation of the LSW-Theory for Ostwald ripening by homogenization methods. *Arch. Rational Mech. Anal.*, 147:119–78, 1999.

[56] E. Pan. Three-dimensional Green's functions in an anisotropic half-space with general boundary conditions. *Journal of Applied Mechanics*, 70:101–10, January 2003.

[57] S. J. H. Petra, K. A. H. Van Leeuwen, L. Feenstra, W. Hogervorst, and W. Vassen. Atom lithography with two-dimensional optical masks. *Applied Physics B*, 79:279–83, 2004.

[58] K. Portz and A. A. Maradudin. Surface contribution to the low-temperature specific heat of a cubic crystal. *Physical Review B*, 16:3535, 1977.

[59] L. Proville. Self-organization of (001) cubic crystal surfaces. *Physical Review B*, 64:165406, 2001.

[60] S. J. Rehse, R. W.McGowan, and S. A. Lee. Optical manipulation of group III atoms. *Applied Physics B – Lasers and Optics*, 70:657–60, 2000.

[61] S. Rousset, V. Repain, G. Baudot, H. Ellmer, Y. Garreau, V. Etgens, J.M. Berroir, B. Croset, M. Sotto, P. Zeppenfeld, J. Ferre, J.P. Jamet, C. Chappert, and J. Lecoeur. Self-ordering on crystal surfaces: fundamentals and applications. *Materials Science and Engineering*, B96:169–77, 2002.

[62] M. Schroeder and D. E. Wolf. Diffusion on strained surfaces. *Surface Science*, 375:129–140, 1997.

[63] H. Shao, P.C. Weakliem, and H. Metiu. Evaporation of single atoms from an adsorbates island or a step to a terrace: Evaporation rate and the underlying atomic-level mechanism. *Physical Review B*, 53(23):16041–9, June 1996.

[64] V. A. Shchukin and D. Bimberg. Spontaneous ordering of nanostructures on crystal surfaces. *Reviews of Modern Physics*, 71(4):1125–71, July 1999.

[65] V. A. Shchukin, A. I. Borovkov, N. N. Ledentsov, and D. Bimberg. Tuning and breakdown of faceting under externally applied stress. *Physical Review B*, 51(15):10104–18, April 1999.

[66] V. A. Shchukin, N. N. Ledentsov, P. S. Kop'ev, and D. Bimberg. Spontaneous ordering of arrays of coherent strained islands. *Physical Review Letters*, 75(16):2968–71, October 1995.

[67] V. B. Shenoy, R. Miller, E. B. Tadmor, R. Phillips, and M. Ortiz. Quasicontinuum models of interfacial structure and deformation. *Physical Review Letters*, 80(4):742–5, 1998.

[68] D.S. Sholl and R.T. Skodje. Diffusion of clusters of atoms and vacancies on surfaces and the dynamics of diffusion-driven coarsening. *Physical Review Letters*, 75(17):3158–61, October 1995.

[69] D. J. Shu, F. Liu, and X. G. Gong. Simple generic method for predicting the effect of strain on surface diffusion. *Physical Review B*, 64:245410, 2001.

[70] B. J. Spencer, S. H. Davis, and P. W. Voorhees. Morphological instability in epitaxially strained dislocation-free solid films: Nonlinear evolution. *Physical Review B*, 47(15):9760–77, April 1993.

[71] B. J. Spencer and J. Tersoff. Equilibrium shapes and properties of epitaxially strained islands. *Physical Review Letters*, 79(24):4858–61, December 1997.

[72] B. J. Spencer, P. W. Voorhees, and S. H. Davis. Morphological instability in epitaxially strained dislocation-free solid films. *Physical Review Letters*, 67(26):3696–9, December 1991.

[73] G. Springholz. Three-dimensional stacking of self-assembled quantum dots in multilayer structures. *C. R. Physique*, 6:89–103, 2005.

[74] Z. Suo. Singularities interacting with interfaces and cracks. *Internal Journal of Solids and Structures*, 25(10):1133–1142, 1989.

[75] P.N. Swarztrauber. Multiprocessor FFTs. *Parallel Computing*, 5:197–210, 1987.

[76] T. C. T. Ting. *Anisotropic Elasticity*. Oxford University Press, Oxford, UK, 1996.

[77] R. M. Tromp, R. J. Hamers, and J. E. Demuth. Si(001) dimer structure observed with scanning tunneling microscopy. *Physical Review Letters*, 55:1303–6, September 1985.

[78] P. W. Voorhees. Ostwald ripening of two-phase mixtures. *Annu. Rev. Mater. Sci.*, 22:197–215, 1992.

[79] D. Walgraef. Reaction-diffusion approach to nanostructure formation during thin film deposition. *Philosophical Magazine*, 83:3829, 2003.

[80] Y. Wang, L.-Q. Chen, and A. G. Khachaturyan. Kinetics of strain-induced morphological transformation in cubic alloys with miscibility gap. *Act Metall. Mater.*, 41(1):279–96, 1993.

[81] J. R. Willis, S. C. Jain, and R. Bullough. The energy of an array of dislocations: implications for strain relaxation in semiconductor heterostructures. *Philosophical Magazine A*, 62(1):115–129, 1990.

[82] E. L. Wolf. *Nanophysics and Nanotechnology.* Wiley-VCH, 2004.